Determining Strength of Materials Under Dynamic Loading Conditions Using Hydrodynamic Instabilities

Thesis by
Zachary Martin Murphy Sternberger

In Partial Fulfillment of the Requirements for the
degree of
Doctor of Philosophy

CALIFORNIA INSTITUTE OF TECHNOLOGY
Pasadena, California

2017
Defended September 12, 2016

Zachary Martin Murphy Sternberger
ORCID: 0000-0002-7612-673X

ACKNOWLEDGEMENTS

I was fortunate to work with a large and helpful group of collaborators. Bruce Remington, Chris Wehrenberg, Brian Maddox, Kathy Opachich, and Richard Kraus gave me advice and support before, during, and after my experiments. Greg Randall, Mike Farrell, Neil Alexander, and Paul Fitzsimmons worked to manufacture our targets and helped profile our samples. My experiments would not have been possible without the help of Shiteng Zhao, Tané Remington, Eric Hahn, Professor Marc Meyers, Suzanne Ali, and Laura Chen. Shiteng and Tané graciously supported my experiments while simultaneously managing their own. I am grateful for the staff at the Jupiter Laser Facility, who poured their time and effort into making our experiments successful.

At Caltech, I had continuous help from Ali Kiani, Joe Haggerty, Petros Arakelian, Cheryl Gause, Dimity Nelson, and Christine Ramirez. Professor Michael Ortiz shared computational resources and Trent Kirchdoerfer helped me sort out problems with my simulations. My first year classmates made surviving my transition to Caltech possible by answering my questions and making me laugh. I especially appreciate my teammates on Professional Tractor / Aftermath for the work they put into making our seasons fun and rewarding.

I am thankful for the advice of my candidacy and thesis committee members, Professor Ares Rosakis, Professor Kaushik Bhattacharya, Professor Dennis Kochmann, and Professor Dan Meiron.

And I am thankful for my advisor, Ravi, for his clear and calm approach to my problems.

This work was supported by the NNSA through the HEDLP program, grant numbers DE-NA0001805 and DE-NA0001832. This work was possible due to experimental time awarded by the Jupiter Laser Facility, Lawrence Livermore National Laboratory.

ABSTRACT

Hydrodynamic instability experiments allow access to material properties at extreme conditions where the pressure exceeds 100 GPa and the strain rate exceeds 10^6 1/s. Laser ablation dynamically loads a sample, causing a manufactured initial perturbation to grow due to hydrodynamic instability. The instability growth rate depends on the strength of the sample. Material strength can then be inferred from a measurement of the instability growth. Past experiments relied on in-flight diagnostics to measure the amplitude growth, which are not available at all facilities.

Recovery instability experiments, where the initial and final amplitude of the instability are measured before and after the sample is dynamically loaded, obviate the need for in-flight diagnostics. Recovery targets containing copper and tantalum samples coined with 2D (hill and valley) and 3D (eggcrate) initial perturbations were dynamically loaded using the Janus laser at the Jupiter Laser Facility, Lawrence Livermore National Laboratory. The energy of the laser pulse was varied to cover a range of conditions in the dynamically compressed sample, with pressures in the range 10 GPa to 150 GPa and strain rates in the range 10^5 1/s to 10^8 1/s.

The coupling of laser energy into a loading wave was studied with a combination of laser-matter interaction simulations (Hyades) and velocity interferometry data (VISAR). Laser ablation of the recovery targets generated a blast wave, loading the coined initial perturbations with a shock wave followed by a release wave. Different ablator materials and variations in the amount of laser energy deposited in the ablator lead to variations in the loading wave and consequently variations in instability growth.

The growth of the initial perturbation amplitude from initial to final conditions was studied with hydrocode simulations (CTH). During dynamic loading of the sample, the shock wave caused amplitude growth due to hydrodynamic instability. The release wave accelerated the perturbed interface and slowed amplitude growth, in some cases reversing growth.

The sensitivity of the instability growth to coarse changes in the strength model was demonstrated. However, uncertainty in modeling the laser ablation loading prevented a definitive comparison between simulation and experiment.

PUBLISHED CONTENT AND CONTRIBUTIONS

[1] Z. Sternberger et al. “A comparative study of Rayleigh-Taylor and Richtmyer-Meshkov instabilities in 2D and 3D in tantalum”. In: *AIP Conference Proceedings* 1793.1 (Jan. 2017), p. 110006. ISSN: 0094-243X. DOI: 10.1063/1.4971669. URL: http://aip.scitation.org/doi/abs/10.1063/1.4971669.
Z.S. contributed to the experimental results.

TABLE OF CONTENTS

LIST OF ILLUSTRATIONS

LIST OF TABLES

NOMENCLATURE

	Target nomenclature
Ablator	Material used to couple laser energy into a loading wave.
CH	*Polystyrene* Plastic, an ablator material.
Conformal	Target configuration where the ablator is glued to the perturbed surface of the sample so that the glue fills the perturbation troughs.
CRF	*Carbon resorcinol formaldehyde* Carbon aerogel, an ablator material.
LiF	*Lithium fluoride* A window material.
Nonconformal	Target configuration where the ablator is attached to the perturbed surface of the sample so that vacuum remains in the perturbation troughs.
Window	Transparent target component through which an optical velocity diagnostic (VISAR) views the sample.

	Hydrodynamic instability nomenclature
A	*Atwood number* Nondimensional difference in density over an interface between two fluids.
GF	*Growth factor* The ratio of the amplitude due to instability growth to the initial perturbation amplitude.
RTI	*Rayleigh-Taylor instability* Hydrodynamic instability caused by the acceleration of two fluids sharing a perturbed interface.
RTSD	*Rayleigh-Taylor stable dynamics* A term used in this work to differentiate between RTI growth with $A > 0$ and oscillation when $A < 0$, the RTSD case.
RMI	*Richtmyer-Meshkov instability* Hydrodynamic instability caused by a shock transiting the perturbed interface separating two fluids.

	Dynamic compression nomenclature
Bulk pressure	The pressure due to the loading wave, as a function of time, averaged between points 1 μm and 10 μm into the sample material.
EOS	*Equation of state* The relation between the pressure, density, and temperature of a material.
Hydrodynamic approximation	When the strength of a material is insignificant compared to the pressure in the shocked state, the shocked stress state is approximately hydrostatic.
HEL	*Hugoniot elastic limit* The stress in the direction of compression when a material yields under uniaxial strain.
HM	*Hoge-Mukherjee strength model* A strain rate dependent strength model [35].
Hugoniot	The locus of states achievable by shock compression from an initial condition.
LMS	*Lawrence Livermore multiscale strength model* A strain rate dependent strength model [6].

Loading wave	The stress wave generated by laser ablation which travels through the ablator and into the sample.
PTW	*Preston-Tonks-Wallace strength model* A strain rate dependent strength model [68].
Ripple pressure	The maximum bulk pressure due to the passage of the loading wave.
SG	*Steinberg-Guinan strength model* A strain rate independent strength model [80].
SL	*Steinberg-Lund strength model* An extension of the Steinberg-Guinan strength model which adds strain rate dependence [81].

Methods nomenclature

CTH	3D hydrodynamics code used to simulate instability growth [50].
Drive	The use of a laser and an ablator to produce a loading wave.
Drive laser	The laser producing the loading wave by laser ablation.
F	*Hyades factor* Ratio of energy required to produce a ripple pressure in Hyades to the energy required to produce the same ripple pressure experimentally.
Hyades	1D radiation transport and hydrodynamics code used to simulate laser ablation [45].
JLF	*Jupiter Laser Facility* A pulsed laser facility where all experiments were conducted.
ORVIS	*Optically recording velocity interferometer system* Also known as *line-VISAR*, a velocity diagnostic that records spatial as well as temporal information.
PTV	*Peak to valley amplitude* The distance between the peaks and the valleys of the initial perturbation, equal to twice the perturbation amplitude.
VISAR	*Velocity interferometer system for any reflector* A velocity diagnostic.
VPF	*Velocity per fringe* The proportionality between the fringe shift measured by VISAR and the velocity of the surface probed by VISAR.

Chapter 1

INTRODUCTION

Understanding material properties at extreme conditions, a term usually encompassing dynamic compression to states near 100 GPa and strain rates above 10^5 1/s, presents a host of challenges. Hydrodynamic instability experiment in solids driven by high energy lasers have provided access to conditions difficult to create in the laboratory. This work continues the development of hydrodynamic instability experiments in solids and the investigation of material properties at extreme conditions.

1.1 Motivation to study strength models

Metals have a linear elastic response, described by Hooke's Law, up until their yield. The material stores deformation as elastic energy and returns to its original configuration when the load is removed. Beyond yield, work done on the material is irreversible and the solid does not recover to its initial state after load is removed. In order to produce additional deformation, the yield stress must be continually overcome. A material deforming to relax stresses exceeding its yield stress flows plastically, motivating the term *flow stress*, sometimes used in place of the term *yield stress*. The transition from elastic deformation to plastic deformation and the subsequent resistance to plastic deformation are described by a strength model. Together with the laws of conservation of mass, momentum, energy, and an equation of state, the strength model forms a system capable of describing the behavior of a material up to and beyond conditions that cause yield.

Simple strength models, like the elastic-perfectly-plastic model, are appropriate for a wide range of cases. Material strength, however, is not always well described by this model. The strength of a material depends on its thermodynamic state, relating the equation of state to the strength model. The rate of deformation and the degree of deformation, rate hardening, and pressure hardening vary based on material. The initial microstructure of the material also impacts strength. Models appropriate for FCC metals do not accurately describe BCC metals due to differences in dislocation mobility. Consequently, strength is a complex property to model. It is uncertain that a model which is proven for a certain range conditions will be valid under different conditions.

In engineering, it is usually undesirable for materials to yield, but yield is sometimes unavoidable. Extreme conditions are generated in military applications, where the study of armor to defeat weapons and the competing study of weapons to defeat armor require understanding the behavior of solids impacting solids at velocities on the order of 1 km/s, generating pressures on the order of 10 GPa, far in excess of yield strengths on the order of 100 MPa [56].

Refining knowledge of strength at extreme conditions benefits planetary science. Impact events drive the evolution of the solar system. The planets formed from the accretion of material into larger and larger bodies through collisions [1]. The Moon is thought to have formed from a collision of a Mars-sized body with the Earth [12, 32, 13]. Simulations have investigated the formation of craters which pock the surface of the Earth and other bodies [2, 17, 10, 78]. These collisions involve velocities of approximately 10 km/s and pressures on the order of 100 GPa. Even before impact, material models play a role in simulating atmospheric breakup of meteoroids [37]. Understanding how the current state of our solar system came to be and predicting future evolution benefits from modeling these events.

1.2 Review of strength measurements at high strain rates

Models of strength require experimental data for fitting and validation. If the model contains strain rate dependence, validating the model requires experimental data over a range of strain rates. A catalog of stress-strain behavior at various strain rates and initial conditions has been built by Hopkinson bar experiments, reaching strain rates up to 10^4 1/s. The pressures achieved on a Hopkinson bar are limited by the requirement that the incident and transmission bars do not yield and the strain rates are limited by the length of the sample. Hopkinson bar experiments require that the sample be subjected to uniaxial stress, so the length cannot be too small compared to the diameter [29, 25]. Experiments in copper have shown an increase in flow stress near 10^3 1/s [43, 26]. Experiments in tantalum have shown an increase in strength around 10^4 1/s, near the limit of Hopkinson bar experiments [77, 57, 35].

Pressure-shear impact, driven by a powder or gas gun, allow measurement of the strength of the material at higher strain rates than the Hopkinson bar, up to 10^7 1/s [16, 86]. This technique is limited by the requirement that the impactor remains elastic. However, the sample is assumed to be in uniaxial strain, allowing for thinner samples and higher strain rates than in Hopkinson bar experiments. Sample thickness is still limited by the need to approximate bulk material. Pressure-shear

experiments extend data on the strain rate sensitivity of copper strength up to 10^6 1/s [28] and provide some results for tantalum in the 10^6 1/s range [24].

Laser ablation, gas guns, and explosives are capable of driving dynamic compression exceeding 100 GPa [31]. The strain rate in a shock goes as the fourth power of the shock pressure [89], allowing access to higher strain rates through high pressure shocks, but measurement of strength at these extreme conditions is difficult. Possible approaches involve measuring the release profile [80], inferring strength from shock behavior [90], and dynamic diffraction [62]. Together with Hopkinon bar and pressure-shear results, these efforts measure flow stress spanning decades of strain rate (Figure 1.1).

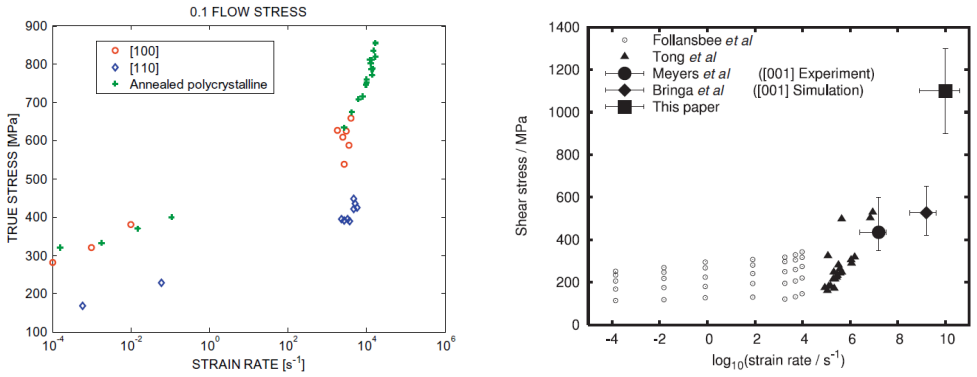

(a) (b)

Figure 1.1: Summary of strength data obtained for tantalum using Hopkinson bar results [76] (a). This plot does not contain results from overdriven shock wave data at 10^9 – 10^{12} 1/s from Swegle and Grady, [82]. Strength data for copper comes from a combination of Hopkinson bar results [26], pressure-shear impact data [87], overdriven shock results [82], MD simulations [9], and laser ablation driven dynamic compression [58, 62], compiled in [62] (b). The higher strength data from Follansbee et al. was taken at higher strains.

This range of data, however, is sparse. Authors have commented on the difficulty of determining material strength during high strain rate deformation, motivating additional study.

- " ... there is great uncertainty in the constitutive response of materials at $\frac{d\varepsilon}{dt} > 10^5$ s^{-1}. Determining which model applies will require experimental data at these high strain rates. Measurements of strength even at the 30 to 50 pct level of accuracy could be helpful here to help establish which mechanism is at play in 10^5 s^{-1} deformations." [73]

- "Despite many decades of study, the response of materials under shock compression at ultra-high strain rates ($10^6 - 10^{10}$ s^{-1}) remains poorly understood." [62]

- "Under these extreme conditions [$P > 100$ GPa, $\dot{\varepsilon} \sim 10^7$ 1/s], material properties and plastic flow dynamics can be significantly different and difficult to predict. Theoretical uncertainties are very large, and relevant experimental data scarce to nonexistant." [63]

1.3 Determining strength with hydrodynamic instability experiments

An additional technique for determining the strength of solids at high strain rate, the hydrodynamic instability experiment, relies on an analogy between plastic flow and fluid flow. Studies of fluids have generated a detailed understanding of two hydrodynamic instabilities: the Rayleigh-Taylor instability (RTI) [85] and the Richtmyer-Meshkov instability (RMI) [75, 54]. The forces driving hydrodynamic instabilities in fluids also drive deformation in solids. Small accelerations only cause elastic deformation. Sufficiently strong accelerations induce plastic deformation and a flow analogous to a fluid. The dynamic loading required to force plastic flow and instability growth also forces the material to a high pressure state and subjects it to high strain rates. The flow stress of the solid resists the instability, modifying the instability growth. The strength of the material can then be inferred by measuring the instability growth, providing a window into the properties of solid in the dynamically compressed state.

Modeling Rayleigh-Taylor instability in solids

Consider two inviscid fluids separated by a planar interface. They are accelerated normal to the interface with magnitude g (Figure 1.2(a)). The acceleration is directed from fluid 1 to fluid 2. The interface is given a small sinusoidal perturbation with wavenumber $k = \lambda/(2\pi)$ and initial amplitude η_0, such that $\eta_0 \ll \lambda$. The interface amplitude grows, with

$$\eta(t) = \eta_0 \exp\left(t\sqrt{Akg}\right) \tag{1.1}$$

$$A = \frac{\rho_2 - \rho_1}{\rho_1 + \rho_2} \tag{1.2}$$

where A is the Atwood number. If $A < 0$, in the case of a heavy fluid accelerated into a light fluid, then the argument of the exponent is complex and the interface

amplitude will oscillate. In this work, this case will be referred to as *Rayleigh-Taylor stable dynamics* (RTSD). Otherwise, the argument of the exponent is positive and the amplitude will grow exponentially, the RTI. As the amplitude grows, the assumption that $\eta_0 \ll \lambda$ will eventually fail. When it does, the dynamics become nonlinear. Shear velocity at the interface turns the initially sinusoidal perturbation into a mushroom shape [42] (Figure 1.2(b)). At later times, the symmetry of the interface breaks down. The heavy fluid falling into the lighter fluid is termed a spike. The lighter fluid rising into the heavier fluid, termed a bubble, slows relative to the spikes, ultimately reaching a constant velocity [30].

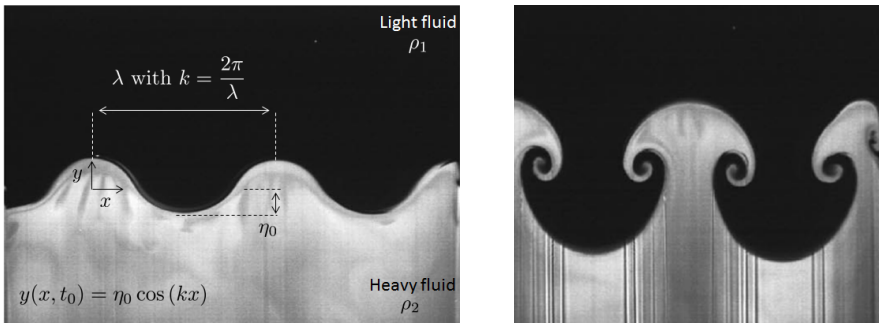

(a) (b)

Figure 1.2: Image of two fluids at the start of an RTI experiment (a). The light fluid is accelerated into the heavy fluid. In this case, the interface perturbation amplitude grows. The shape of the interface in the nonlinear regime is shown in (b) [88].

The analysis has been expanded for a 3D initial perturbation. Jacobs and Catton [39] generalized the initial perturbation to a rectangular perturbation of the form

$$\eta_0 = \sin(k_x x)\sin(k_y y) \tag{1.3}$$

with aspect ratio $L = k_x/k_y$. The perturbations with $L = 1$ grew most quickly. The smaller the aspect ratio, the slower the perturbation grew. All 3D perturbations grew faster than their 2D counterparts with $L = 0$. In order to compare the growth rates of different initial perturbations, the wavenumber $k = \sqrt{k_x^2 + k_y^2}$ is held constant. In part II of their publication, experiments performed by Jacobs and Catton with air and water verified this result and showed that experimentally determined growth rates match linear theory even up to $\eta k \sim 1$ [38]. A higher growth rate for initially 3D perturbations than initially 2D perturbations has been verified in further experiments in fluids [91] and in plasma [49].

Efforts to model the RTI in solid materials quantify the amount strength reduces the RTI growth rate, allowing strength to be inferred from RTI experiments. A model for the evolution of RTI in viscous fluids with surface tension has been developed as a proxy for a plastically deforming solid [60]. This model is expanded by making an analogy between the shear modulus of the solid and surface tension and between the flow stress of the solid and viscosity [18]. This model agrees well with experimental RTI results in aluminum [5, 4], but disagrees with other data from higher strain rate experiments [40], providing insight into unexpected strength behavior. Piriz et al. developed a model of a rigid plastic solid deforming under RTI, resulting in an asymptotic growth rate dependent on the flow stress [66]. Mikaelian has performed further computational work, simulating a RTI experiment in tantalum compressed to nearly 1 TPa [59].

Modeling Richtmyer-Meshkov instability in solids

A shock passing over an interface between two fluids also causes small perturbations in the interface to grow, the RMI. Misalignment in the density and pressure gradients deposits vorticity at the interface. The passage of the shock modifies the material properties at the interface, compressing the two fluids and producing a post shock Atwood number and growth rate which, for small amplitude initial perturbations, is linear with

$$\eta(t) = \eta_0^+ + \left(u_p k \eta_0^+ A^+\right) t \tag{1.4}$$

$$A^+ = \frac{\rho_2^+ - \rho_1^+}{\rho_2^+ + \rho_1^+} \tag{1.5}$$

where the superscript + indicates a quantity in the compressed post-shock material and where u_p is the velocity imparted by the shock [75]. Unlike RTI, the interface is unstable regardless of the sign of A^+. The modified growth rate

$$\eta(t) = \eta_0^+ + \left(u_p k \frac{\eta_0^+ + \eta_0}{2} A^+\right) t \tag{1.6}$$

better predicts experimental results when $A^+ < 0$ [55]. As in RTI, the amplitude grows into a nonlinear regime. The high density spikes outgrow the low density bubbles. Asymptotic limits for both the bubble and spike velocity depend on the

dimensionality of the interface perturbation. As in RTI, 3D perturbations outgrow 2D perturbations [30]. This result has been supported by experiment in fluids [15].

Mikaelian considers viscous RMI where, as in his RTI work, the viscosity can be a proxy for yield strength [60]. Unlike in viscous RTI, the amplitude of viscous RMI saturates. Mikaelian suggests that this amplitude, sensitive to the viscosity of the fluid, could be used to experimentally determine fluid viscosity, and by proxy, solid flow stress. In later work, a relationship between flow stress and viscosity is given and an updated model which closely follows 2D simulation results is described [61].

Elastic-plastic material undergoing RMI has been modeled by Piriz et al. [67]. The strength in a solid material slows the growth of the RMI before arresting growth at a final amplitude. An analytic model determined that the difference between final and initial amplitude is inversely proportional to Y, the flow stress. Simulations of an elastic-plastic material follow the predicted inverse relationship, with

$$\eta_f = \eta_0 + 0.29\frac{\rho u_p^2}{kY}, \tag{1.7}$$

where η_f is the final amplitude. While Piriz et al. developed this model for the $A^+ > 0$ case, the inverse scaling with Y has been validated by subsequent MD and hydrodynamic simulations for the $A^+ < 0$ case [22].

Review of hydrodynamic instability experiments in solids

Experimental determination of material strength by observing hydrodynamic instability growth was pioneered by Barnes et al. in 1973 [5]. Initial perturbations machined into aluminum were accelerated by low density explosion products, loading the sample to approximately 10 GPa and causing the perturbation amplitude to grow due to RTI.

More recently, high energy laser facilities have been used to ramp compress aluminum, tantalum, and vanadium samples to approximately 100 GPa and drive RTI [40, 64, 65, 63]. By loading the sample as isentropically as possible, the sample is guided to a high pressure state while remaining solid, producing strain rates of approximately 10^7 1/s. Differences between experimental results and simulations using standard strength models indicate inaccuracies in the standard strength models at these conditions (Figure 1.3). While current models describe strength as sensitive to microstructure, experiments at 10^7 1/s show little sensitivity to microstructure [63].

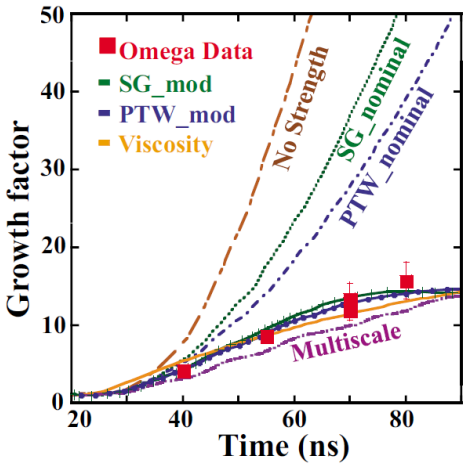

Figure 1.3: Comparison of simulations of RTI growth in a vanadium sample with a range of strength models, compared to experimental results [64]. Growth factor is the ratio of the amplitude due to instability growth to the initial perturbation amplitude.

Instability growth due to RMI has also been studied in solids, but only for the $A^+ < 0$ case. Experiments in copper shocked at 36 GPa produced RMI growth of initial perturbations [11]. RMI was shown to be sensitive to material strength [22] and an existing strength model for copper to was shown to underestimate experimentally determined strength [69]. As the instability occurs on the rear surface of the sample, the high pressure behind the shock releases immediately, so these experiments test strength at high strain rates (approximately 10^7 1/s), but at low pressure.

In fluids, the nonlinear evolution of the instability depends on the shape of the initial perturbation. Lebedev et al. conducted RTI experiments and simulations in solids, using a setup similar to Barnes et al., with 2D and 3D initial perturbations [46]. Contrary to the RTI in fluids, the 2D initial perturbations grew more than 3D initial perturbations. Dimonte et al. performed RTI experiments on an elastic-plastic yogurt and found that 3D perturbations were more stable than 2D perturbations [21].

1.4 Motivation for a recovery hydrodynamic instability experiment

RTI laser experiments require that the laser ablation drive loads the sample to a high pressure solid state without shocks. Lasers deposit energy on a density-graded ablator, creating a shock which breaks out into a vacuum gap between the ablator and the sample. The rush of ablation products stagnates on the sample. The more ramp-like the drive, the more isentropic the compression is, leading to higher pressures in

the solid phase. Decreasing the thickness of the sample results in higher acceleration and faster RTI growth rates. In-flight diagnostics are necessary to image the growth of the initial perturbation before the target is destroyed.

Decreasing the complexity of this experiment is desirable. First, the requirement of an approximate ramp loading can be relaxed. Ramp loading requires density-graded ablator designs and accurate laser pulse shaping. Instead, a short laser pulse depositing energy on an ablator held in contact with a sample drives a blast wave, a shock followed by a release, into the ablator-sample interface. Blast loading is easier to produce, requiring neither graded ablator nor accurate pulse shaping. The shock leading the blast wave excites RMI, which can be used to grow initial perturbations in a hydrodynamic instability experiment.

Second, no in-flight diagnostics are required if the sample can be recovered and analyzed after the experiment. Material strength arrests instability growth and preserves the final amplitude. The final amplitude can then be compared to simulations of the instability growth, as long as the loading and initial perturbation is well understood. Recovering the sample puts upper bounds on the strength of the blast loading. Too strong a blast and the shocked sample will melt on release. Using RMI instead of RTI removes the need to accelerate the sample to cause growth, so the sample does not need to be thin. A thick sample protects against spall and prevents reflections from the rear surface of the sample from interacting with the perturbed interface.

With these changes, the experiment transforms from a delicate sample probed by high speed diagnostics during a violent acceleration into a robust sample shocked by a blast wave and recovered (Figure 1.4).

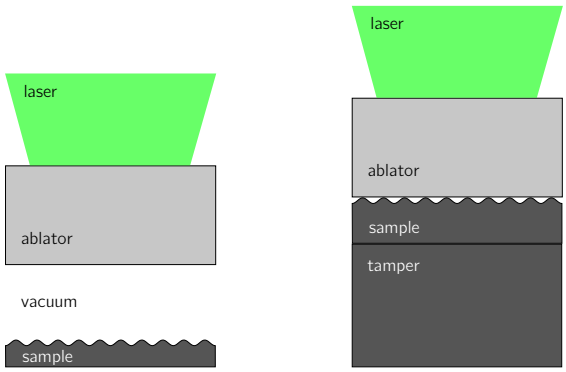

Figure 1.4: Comparison of an RTI-style target (a) and the RMI recovery target used in this work (b).

1.5 Outline of thesis

This goal of this work is to further development of hydrodynamic instability experiments as a tool to infer strength. Experiments were conducted to constrain the strength of two materials: copper and tantalum. Both copper and tantalum have been well characterized by other experiments in the $< 10^5$ 1/s strain rate range, providing a useful base of knowledge to compare against this work. However, understanding of flow stress in the $10^6 - 10^9$ 1/s range is sparse. Laser ablation was used to drive RMI recovery experiments, accessing strain rates near 10^6 1/s and pressures near 100 GPa.

An experimental campaign in 2014 produced a set of instability growth results in tantalum with two different initial perturbation patterns. A second experimental campaign in 2015 produced a set of instability growth results in copper, also using two different initial perturbation patterns. A subset of the copper targets were loaded from an elevated temperature.

In Chapter 2, fundamentals of shock modeling will be discussed to help explain concepts in dynamic compression experiments. Basic analytic techniques aid in understanding the 1D shock propagation that appears in the hydrodynamic instability experiments. Material models developed for the high pressure and high strain rate conditions in this work, including specific strength models, are reviewed.

In Chapter 3, the target design used to recover instability growth in a tantalum or copper sample is presented. The laser facility where the experiments were performed is described, as are the diagnostics required to characterize the dynamic compression and the recovered instability growth. The preheat capability of the target mount is discussed.

In Chapter 4, the numerical methods required to infer material strength from the recovered growth are introduced. The laser ablation drive is studied with simulations of laser-matter interaction. The laser ablation simulations are calibrated to experimental results, producing a tool to mimic experimental conditions in 2D and 3D hydrodynamic instability simulations.

In Chapter 5, calibrated laser ablation simulations are used to understand the loading imposed on the sample. The instability growth is simulated in 2D and 3D and the sensitivity of the growth to the strength model is tested. Trends in the simulations results are used to interpret experimentally determined instability growth.

In Chapter 6, results are compared to the existing knowledge of strength of copper

and tantalum. Remaining problems with the experimental and simulations are discussed and possible solutions are presented.

Chapter 2

SHOCK WAVE MODELING

In experiments, hydrodynamic instability growth is driven by dynamically compressing the sample material. This chapter gives an overview of dynamic compression and material models accurate under dynamic compression. Numerical studies using these models aid in understanding the compression of the sample.

2.1 Background on shock waves

The sound speed in a media is a function of the state of the media, with

$$c^2 = \frac{\partial P}{\partial \rho} \quad \text{and typically with,} \quad \frac{\partial c}{\partial \rho} > 0. \tag{2.1}$$

The inequality, if it holds, results in a sound speed that increases when the material is compressed. As long as the derivative of sound speed with respect to density is nonzero, wave behavior may become nonlinear. In a typical 1D example, consider a piston compressing ambient media. The media communicates the compression by launching waves from the piston face into the ambient media. Compression raises the sound speed, so waves communicating further pressure increases by the piston will catch up to waves launched earlier in time. This staking up of waves forms a shock wave, a nearly discontinuous change in the state of the material [19].

To model the shock wave, the conservation laws are simplified over a discontinuous jump resulting in the Rankine-Hugoniot jump conditions. The shock moves at velocity u_s into a media with initial velocity u_0, modifying the state of the medium from state 0 to state 1 as it passes. In a frame following the shock, the velocity is written relative to the shock velocity as $\overline{u}_i = u_i - u_s$. For shocks considered in this work, $u_0 = 0$ and u_1, the velocity induced by the shock, is referred to as the particle velocity u_p. The general and reduced forms of the conservation laws are,

Conservation of mass

$$\rho_0 u_0 = \rho_1 u_1 \tag{2.2}$$

$$\rho_0 u_s = \rho_1 (u_s - u_p) \tag{2.3}$$

Conservation of momentum

$$P_0 + \rho_0 \overline{u}_0 u_0 = P_1 + \rho_1 \overline{u}_1 u_1 \tag{2.4}$$

$$P_0 + \rho_0 u_s u_p = P_1 \tag{2.5}$$

Conservation of energy

$$P_0 u_0 + \rho_0 \left(\frac{1}{2} u_0^2 + e_0 \right) \overline{u}_0 = P_1 u_1 + \rho_2 \left(\frac{1}{2} u_1^2 + e_1 \right) \overline{u}_1 \tag{2.6}$$

$$P_0 V_0 + e_0 + u_p \left(u_s - \frac{u_p}{2} \right) = P_1 V_1 + e_1 \tag{2.7}$$

where V if the specific volume, P is the pressure, and e is the specific internal energy. Equation 2.5 is a variation of conservation of momentum using the conservation of mass. Equation 2.7 is a variation of conservation of energy using the other conservation laws. These conservation equations do not include any effects of viscosity or heat transfer. While these mechanism are necessary to form a physical shock wave, they are not necessary for this shock wave model where a mathematical discontinuity is imposed in the flow [92]. Despite lacking explicit dependence on these irreversible mechanisms, the conservation laws predict a rise in entropy over the shock.

The conservation laws for momentum and energy can be combined to form the Hugoniot relation,

$$e_1 - e_0 = \frac{1}{2}(P_0 + P_1)(V_0 - V_1). \tag{2.8}$$

The change in specific internal energy can be thought of the work accomplished by the average pressure between states 0 and 1 performing the compression from state 0 to state 1.

The locus of states 1 reached in shock compression from state 0 is called *the Hugoniot*. Generally, it is assumed the initial state is at standard conditions. Sometimes, when considering shock compression from a preheated or precooled state, it is not certain if the term Hugoniot refers to standard conditions or some other initial state. In this circumstance, the term *the principle Hugoniot* is used to distinguish the locus of states reached from standard conditions. While standard conditions assume atmospheric pressure, no distinction is made if the initial pressure is zero (dynamic compression experiments commonly require vacuum) because atmospheric pressure is insignificant compared to the pressure in the shocked state, usually > 1 GPa. Consequently, $P_0 = 0$ in most uses of the Rankine-Hugoniot jump conditions.

Combining Equations 2.3 and 2.7 expresses the shock wave speed as,

$$u_s = V_0\sqrt{\frac{P_1 - P_0}{V_0 - V_1}} \tag{2.9}$$

and allows the shock speed to be determined easily from a plot of the Hugoniot in $P - V$ space. In this section, the pressure P refers to the stress in the direction of shock propagation. To be more descriptive, the stress tensor σ_{ij} can be used to represent the full stress state of the material. For an inviscid fluid, this P is the hydrostatic pressure and $\sigma_{ij} = -P\delta_{ij}$. Assuming the shock is aligned in this example so that σ_{11} bears the load, $\sigma_{11} = -P$.

2.2 Shock waves in solids

Solid materials, unlike fluids, can support shear deformation. Up until yield, deformation is born elastically and linearly. It is revealing to decompose the stress tensor σ_{ij} into a hydrostatic pressure P and a deviatoric stress tensor S_{ij},

$$\sigma_{ij} = S_{ij} + P\delta_{ij} \qquad P = -\frac{1}{3}\sigma_{kk}, \tag{2.10}$$

where the negative sign maintains consistency between the stress tensor, positive in tension, and the pressure, positive in compression. It is easier to discuss $-\sigma_{ij} = -S_{ij} + P\delta_{ij}$, the compression at the shock front, where $-\sigma_{ij} > 0$, $-S_{ij} > 0$, and $P > 0$ for compression.

Consider planar shock loading, producing a state of uniaxial strain in the ε_{11} direction. Uniaxial strain caused by shock compression is described in great detail in literature. A small sampling is [74, 36, 20]. As all other strains are zero, $\varepsilon_{11} = \varepsilon_{kk} = \Delta V/V$. While the strain is uniaxial, the stress is not. The volumetric deformation produces a rise in the hydrostatic pressure through the bulk modulus K. Shear stresses are supported by $-S_{ij}$ through the shear modulus G. As $-\sigma_{11} = -S_{11} + P$, $-\sigma_{11}$ increases more quickly than P as the material is compressed. The linear constitutive relation results in a single elastic wave speed. Under sufficient compression, material will yield and the deviatoric tensor will be unable to support additional stress.

Beyond yield, additional stresses cannot be stored elastically. The solid relaxes any additional shear stresses through plastic flow and bears the additional compression

hydrostatically [20]. The stress in the direction of compression at yield is referred to as the Hugoniot elastic limit (HEL). Because the $-S_{11}$ component of $-\sigma_{11}$ stops bearing additional stress beyond yield, the slope of the constitutive relation $-\sigma_{11}(\varepsilon_{11})$ decreases at yield.

Compression beyond yield launches an elastic wave carrying the HEL stress at the elastic wave speed, known as the elastic precursor. The remainder of the stress is carried by a plastic wave traveling at a slower velocity due to the decrease in slope of the constitutive relation at the HEL.

As the compression increases, the flow stress may change. Figure 2.1 depicts a weakening of the material under compression. The difference between the hydrostatic pressure P and the Hugoniot stress $-\sigma_{11}$, equal to $2Y/3$, decreases with compression. When the compression exceeds the stable shock threshold (Figure 2.1), the plastic wave speed exceeds the elastic wave speed and there is no distinct elastic precursor, producing what is referred to as an overdriven shock.

For even higher compression, the $-S_{11}$ term will become small with respect to the pressure and $-\sigma_{11} \sim P$. Beyond this level of compression, the Rankine-Hugoniot relations can be used with the hydrostatic P only, ignoring the $-S_{11}$ contribution. This simplification is called the *hydrodynamic approximation* and is commonly made for metals when the compression exceeds 10 GPa, roughly two orders of magnitude higher than their strength [20].

2.3 Shock transmission and reflection

Simple 1D wave propagation problems can largely be broken down into shock waves interacting with interfaces or free surfaces. When a wave encounters an interface, a wave is reflected and a wave is transmitted. At the interface, each material achieves equilibrium in stress and particle velocity. If the materials are different, the state in each material will differ. The solution to matching these conditions has a graphical interpretation (Figure 2.2). In this illustration, the shock takes the media from initial state 1 to state 2. The Hugoniot of each material (A and B) is plotted in $P - u_p$ space to help match these two variables at the interface.

The initial shocked state resides somewhere on the Hugoniot of the transmitting material A. In Figure 2.2, the shock impedance $\rho_0 u_s$ of A is lower. The transmitted shock will shock B to some point on its Hugoniot. The mutually achieved state is found by reflecting the Hugoniot of A (curve AR) and finding the intersection of AR with B [56]. The resulting state is higher pressure, but lower particle velocity, than

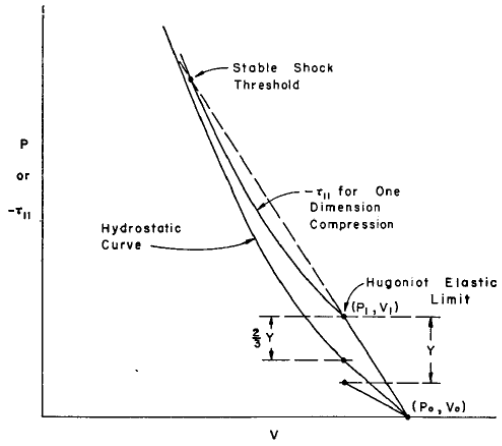

Figure 2.1: Plot of the pressure P and the stress σ_{11} in the case of uniaxial strain. The solid supports additional shear linearly up until the Hugoniot elastic limit. The decrease in offset between the hydrostatic curve and the stress indicates that this material softens with compression. At the end of compression shown on the plot, the plastic wave speed exceeds the elastic precursor wave speed and a single overdriven shock is formed [74].

the incident state.

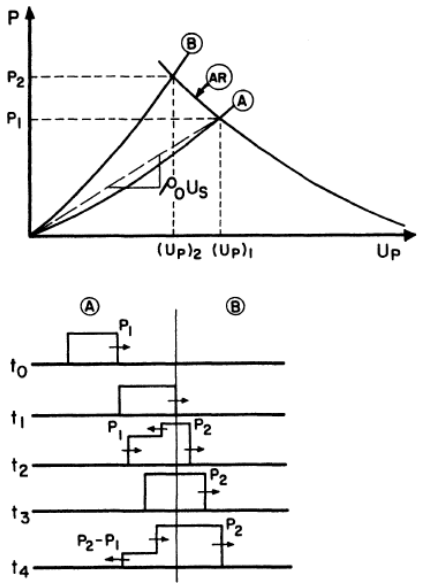

Figure 2.2: Illustration of the impedance matching graphical method for a shock going from a low impedance material to a high impedance material [56].

This technique can be used to understand the reflection of a wave from a free surface. In this case, the shocked state unloads all the way down the reflected Hugoniot. As the reflection is symmetric about the shocked state, the reflected state is at $P_2 = 0$

and $u_{p2} = 2u_{p1}$. However, the release is an isentropic process that is not identical to the irreversible shock compression described by the Hugoniot. The validity of this assumption has been found to be good in metals for compressed states with $P < 50$ GPa [74].

Determining the free surface velocity at shock break out, commonly with an optical diagnostic like VISAR, is an important experimental tool for measuring shock properties. For sufficiently strong shocks, the uncertainty introduced by the difference between the isentrope and the reflected Hugoniot can be alleviated by using a window, a transparent material that the sample releases into instead of a vacuum. If the Hugoniot of the sample and the window are not too different, then the difference between the reflected Hugoniot and the isentrope, and the error in the measured breakout velocity, is minimized.

2.4 Background on hydrocodes

Numerical codes designed to simulate solid mechanics at conditions where the hydrodynamic assumption is valid are called hydrocodes. Hydrocodes solve the conservation laws, closed by a two-part constitutive relation [56]. One part, the equation of state (EOS), describes the relation between the pressure P, density ρ, energy E, and temperature T of the material. The second part, the strength model, describes the yield surface and consequently the flow stress. Generally, strength is dependent on pressure and temperature, relating the two models.

2.5 Equations of state for hydrocodes

In most engineering applications, solids are modeled with a single constitutive relation, for example Hooke's law, linking the full stress tensor to the full strain tensor. Under the hydrodynamic assumption, the stress tensor is dominated by the hydrostatic pressure, so it is more natural to think of materials as fluids possessing an EOS in the form $P = P(e, V)$.

The Hugoniot equation of state

A wide range of materials have an experimentally determined u_s that is nearly linear in u_p [74]. Data from shock compression experiments are fit to the equation,

$$u_s = su_p + c_0 \tag{2.11}$$

known as the Hugoniot EOS of the material. No definitive explanation has been

given for the wide ranging applicability of this simple linear model [52]. Under the hydrodynamic assumption, the jump conservation laws can then determine the thermodynamic variables in the shocked state. In a dynamic compression experiment, u_p and u_s are much easier to measure than P and V. For example,

$$P_1 = P_0 + \rho_0 u_p (s u_p + c_0), \tag{2.12}$$

where the shocked pressure is determined from the initial condition, the Hugoniot for the shocked material, and the particle velocity behind the shock. Writing the pressure as a function of density along the Hugoniot,

$$P_1 = \frac{c_0^2 \rho_0 \rho_1 (\rho_1 - \rho_0) + P_0 \left(s(\rho_0 - \rho_1) + \rho_1\right)^2}{\left(s(\rho_0 - \rho_1) + \rho_1\right)^2} \tag{2.13}$$

demonstrates the singularity at $s = (1 - \rho_0/\rho_1)^{-1}$. For metals, s is around 1.5, so the maximum compression allowed by the Hugoniot EOS is approximately 3. This singularity is not physical and the simple linear Hugoniot should not be extrapolated to model large compression. In some applications, a higher order fit to the Hugoniot is used instead.

The Hugoniot EOS is an appropriate model for many solids, but is only applicable to states that can be reached by shock compression. A given Hugoniot is also only relevant to a specific initial conditions. If the initial conditions are, for example, hotter or higher pressure than standard conditions, then the principal Hugoniot will not describe the shocked state. More complex equations of states, based on the principal Hugoniot, give predictions of the state at conditions off the principal Hugoniot.

The Mie-Grüneisen equation of state

The Grünesien parameter Γ, defined by

$$\Gamma = V \left.\frac{\partial P}{\partial e}\right|_V = -\frac{V}{T} \left.\frac{\partial T}{\partial V}\right|_S = \frac{\beta K_s}{C_P}, \tag{2.14}$$

links the energy and the pressure of the material, expressed in terms of the coefficient of thermal expansion β, the isentropic bulk modulus K_s, and the specific heat at

constant pressure C_P [52, 53]. For metals, Γ is empirically shown to be insensitive to temperature and follows the approximation,

$$\frac{\Gamma(V)}{V} = \frac{\Gamma_0}{V_0} \tag{2.15}$$

[52, 51], so only the Grüneisen parameter at the reference state Γ_0 is needed. The Mie-Grüneisen EOS is defined as,

$$P(V, e) \approx P_{\text{ref}}(V) + \frac{\Gamma_0}{V_0}(e - e_{\text{ref}}(V)), \tag{2.16}$$

where the reference state at P_{ref} and T_{ref} is taken from some known state of the material. The principal Hugoniot is a natural source of reference states when using the Mie-Grüneisen EOS to model shock compression. The Mie-Grüneisen EOS gives access to states that are off the Hugoniot by relating them to the Hugoniot state at the same volume [52, 27, 56].

This relationship does not contain any information about temperature. First, the temperature along the reference curve can be integrated numerically from the relation,

$$\frac{dT_{\text{ref}}}{dV} + \frac{\Gamma}{V}T_{\text{ref}} = \left(P_{\text{ref}} + \frac{de_{\text{ref}}}{dV}\right)\frac{1}{C_V} \tag{2.17}$$

[52]. Then the Mie-Grüneisen EOS can be expanded to a temperature based on the reference curve temperature. Assuming a constant specific heat,

$$T(V, e) = \frac{e - e_{\text{ref}}}{C_V} + T_{\text{ref}} \tag{2.18}$$

[52].

The Mie-Grüneisen EOS will be less accurate at higher compression. Because the EOS is defined with respect to the Hugoniot, the maximum compression of a Mie-Grüneisen material is limited. The assumption that Γ is independent of T and the assumption of constant C_V will also start to break down at higher compression. Example parameters for the Mie-Grüneisen EOS are given in Table 2.1.

Table 2.1: Parameters for the Mie-Grüneisen EOS with a linear Hugoniot reference curve [79].

		Tantalum	Copper	Lithium Fluoride	Polystyrene
ρ_0	g/cc	16.69	8.93	2.638	1.046
c_0	km/s	0.341	0.394	0.515	0.189
s		1.2	1.489	1.35	2.965
Γ_0		1.67	2.02	1.69	0.67
C_p	J/kg·K	135	383	1560	

The Sesame library

The Sesame library is a collection of tables, compiled by Los Alamos National Laboratory, describing the states of a given material [7]. Two tables, $e(V,T)$ and $P(V,T)$ defined over a grid of points in V and T, set the EOS of a material. When the governing equations are integrated, these tables are interpolated to determine the states of the simulated materials [7, 52].

The data in the tables are drawn from a variety of sources. Consequently, a Sesame EOS can describe a wide range of conditions without suffering the drawbacks of using a single model with a limited range of validity [52]. Secondary EOS models modify the primary Sesame EOS. One such model, the P-α porosity model, modifies the Sesame EOS for a bulk material to account for porosity [33]. Porosity is described by $\alpha = V/V_0$ where V is the specific volume of the porous material and V_0 is the specific volume of the bulk material.

2.6 Strength models for hydrocodes

A variety of constitutive relations have been proposed to handle high pressure and high strain rate conditions, reviewed by [72]. The Zerilli-Armstrong (ZA) model [93], the Preston-Tonks-Wallace (PTW) model [68], the Steinberg-Guinan (SG) model [80], the Steinberg-Lund (SL) model [81], and the Lawrence Livermore Multiscale model (LMS) [6] are a sampling.

The SG and SL models are based on the assumption that rate limiting effects saturate above a critical strain rate. The PTW, ZA, and LMS models predict that strength will continue to increase with strain rate.

Strain rate dependence in all of these models is based on dislocation motion. Dislocations moving to relax stress manifest in the material as plastic flow. When the stress is low, dislocations snap from lattice position to lattice position, awaiting

thermal fluctuations to help them over the potential barriers. When the dislocations glide between barriers, they are subject to a drag force. This regime is referred to as either the *thermal activation* regime or the jerky glide regime. When the driving stress is sufficiently high, the potential barriers do not halt dislocations, leading to a *phonon drag* or continuous glide regime where drag effects become dominant [71, 56].

This work will consider the SG and SL models in more detail. Despite handling high strain rate dependence differently than the more modern PTW and LMS models, agreement with these models and hydrodynamic instability experiments has been achieved by using a strengthened SG model, where the strength is increased by some constant multiple [64].

The Steinberg-Guinan strength model

The SG strength model is similar to a Taylor series expansion of the yield surface with respect to P and T, intended to capture the increase of Y and G with pressure and their decrease with temperature. A power law captures work hardening. A limit is set on the maximum value of Y attainable.

$$G = G_0 \left[1 + \frac{1}{G_0} \frac{\partial G}{\partial P} \frac{P}{\eta^{1/3}} - \frac{1}{G_0} \frac{\partial G}{\partial T} (T - 300\text{K}) \right] \tag{2.19}$$

$$Y = Y_0 [1 + \beta(\epsilon_p + \epsilon_{p0})]^n \frac{G}{G_0} \tag{2.20}$$

$$Y_0 [1 + \beta(\epsilon + \epsilon_i)]^n \leq Y_{\max}, \tag{2.21}$$

where ϵ_p is the equivalent plastic strain, ϵ_{p0} is the initial equivalent plastic strain, $\eta = V_0/V$ is the compression, $Y_{\max}$ is the maximum yield strength allowed, and β and n are work hardening parameters [80]. Example parameters for copper and tantalum are given in Table 2.2.

The Steinberg-Lund strength model

The SL strength model is a modification of the SG model, including strain rate dependence below a critical strain rate. Above the critical strain rate, the strength saturates and the SL model reduces to the SG model. The SL model decomposes the yield strength into two terms:

$$Y = \left[Y_T(\dot{\epsilon_p}, T) + Y_A f(\epsilon_p) \right] \frac{G(P,T)}{G_0}, \tag{2.22}$$

where Y_T is the portion that is dependent on the temperature and strain rate and Y_A is rate independent.

The rate dependence included in the model is based on the Hoge and Mukerjee strength model (HM) [35, 81]. The HM model was derived to capture strength data for tantalum obtained up to a strain rate of 10^4 1/s, taking into account the thermal activation and phonon drag mechanisms. Both mechanisms are always active, meaning HM models strength in the jerky glide regime.

The thermal term Y_T is defined with respect to the stain rate by

$$\dot{\epsilon_p} = \left\{ \frac{1}{C_1} \exp\left[\frac{2U_k}{kT} \left(1 - \frac{Y_T}{Y_P} \right)^2 \right] + \frac{C_2}{Y_T} \right\}^{-1}, \tag{2.23}$$

where Y_P is the Peierls stress, the minimum driving stress required for dislocations to glide over the lattice barriers at $T = 0$ K, $2U_k$ is the energy required to form a pair of kinks in a dislocation of length L, and k is the Boltzmann constant. A limit is imposed on the rate dependence of strength, $Y_T \leq Y_P$. As in the SG model, the strain rate independent strength is limited by $Y_A f(\epsilon_p) \leq Y^{\star}_{\max}$. The constant C_1 is related to the thermal activation mechanism and the constant C_2, proportional to the drag coefficient, is related to the phonon drag mechanism.

The model for G and the athermal term Y_A follow the SG model, with

$$f(\epsilon_p) = \left(1 + \beta(\epsilon_p - \epsilon_{p0})\right)^n, \tag{2.24}$$

which is the same work hardening function used in the SG model.

Problems with strength model calibration at extreme conditions

The sparseness of available dynamic strength data, discussed in Section 1.3, affects the calibration of strength models. Strength models are unconstrained and consequently disagree with each other.

In calibrating the PTW model, flow stress is interpolated between high strain rate overdriven shock data and lower strain rate Hopkinson bar data, a five decade gap without validated data, Figure 2.3. This strain rate range is of importance because the transition between the dominance of thermal activation and phonon drag mechanisms occurs here.

Table 2.2: Parameters for the Steinberg-Guinan strength model and additional parameters used by the Steinberg-Lund strength model [79].

		Tantalum	Copper	Lithium Fluoride
G_0	GPa	69.0	47.7	49.0
Y_0	GPa	0.77	0.12	0.36
$Y_{\max}$	GPa	1.10	0.64	0.36
β		22	36	0
n		0.283	0.45	0
$\frac{1}{G_0}\frac{\partial G}{\partial P}$	TPa^{-1}	14.5	28.3	50
$-\frac{1}{G_0}\frac{\partial G}{\partial T}$	kK^{-1}	0.13	0.377	0.618
T_{m0}	K	4340	1790	1480
γ		1.67	2.02	1.69
a		1.3	1.5	1.4
C_1	s^{-1}	$0.71 \cdot 10^6$		
C_2	MPa·s	0.0024		
U_k	eV	0.31		
Y_P	GPa	0.82		
Y_A	GPa	0.375		
$Y^\star_{\max}$	GPa	0.45		

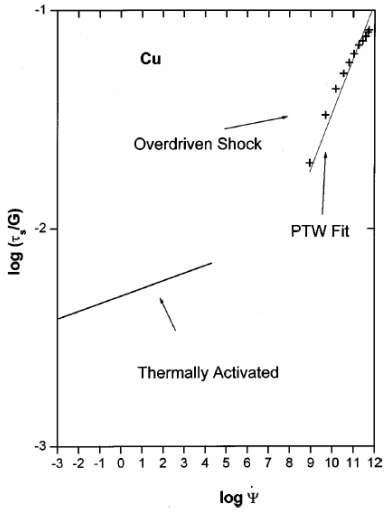

Figure 2.3: Overdriven strength data used to fit the copper PTW model, [68]. A multi-decade gap in flow stress data leaves the fit unconstrained.

Compared to a modification of SL where the upper limit on strain rate hardening is removed to prevent flow stress saturation [72], the PTW model disagrees over the critical strain rate at which thermal activation transitions to phonon drag by orders of magnitude [64] (Figure 2.4). Sparseness of data on strength of metals at strain rates above 10^5 1/s motivates further study.

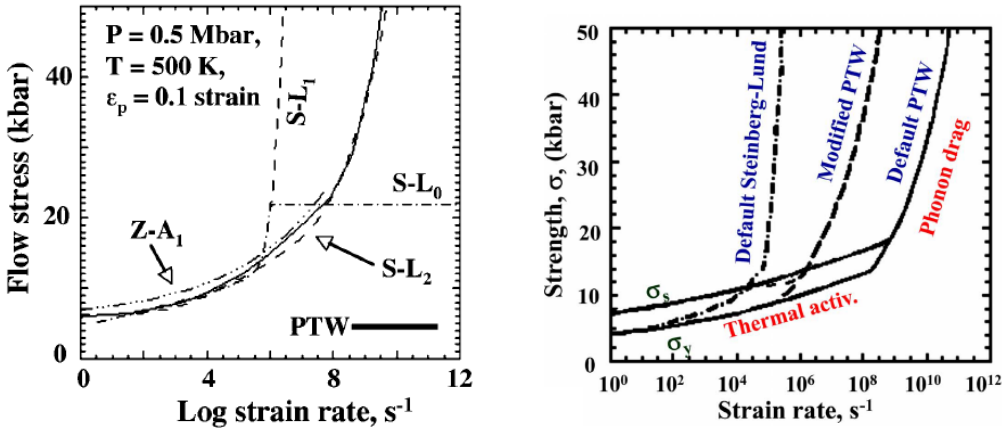

(a) (b)

Figure 2.4: Disagreement in strength models for tantalum from [72] at conditions representative of a dynamic compression experiment, where Z-A_1 (ZA with pressure hardening), S-L_0 (SL), S-L_1 (SL with no saturation, $\sigma \sim \dot{\varepsilon}$), and S-$L_2$ (SL with no saturation and $\sigma \sim \dot{\varepsilon}^{1/4}$ to match PTW) are variations of the ZA and SL models, intended to produce better agreement in the models (a). Disagreement in flow strength models used by [64] to simulate high strain rate behavior of vanadium (b).

Chapter 3

EXPERIMENTAL METHODS

The recovery targets used in this work were designed to couple energy from a pulsed laser into the sample, accelerate the perturbed interface of the sample, and preserve the sample so that it could be recovered after the experiment. The recovered perturbation was measured and compared to a record of the initial perturbation to determine the magnitude of the instability growth. The velocity diagnostic VISAR was used to understand the loaded state of the sample during instability growth.

3.1 Dynamic compression using laser ablation

Pulsed lasers are capable of rapidly depositing energy on a target material. The target material is heated and expands, forming a plume of plasma. The rush of plasma away from the target increases pressure in the target by momentum conservation, like a rocket producing thrust [47, 48].

The effectiveness of the laser-matter energy coupling depends on the material being ablated. A material with desirable ablation properties, the *ablator*, is attached to the sample. The laser then couples with the ablator and generates a *loading wave* which propagates through the ablator into the sample. The assembly of the ablator and sample is termed the *target*. The use of a laser and an ablator together to produce a loading wave is termed a laser ablation drive, or simply a *drive*. The laser producing the drive is termed the *drive laser*.

The pressure generated by the laser-matter interaction scales with the intensity of the laser and the wavelength of the laser,

$$P[\mathrm{MBar}] = 40\left(\frac{I[\mathrm{W/cm^2}]}{\lambda}\right)^{\frac{2}{3}}, \tag{3.1}$$

where I is the laser intensity and λ is the laser wavelength. This result is derived from data collected during direct drive spherical implosion experiments [47]. Other work, considering a planar shock generated by the ablation of plastics, also found that ablation pressure scales as a power law of laser intensity, with

$$P[\text{GPa}] = 8.614 \left(I[\text{PW/m}^2] \right)^{0.833} . \tag{3.2}$$

This scaling was determined from simulations of ablation of a parylene-D ablator with a 10 ns square pulse of laser light [83].

Differences in the laser and experimental setup are expected to alter the constants in the power law. However, the general power law scaling is assumed to hold for peak pressures generated by laser ablation.

3.2 Sketch of a recovery hydrodynamic instability experiment

During a RMI recovery target experiment, the ablator couples laser energy into the target, producing a loading wave, Figure 3.1. The shock leading the loading wave causes RMI and the amplitude of the initial perturbations grow. However, the growth rate rapidly decreases from the classic supported shock case of RMI as the release portion of the loading wave accelerates the heavy sample into the light ablator. This acceleration results in RTI with negative Atwood number, the stable RTSD case, and the growth of the initial perturbation slows or reverses. Meanwhile, the loading wave travels through the sample and into the tamper, attenuating to a point where reflections of the shock will not interfere with the instability growth. Ideally, the RTI does not reverse all of the growth from the RMI. During the experiment, the perturbation plastically deforms, so the target can be recovered and cleaned, and the final perturbation amplitude measured and compared to a record of the initial perturbation amplitude.

3.3 Recovery target and drive target design

To understand strength as a function of the state, the conditions produced by loading wave must be known. The most useful available measurement is the laser energy deposited on the ablator. Increasing laser energy increases the pressure in the loaded state. It is assumed that the scaling of ablation pressure with laser energy can be approximated by laser ablation simulations. However, measurements of the shocked state are necessary to calibrate the scaling.

A common method of determining the shocked state in a sample is to measure the particle velocity in the sample material using VISAR, a velocity interferometry technique. Once the particle velocity is known, an equation of state for the material, like the Hugoniot, gives the shocked pressure. However, VISAR requires reflecting

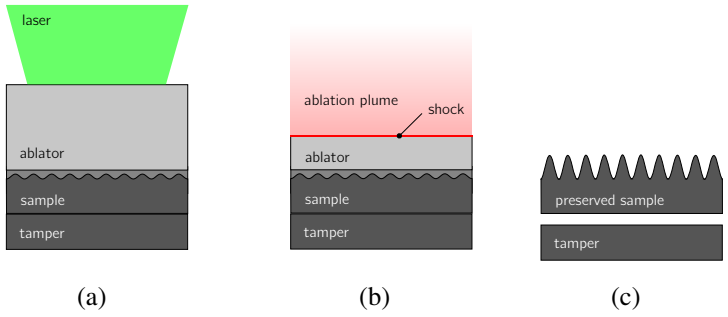

Figure 3.1: Diagram of the experiment. The coined sample is attached to a tamper and an ablator (a). During the experiment, a laser strikes the ablator, launching a shock wave through the ablator and into the sample (b). The shock wave drives a hydrodynamic instability in the initial perturbation, causing the amplitude to grow (c).

a probe laser off an interface of the sample material. In order to access the shock state near the initial perturbation, the sample material must be thin contrary to the requirements for a robust recovery target.

To get around this conflict, two styles of target were used. The first, the *recovery target*, contained a thick sample and a tamper to protect the sample against damage. The recovery targets sketched in Figure 3.2 satisfied these considerations.

The choice of ablator material influences the laser energy coupling to the target and the instability dynamics. Plastic is commonly used as an ablator and the loading generated by the ablation of plastic has been studied [83].

A plastic ablator also benefits the hydrodynamics of the experiment. Ablated plastic has negligible strength, so any instability growth depends on the strength of the sample only. A low density ablator increases the Atwood number at the ablator-sample interface, increasing the growth rate of the instability. Polystyrene (CH) with density of 1.04 g/cc was chosen as the ablator for tantalum targets during the 2014 campaign. A preheated sample would damage a CH ablator, however. Carbon resorcinol formaldehyde (CRF) foam with a density of 100 mg/cc was used for the copper targets in the 2015 campaign.

Targets were assembled using glue. If the glue has negligible strength, it can be applied between the ripples and the ablator, the *conformal* configuration. If the glue is strong, it cannot be applied directly to the ripples because it would affect the instability growth. In this case, the glue was applied to the sides of the target, leaving a vacuum gap between the ripples and the ablator, the *nonconformal* configuration

(Figure 3.2). In experiments without a preheated sample, a weak glue was used. A heat resistant ceramic glue with significant strength was used for preheated samples. All target components were roughly 3 mm diameter cylinders.

In the 2014 campaign, no targets were preheated, so all tantalum targets used the conformal configuration. The ablators were 220 μm long, attached to the 1 mm long samples by a glue layer. Tampers were 3 mm long.

In the 2015 campaign, targets were preheated and required the nonconformal configuration. The ablators were 250 μm long, attached to 1 mm long sample and a 3 mm long tamper.

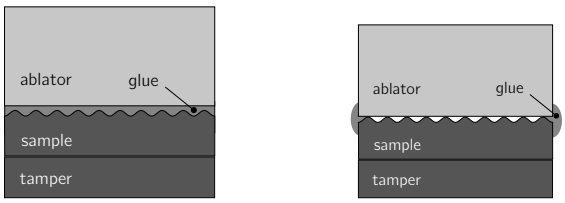

(a) (b)

Figure 3.2: Recovery target sketches in the conformal (a) and nonconformal (b) configurations.

The second style of targets, the *drive targets*, contained a thin 10-50 μm long sample. The goal of the drive target is to provide an opportunity for VISAR to probe the pressure in the sample near the ablator. The fate of the target after this measurement is made is unimportant, so the target does not need to be robust. In order for an accurate comparison to the recovery targets, the drive targets used the same ablator, glue, and sample material as the recovery target.

Two schemes to determine the state of the sample with VISAR were used. The particle velocity can be measured directly with VISAR. This concept leads to *flat drive targets* (Figure 3.3). VISAR can also measure the difference in shock breakout times from two different thickness of sample material. The shock speed is then the ratio of difference in distance traveled to difference in breakout time. This concept leads to *stepped drive targets*. Because VISAR measures the breakout velocities from each step, stepped drive targets also function as a pair of flat drive targets, giving a pair of breakout velocities.

If the loading wave is sufficiently strong, the reflection of the loading wave from the rear surface of the sample could fragment or melt the sample and cause loss of reflectivity and loss of VISAR signal. A thick tamper would solve this problem, but

the tamper material would have to be transparent to the VISAR probe laser. Lithium Fluoride (LiF) is used for this role. Due to the preheated sample, no window was used in the 2015 campaign.

Tantalum drive targets are sketched in Figure 3.3. It was simpler to manufacture the stepped drive targets with a step in the ablator and not in the window. This decision resulted in stepped targets that were more difficult to analyze, because the loading wave traveled through different thicknesses of ablator in each step. Because the steps were manufactured from different pieces of sample material, silver-doped paste was placed between the steps to prevent drive laser light from shining through gaps in the target and damaging the VISAR optics. The short step was 15 μm and the long step was 50 μm. To account for the difference, the ablator on the short step was 35 μm longer than the 220 μm long ablator on the long step.

Drive targets for copper samples are sketched in Figure 3.4. Heat resistant glue attached the ablator to the sample on the sides of the target only. Unlike in the tantalum targets, the stepped sample was made from a single piece. Following the recovery targets, the ablator was 250 μm long. The sample in the flat targets was 25 μm long. In the stepped targets, a region of the 50 μm long sample was plasma etched to 25 μm, making the short step. As in the recovery targets, all tantalum and copper drive targets were roughly 3 mm diameter cylindrical stacks.

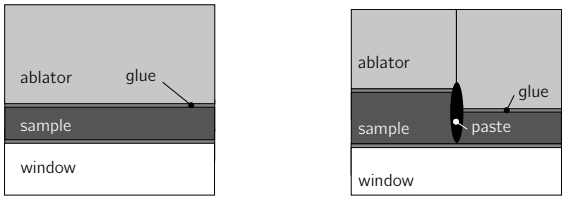

Figure 3.3: Flat (a) and stepped (b) drive targets used for tantalum samples in the 2014 campaign.

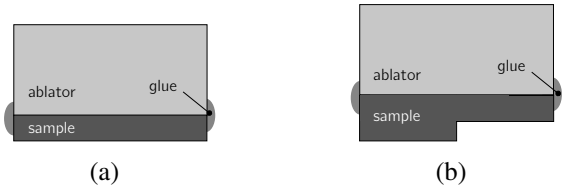

Figure 3.4: Flat (a) and stepped (b) drive targets used for copper samples in the 2015 campaign.

3.4 Manufacture of targets

The targets were manufactured by General Atomics [70]. For the 2014 campaign, the CH and LiF were purchased from Goodfellow. The maximum deviation from the specified 220 μm ablator length was 4 μm. The sample material was national stock polycrystalline tantalum at 4N purity with roughly 20 μm grains. For the 2015 campaign, CRF at 100 mg/cc was produced by General Atomics. On average, the produced CRF had a density closer to 115 mg/cc, with a maximum deviation from this average of 8 mg/cc. The largest deviation from specified ablator length of 250 μm was 6 μm. The sample copper came from polycrystalline stock at General Atomics at 4N purity.

Two perturbation patterns were used for the recovery targets, a 2D pattern of hills and valleys and a 3D egg crate pattern. The 2D perturbation is described by Equation 3.3 where $\lambda_{2D} = 50$ μm and $\eta_0 = 5$ μm. The 3D perturbation is described by Equation 3.4, where $\lambda_{3D} = 100$ μm.

$$\eta(x, y) = \eta_0 \cos\left(\frac{2\pi x}{\lambda_{2D}}\right) \tag{3.3}$$

$$\eta(x, y) = \eta_0 \cos\left(\frac{2\pi x}{\lambda_{3D}}\right) \cos\left(\frac{2\pi y}{\lambda_{3D}}\right) \tag{3.4}$$

Ideally, the perturbation patterns would use the same wavenumber, as discussed in Section 1.3. If $\lambda_{2D} = 50$ μm, then $\lambda_{3D} = 50\sqrt{2}$ μm for this condition to be satisfied. However, a mistake in the 3D target manufacture resulted in $\lambda_{3D} = 100$ μm. In this case, the 3D wavenumber was $k = \sqrt{k_x^2 + k_y^2} = 2\pi\sqrt{2}/100$ μm equivalent to a $50\sqrt{2}$ μm wavelength 2D perturbation. Consequently, the wavenumber of the 2D targets was larger than the wavenumber of the 3D targets, so the linear growth rate of the 2D targets was higher than the linear growth rate of the 3D targets. This issue prevented a direct comparison between the data collected from the 2D targets and the 3D targets.

The initial perturbation was machined into a steel die which was then nitrided to increases its hardness. Discs of the sample material were coined in a closed die [70]. The pattern machined into the die was transferred to the sample, Figure 3.5.

3.5 Capabilities of Jupiter Laser Facility

The Jupiter Laser Facility (JLF) at Lawrence Livermore National Laboratory (LLNL) is a user facility that is made available by LLNL to experimental groups. JLF offers

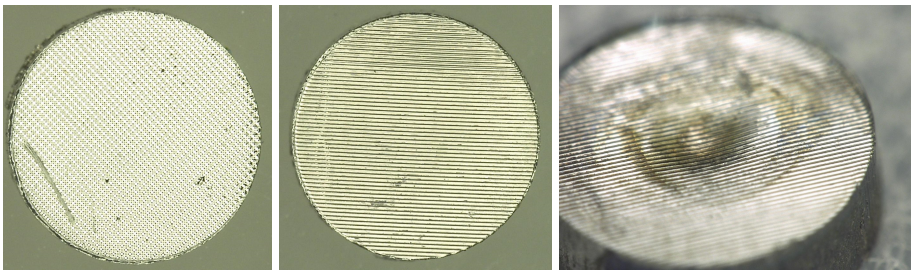

(a) (b) (c)

Figure 3.5: Image of a 3D sample (a), a 2D sample (b), and a 2D sample showing the thickness of the sample (c). This image was taken after the experiment, so the surface of the target is charred and cratered from the laser ablation drive.

two target areas: Janus and Titan. Janus is used for experiments requiring 1-2 long pulse beams. Titan is used for experiments requiring 1 short pulse beam and 1 long pulse beam. The beams are generated by a central bay and sent to each target area. Each beam requires an approximately 45 minute cool down after an amplified shot. If a beam is being shared between target areas, shots to a single target area occur on approximately 90 minute cycles. A single experimental campaign lasts four weeks, including a week of setup at the beginning of the campaign. The shot rate at this facility typically allows a best case scenario of 4 to 5 shots during a single day. The Janus target area was used for all experiments in this work.

Drive lasers

The Janus target area provides two lasers, referred to as the east beam and the west beam, each capable of delivering approximately 1 kJ of infrared 1053 nm light in 1-20 ns pulses. For experiments in this work, the frequency of each laser was doubled to green 527 nm light. The maximum energy of the converted light is roughly 200 J per beam. A small portion of each amplified drive beam is picked off before and after frequency conversion, providing a measurement of energy in the laser pulse. A continuous wave laser can be passed into the target chamber along the same beamline as the drive laser to help align the experiment.

Phase plates installed in the beamline smooth spatial variations in beam intensity and set the focused spot size of the beam. Two phase plates were used in this work. The first produces, ideally, a 1 mm by 1 mm square. The second ideally produces a 0.6 mm diameter circle. The size of the spot is difficult to quantify. The location of the target varied each shot due to normal variations in target dimensions, which required refocusing the drive beams and slightly changing the spot size. The spot

size of the amplified beam can also vary from the spot size of the alignment diode used to focus the beam and the spot size of the unamplified beam.

Decreasing the spot size increases the laser intensity for a given laser energy, boosting ablation pressure. However, decreasing the spot size means that the release waves from the edge of the ablated region will affect a greater area of the target.

Target chamber and preheating target mount

The drive lasers are delivered to the Janus target area inside a target chamber. The west beam and VISAR beam enter the target chamber along the same axis. The east beam enters the target chamber off the axis by 27° (Figure 3.6(a)).

The target mount was positioned at the target chamber center, where the three beams intersect. Final adjustments to the mount location were made with translation and rotation stages. Final laser pointing adjustments were made on each drive beam and on the VISAR beam by manipulating the final turning mirrors. An alignment camera in the chamber helped position the drive lasers on the target.

Turbo pumps maintained a vacuum of $\sim$ 1 mTorr during a shot. The VISAR optics were protected from target debris during the shot by a replaceable blast shield. Just before a shot, the alignment camera was protected with an opaque cover to block drive laser light.

In the 2014 campaign, both east and west beams were used and the target mount was aligned so that the axis of the target was between the east and the west beams. In the 2015 campaign, preheated shots required a more complex mount (Figure 3.6(b)). Cooling was added to shorten turnaround time for the next shot, as the target chamber could not be vented until the mount was below 200° C. Only the east beam was used.

The preheating target mount body was constructed out of 316 stainless steel. Copper washers held the target in contact with the body of the mount and the 308 stainless steel cooling loop. Ceramic standoffs insulated the mount from the target chamber. Thermocouples (Omega K type, 0.005" thick) were attached in two locations. First, a thermocouple was held in contact with one of the cartridge heaters (Omega CIR-10151/120, 250 W), the "heater TC" in Figure 3.6(b). A second thermocouple was attached between the mount and the target, labeled the "target TC" in Figure 3.6(b). The thermocouple could not be attached directly to the target without interfering with the drive laser, so the temperature at the target was calibrated to the temperature measured by these thermocouples in separate experiments.

The cartridge heaters were controlled by manually increasing the voltage of a variable AC controller over approximately 10 minutes. The heater life was extended by waiting until pressure was below 0.2 Torr before applying voltage to the heaters and limiting the maximum voltage to 70 V. Even with restricting high temperatures to high vacuum conditions, oxidation was noticeable and the screws holding the target in the mount were replaced each shot to prevent them from binding to the mount.

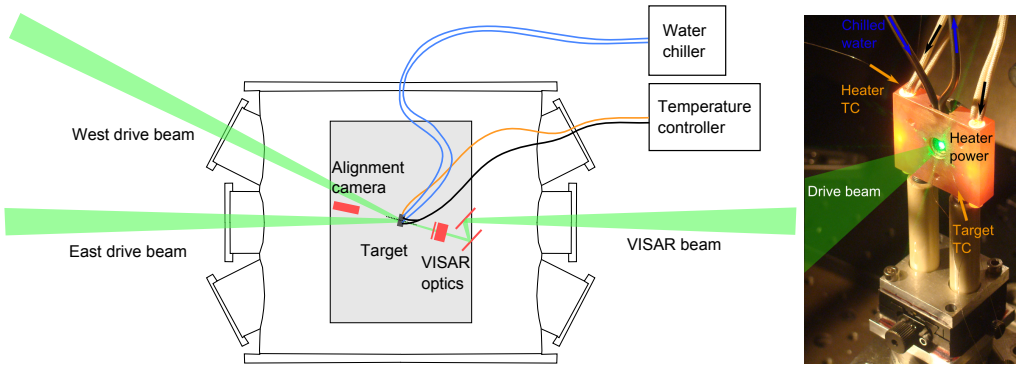

(a) (b)

Figure 3.6: Overhead view of the Janus target chamber (a). The target mount and other equipment are attached to the breadboard. The west beam is shown from 2014 campaign setup. Temperature controller and water chiller for the target heating mount are shown from the 2015 campaign. The temperature controller requires heater thermocouple (TC) hookup and heater power connections (b).

VISAR system

VISAR (velocity interferometer for any reflector) is an optical velocimetry diagnostic [3] based on the wide angle Michelson interferometer (WAMI), a modification of the Michelson interferometer. An etalon, a glass component with anti-reflective coating, is added to one of the legs of the interferometer. The etalon shifts the effective location of the mirror in its leg, improving the uniformity of the fringes produced by the interferometer and improving tolerance to imperfections in the reflectivity of the target [23, 34].

Light from a probe laser is reflected off the target and then passed to the interferometer, sketched in Figure 3.7. While the virtual mirror position created by the etalon is the same as the mirror position in the other leg, the physical path length is longer. Combined with the decrease in the speed of light introduced by the etalon, this layout creates a delay between the legs. If the Doppler shifted input is time varying, the delayed light frequency is different than the current input and the interferometer

will see a beat frequency.

The time delay τ imparted by the etalon is

$$\tau = \frac{2L}{c}\left(n_0 - \frac{1}{n_0}\right), \tag{3.5}$$

where L is the etalon length, n_0 is the index of refraction of the etalon, and c is the speed of light. The properties of the VISAR determine the relationship between the measured fringe shift and the velocity of the sample, the velocity per fringe (VPF). On the Janus VISAR [14], the etalons have $n_0 = 1.4607$. Lengths of etalons used in the experiments are given in Table 3.1.

Two modifications must be made to calculate the VPF. First, the wave speed in the etalon is affect by dispersion. Different frequencies of light passing through the etalon, caused by the Doppler shifting of the probe laser, are delayed different amounts by the etalon. Second, if a window is used, the index of refraction of the window material alters the optical path of the probe laser requiring a correction.

Because the window correction depends on the individual target used and not the VISAR system, two VPF values will be defined. First, the baseline VPF not including the window correction and VPF*, including the window correction,

$$\mathrm{VPF} = \frac{\lambda_0}{2\tau(1+\delta)} \tag{3.6}$$

$$\mathrm{VPF}^\star = \frac{\lambda_0}{2\tau(1+\delta)a} \tag{3.7}$$

$$\delta = -\frac{n_0}{n_0^2 - 1}\lambda_0 \left.\frac{dn}{d\lambda}\right|_{\lambda=\lambda_0} \tag{3.8}$$

$$n_w = a + b\rho, \tag{3.9}$$

where λ_0 is the wavelength of the VISAR laser (532 nm at JLF) and $\mathrm{d}n/\mathrm{d}\lambda$ is the dispersion of the etalon, resulting in $\delta = 0.0318$. The factor a is a coefficient of a model for the linear variation of n_w, the index of refraction of the window material in terms of its density ρ [23]. For the LiF windows used in the experiment, $a = 1.28$.

The classic VISAR system focuses the central spot of the image plane on a detector, producing a single fringe measurement. The JLF VISAR system is an alternate

design called ORVIS (optically recording velocity interferometer system) [8], where the interfering beams are displaced by a small angle producing a pattern of fringes, shown in the inset of Figure 3.7. ORVIS is also known as line-VISAR, as it views a line across the back of the sample. When the sample moves, each point of the fringe pattern undergoes a fringe shift. This shift appears as a translation of the pattern perpendicular to the fringes. A full fringe shift moves the fringes one fringe width. Because spatial as well as temporal information is captured by a line-VISAR, it can be used to measure different breakout velocities from different steps in a stepped drive target.

The fringe pattern is imaged on a streak camera producing an image like the one in the inset of Figure 3.7. The streak cameras were both found to be linear in time. The VISAR 1 streak length was 46 ns and the VISAR 2 streak length was 51 ns. Reference images were taken before the shot to account for any streak tilt. The streak images were analyzed to produce velocity traces [84, 14].

Shock loading presents a problem for VISAR. If the velocity imparted by the shock exceeds the VPF of the VISAR, then at least a full fringe cycle will occur at the shock breakout. The number of fringe cycles is lost and the measured velocity will be off by some integer multiple of the VPF. To resolve the fringe ambiguity, two VISAR with different etalons are used in parallel.

At each fringe jump, a range of possible velocity traces can be constructed by adding or subtracting integer multiples of the VPF. However, the VISAR should agree with each other. For good choices of etalons, only one of the possible reasonable velocity traces will match both VISAR. Typically, etalons are chosen with a 2.5:1 length ratio [14]. Generally, the ratio of VPF for each VISAR should not be close to an integer.

Table 3.1: Description of etalons used in experiments. For the 2014 campaign a LiF window was used for all shots. For 2015, only one shot used a LiF window while all others had no window.

Etalon length (mm)	VPF (km/s/fringe)	Campaign
40.41127	1.27	2014 VISAR 1
100.21	0.497	2014 VISAR 2
28.77136	1.73	2015 VISAR 1
11.63844	4.28	2015 VISAR 2
50.40292	0.99	2015 VISAR 2

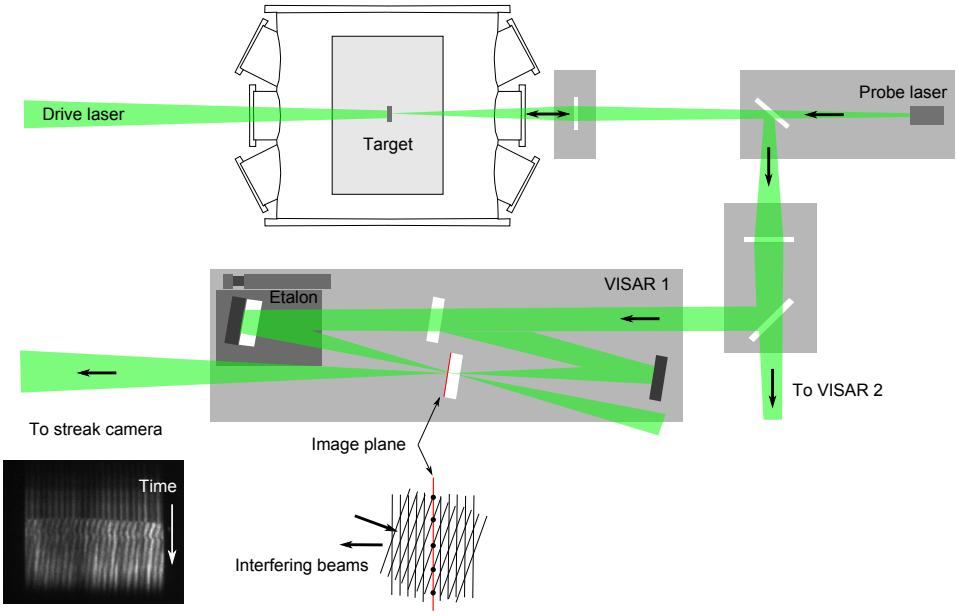

Figure 3.7: Sketch of the JLF VISAR system. Only the VISAR 1 interferometer is shown. The VISAR 2 system is identical to the VISAR 1 system. The optics between the probe laser and the interferometer are only illustrative and do not match the actual JLF VISAR optics. Image adapted from [14].

3.6 Profiling the recovered samples

During manufacture, each sample was marked with a fiducial to help align the pre-shot and post-shot profiles. The fiducial is visible at the upper left of the profiles in Figure 3.8. The perturbations were profiled using a white light interferometer (Wyko NT9100) with a vertical resolution of < 0.1 nm.

After the experiment, the target was cleaned to remove ablator and glue residue. Methods of removing debris included acetone soak, nitromethane soak, heated nitromethane soak, sonication, and rubbing with a cotton swab. SEM images of the cleaned target showed fragile structures and no indication of damage, indicating cleaning did not affect the target profile.

To record the post-shot profile, the sample was aligned with the fiducial in roughly the same location as in the pre-shot profile. Alignment was adjusted so that the wave peaks were as vertical as possible. The profile covered a 3 mm diameter circle, centered 1.5 mm to the right of the leftmost edge of the coined area. Figures 3.8(a) and 3.8(b) are an example of the alignment between the pre-shot and the post-shot target.

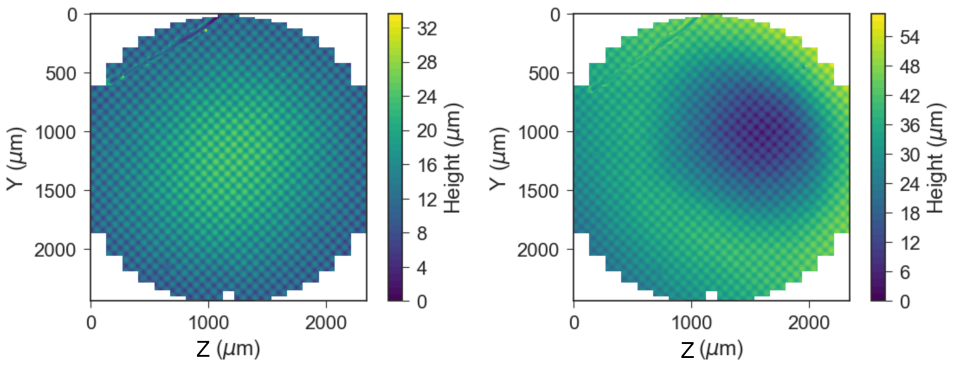

(a) (b)

Figure 3.8: Example profiles of a 3D tantalum sample pre-shot (a) and post-shot (b).

3.7 Profile analysis

After the targets were manufactured, profiled, driven, cleaned, and profiled again post-shot, the profiles were analyzed to calculate the growth of the interface perturbation. First, the center of the post-shot target was found. The laser drive formed a pronounced crater in the tantalum samples. The center was found automatically by selecting the deepest location in the crater. The CRF drive did not form such a pronounced crater in the copper samples, so the shot center was selected by eye.

Only a subset of each sample profile was analyzed. A reduced data set in a square region 500 μm wide around the shot center was defined. The empty pixels in the data set were filled in by linear interpolation. The interpolated data was filtered with a Gaussian filter to remove small surface features. The standard deviation of the Gaussian filter was set to 2 μm, Figure 3.9. The contribution of the surface features to the profile height was around 2 μm, a significant portion of the perturbation amplitude.

The extrema were found using minimum and maximum filters. For 3D targets, the filter neighborhood was set to $\lambda/2$. For 2D targets, the profile was divided into $\lambda/3$ wide strips that run across the ripples. Within those strips, a filter with a neighborhood of λ was applied. The extrema that were within $\lambda/3$ of the edge of the profile were discarded to prevent counting extrema from waves that were not wholly contained in the domain.

After the extrema were found, the neighbors of each extrema were identified. For a maxima, the neighbors are minima. For a minima, the neighbors are maxima. In a

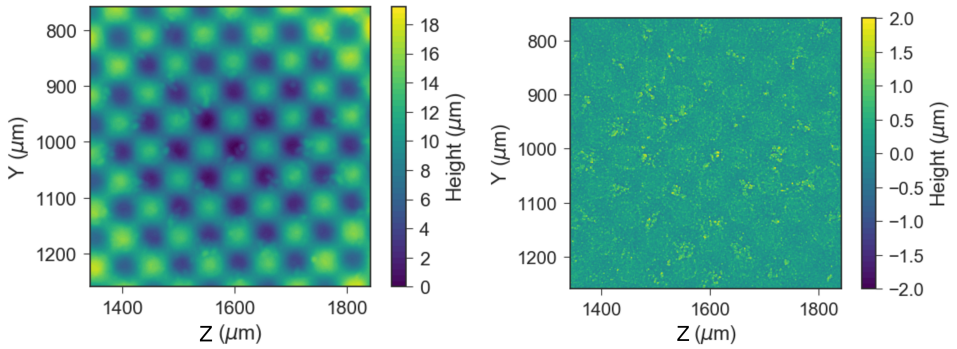

(a) (b)

Figure 3.9: Profile filtering for tantalum 3D sample. The target profile is filtered with a 2 μm Gaussian filter (a). The difference between the filtered and the unfiltered data shows the amplitude of the surface features (b).

3D target, the nearest four neighbors were identified. For a 2D target, the nearest two neighbors within the same strip were identified. Let the function $N(i) = (\Delta x_1, \cdots)$ return the set of heights between the i^{th} extrema and each of its neighbors (Figure 3.10). Noticeably, the extrema on the 2D targets did not fall on a line; the freedom allowed by the strips resulted in small deviations along the ripple.

It is expected that there is some low frequency content in the profile and $x(y_i, z_i) \neq x(y_i \pm \lambda, z_i \pm \lambda)$. In the pre-shot targets, long wavelength deformation of the die added a bulge to the center of the target. In the post-shot targets, the crater at the shot center dominated the profile. Consequently, $\Delta x_1 \neq \Delta x_2 \neq \cdots$. Letting $\mu()$ be the mean of a set and $\sigma()$ be the standard deviation of a set, the peak to valley amplitude (PTV) was defined as $\text{PTV}(i) = \mu(N(i))$. The value of $\sigma(N(i))$ was calculated as a diagnostic, but each $\text{PTV}(i)$ was taken as a single value with no uncertainty.

The average of each $\text{PTV}(i)$ over the shot area was determined by cumulatively averaging from the shot center. Let (y_c, z_c) be the location of the center. Then, instead of referencing the i^{th} extrema at location (y_i, z_i), it is useful to reference the radial distance of the extrema from the shot center $r(i) = \sqrt{(y_i - y_c)^2 + (z_i - z_c)^2}$. Let $C(R)$ return the set of $\text{PTV}(i)$ where $r(i) \leq R$. Then, the cumulative PTV is $\overline{\text{PTV}}(R) = \mu(C(R))$ with uncertainty $U_{\text{PTV}}(R) = \pm\sigma(C(R))$.

This procedure, from data reduction to the extrema neighbor finding and the statistics was repeated for the pre-shot profiles. The center of the post-shot target was used as the center of the pre-shot target.

At a given radius, the collection of cumulative post-shot PTV values that exist at a

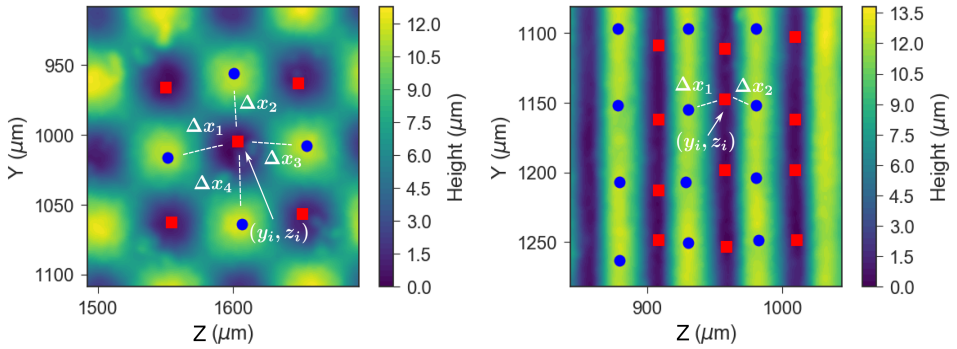

Figure 3.10: Extrema for a post-shot 3D sample (a) and for a post-shot 2D sample (b). Blue dots locate maxima and red dots locate minima. The difference in height between neighboring extrema is given by Δx. Here, the function $N(i)$ returns the set of Δx in the image.

smaller radius were compared to the collection of cumulative pre-shot PTV values at a smaller radius. The superscripts `pre` and `post` are used to distinguish the two data sets. The growth factor GF(R) was defined as

$$\mathrm{GF}(R) = \frac{\overline{\mathrm{PTV}}^{\mathrm{post}}(R)}{\overline{\mathrm{PTV}}^{\mathrm{pre}}(R)}. \tag{3.10}$$

The uncertainty of the growth factor was defined as

$$U_{\mathrm{GF}}(R) = \pm\sqrt{\left(\frac{\partial \mathrm{GF}}{\partial \overline{\mathrm{PTV}}^{\mathrm{post}}}\bigg|_R U^{\mathrm{post}}_{\mathrm{PTV}}(R)\right)^2 + \left(\frac{\partial \mathrm{GF}}{\partial \overline{\mathrm{PTV}}^{\mathrm{pre}}}\bigg|_R U^{\mathrm{pre}}_{\mathrm{PTV}}(R)\right)^2} \tag{3.11}$$

$$= \pm\sqrt{\left(\frac{1}{\overline{\mathrm{PTV}}^{\mathrm{pre}}(R)} U^{\mathrm{post}}_{\mathrm{PTV}}(R)\right)^2 + \left(-\frac{\overline{\mathrm{PTV}}^{\mathrm{post}}(R)}{\overline{\mathrm{PTV}}^{\mathrm{pre}}(R)^2} U^{\mathrm{pre}}_{\mathrm{PTV}}(R)\right)^2}. \tag{3.12}$$

Figure 3.11 highlights the calculation of GF(R) for a 3D target. The PTV of the 3D pre-shot target was consistently around 9 μm. In the shocked target, the average PTV hovered around 11 μm. Scatter in the average as a function of R increased the cumulative uncertainty as R increased. The final GF(R) measurement shows the influence of the variation in radial statistics from the post-shot target. The GF(R) decreased and $U_{\mathrm{GF}}(r_i)$ increased as R increased.

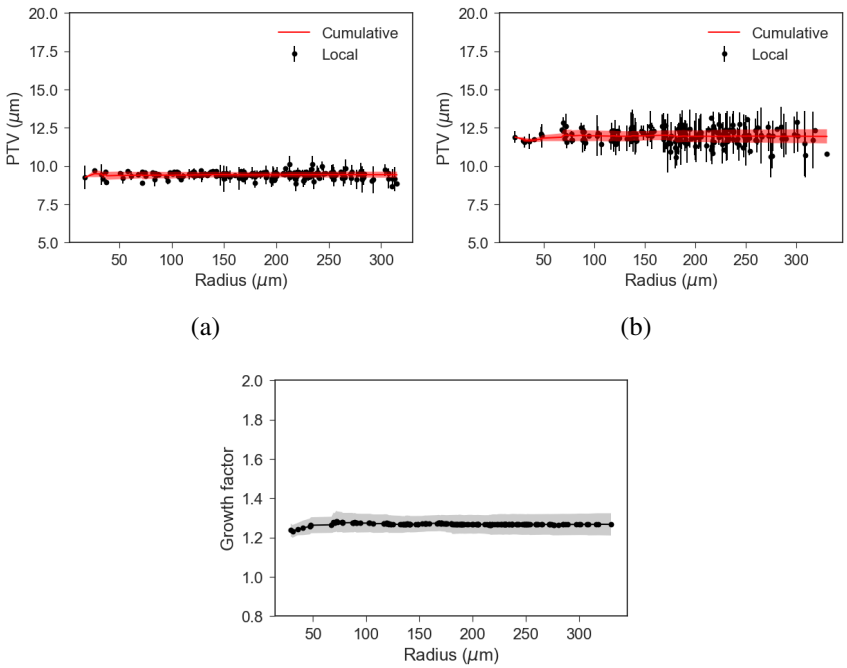

Figure 3.11: Cumulative PTV as a function of radius from the shot center for the pre-shot target (a), the post-shot target (b), and the growth factor as a function of radius (c). Local uncertainty is $\sigma(N(i))$, plotted at the radius $r(i)$. Cumulative uncertainty is $U_{\mathrm{GF}}(R)$.

A single value of R, defined R_c, was selected to compare GF(R) across all targets. This value of R_c should be smaller than the radius of the laser spot to reduce the edge effects in the profile data.

Chapter 4

NUMERICAL METHODS

Understanding the loading generated by laser ablation required fitting a model of laser ablation to experimental results. This chapter describes the calibration of the loading model. The model loading was then used to simulate instability growth using existing strength models to evaluate their predictions at the loaded state.

4.1 Background on laser ablation

Laser ablation of the target generates the loading wave which accesses high pressures and strain rates in the sample material and drives the instability at the ablator-sample interface. The scaling of the loading with laser energy was studied with simulations using Hyades, a 1D Lagrangian code developed by Cascade Applied Sciences [45]. Hyades includes EOS and strength models for all the target materials used in this work. The Sesame EOS was used for tantalum, copper, carbon, polystyrene, and LiF. The Steinberg-Guinan strength model was used for tantalum and copper. Hyades does not contain a porosity model to simulate the low initial density of the CRF. The best available solution was to use an EOS for nonporous carbon, but with the initial density set to the density of the CRF [44].

Two studies of Hyades simulations were used in this work. First, a study of Hyades simulations predicted scaling of the loading condition with laser energy. The predicted peak pressure in the sample informed laser energies used in the experiment. The predicted shock arrival time informed time delays used in the experiment to guarantee VISAR measured the shock breakout. The predicted breakout velocity informed the analysis of the VISAR signals by putting bounds on possible breakout velocities.

Second, a study of Hyades simulations described how energy was deposited on the target during laser ablation. Hyades is only 1D and cannot simulate inherently 2D or 3D hydrodynamic instabilities. The code selected for hydrodynamic instability simulations, CTH (introduced in Section 4.6), cannot model laser ablation. Instead, CTH allows the user to define an energy source over some space and time. The Hyades ablation study informed the definition of energy sources in the CTH simulations that mimicked laser ablation loading, discussed in Section 4.8.

All Hyades simulation used the same laser source: a 3 ns square pulse, with 0.1 ns rise and fall times, of 527 nm wavelength light distributed over a 1 mm^2 spot area. The energy contained in the pulse is often used to refer to a given laser ablation drive, but it is the intensity of the light that is important in simulating laser ablation. This spot size and pulse length is typical for all experiments. Typical values of energy were between 10 and 100 J.

Experimental laser sources were subject to uncertainty. The spot size of the laser, the pulse shape, and the energy of the pulse were not known exactly. However, following established procedures increased the repeatability of the experiment. Consequently, the Hyades simulations were unable to predict a single experimental result, but simulation and experiment scaled with laser energy similarly.

The uncertainty present in linking Hyades simulations to experimental results was lumped into a single *Hyades factor*, $F = E_H/E_s$, where E_s was the energy measured during a laser shot (shot energy) and E_H was the energy required to match the experimentally measured shock in a Hyades simulation, the Hyades energy.

4.2 Study of laser energy scaling in recovery targets

The recovery target geometry was reduced into a 1D domain. The glue layer was neglected, so there was no gap between the ablator and the sample. The mesh in the sample was extended to be sufficiently long that loading wave did not reach the end of the domain and produce unwanted reflections. The recovery target mesh is described in more detail in Appendix A.2.

Appendix A.1 contains a detailed description of the mesh requirements. Succinctly, the mesh resolution must be highest near the surface illuminated by the laser. An expanding, or feathered, mesh was used to decrease the mesh resolution farther from the ablation. Distances between the mesh points, the zone widths, increased from 1 Å up to roughly 1.0 μm. Each zone was $< 5\%$ larger than the previous zone. After the zones were sufficiently expanded, much of the remained of the target was meshed with constant width zones.

The *bulk pressure*, the pressure averaged between points 1 μm and 10 μm into the sample, was calculated for CH-tantalum and CRF-copper recovery targets, Figure 4.1. The *ripple pressure*, defined as the maximum bulk pressure, is a simple way to refer to loading conditions by the maximum pressure it produces near the interface perturbation. Mesh convergence studies comparing the ripple pressure predicted by different mesh resolutions (Appendix A.4) found that mesh resolutions finer than

1.0 μm/zone were sufficient.

Despite identical square pulse shapes, the different ablator materials produced different loading waves. The tantalum samples experienced a shock, followed by a release to an intermediate plateau, followed by a release to a long low pressure plateau before releasing to zero pressure. The copper samples experienced a shock followed by a steady release to zero pressure with no intermediate plateaus.

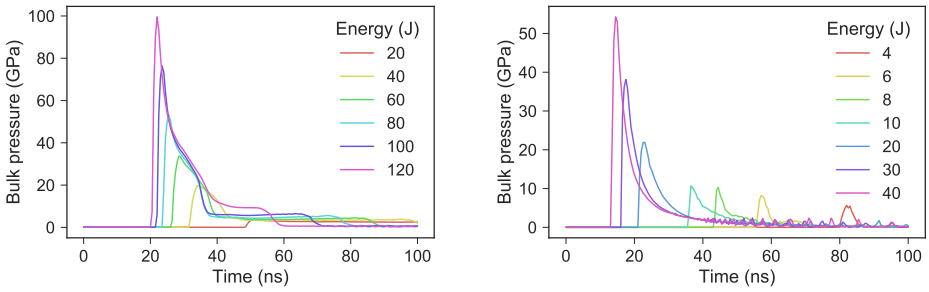

(a) (b)

Figure 4.1: Bulk pressure in a tantalum sample (a) and in a copper sample (b) for a range of laser energies.

4.3 Study of laser energy scaling in drive targets

The drive target geometry was reduced into a 1D domain. The mesh in the window was extended so that the loading wave did not reflect from the end of the mesh during the simulation. The mesh is described in more detail in Appendix A.3. For a given laser energy, the bulk and ripple pressures were calculated. The peak velocity was recorded at the sample-window interface, the location where the VISAR measurement was made during drive shots.

Power law fits to the simulation results simplified analyzing the drive shot data. For each drive target design, the breakout velocity as a function of Hyades energy was determined, $v_b = f_{v_b}(E_H)$. The ripple pressure was fit to breakout velocity, $P_r = f_{P_r}(v_b)$. These two fits allowed the ripple pressure in a recovery target to be calculated from the laser energy.

The targets for the 2014 campaign used a polystyrene ablator, tantalum sample, and LiF window. Hyades was used to simulate laser ablation with laser energies between 20 J and 200 J (Figure 4.2). The targets for the 2015 campaign used a CRF ablator and copper sample with no window. The Hyades energy required to produce this

range of simulations was significantly lower than the energy used for the tantalum targets with CH ablators (Figure 4.3).

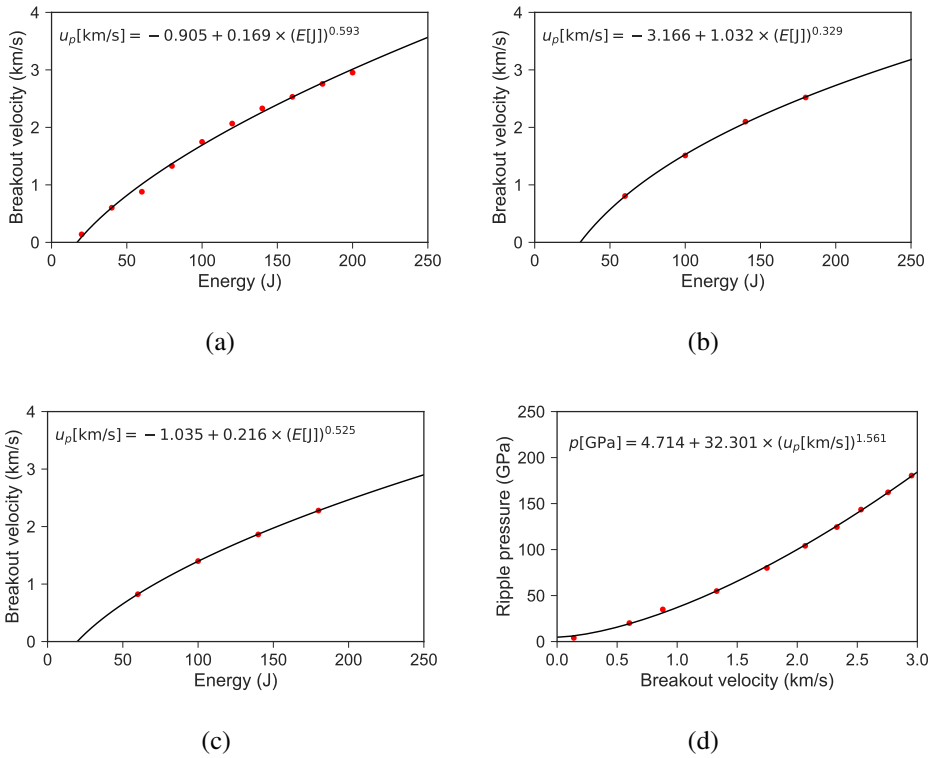

Figure 4.2: Results from Hyades with power law fits of breakout velocity for the flat tantalum drive targets (a), the 15 μm step of the step drive targets, (b), and the 50 μm step of the step drive targets, (c). The ripple pressure as a function of breakout velocity for the recovery targets is shown in (d).

4.4 Study of energy deposition during laser ablation

The energy deposition of the laser on a CH ablator was studied for 50 J, 80 J, and 110 J laser pulses with 0.5 μm/pt resolution. The laser ablation only deposited energy in the first 1 μm of the ablator surface (Figure 4.4(a)). This plot uses the Lagrangian coordinate of the mesh points. As time progressed, the leftmost material rushed away from the face of the ablator, traveling over 1 mm before the laser turned off. This ablation plume absorbed some of the incident light, but the majority of the laser power was absorbed closer to the ablator surface.

The targets for the 2015 campaign used a CRF ablator. The energy deposition of the laser on the ablator was studied for 6 J, 10 J, and 15 J laser pulses with 0.25 μm/zone resolution. The laser light deposited energy farther into the CRF ablator

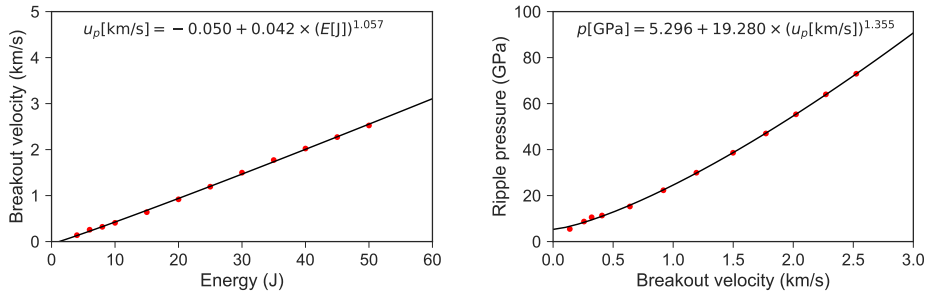

(a) (b)

Figure 4.3: Results from Hyades with power law fits of breakout velocity for the flat copper drive targets (a). The ripple pressure as a function of breakout velocity for the recovery targets is shown in (b).

than the CH ablator. However, all energy deposition was constrained to the first 5 μm.

This study supported a simplified model of a laser ablation drive, where the laser energy was deposited in the first 1 μm of the ablator material at the initial time. This approximation was necessary to simply initiate 2D and 3D CTH simulations of the hydrodynamic instability.

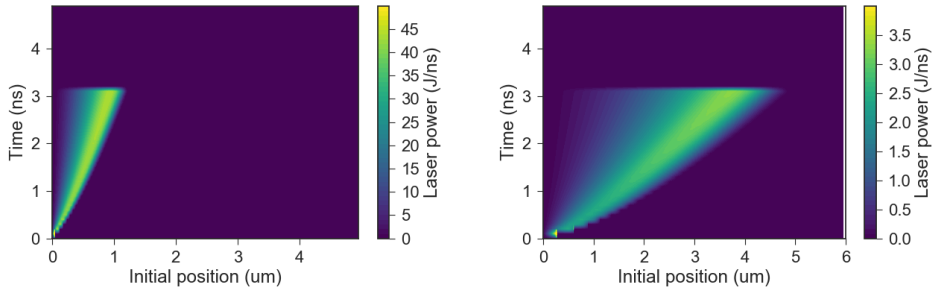

(a) (b)

Figure 4.4: Laser power per zone for (a) a 110 J laser pulse ablating CH and for (b) a 15 J laser pulse ablating CRF. The laser strikes the ablator at coordinate 0 μm.

4.5 VISAR processing summary

Each drive shot produced two streak images, from VISAR 1 and VISAR 2. The fringes before the shock arrival were constant. When the shock arrived, the fringes jumped and then moved proportionally to the changing velocity as the sample released. In Figure 4.5, the VISAR 2 etalon had a higher velocity sensitivity,

resulting in a more obvious release following the shock. The triggering system flashed a fiducial in each streak image to help align the images in time. The fiducial is on the right hand side of the images and is highlighted by a white dotted line.

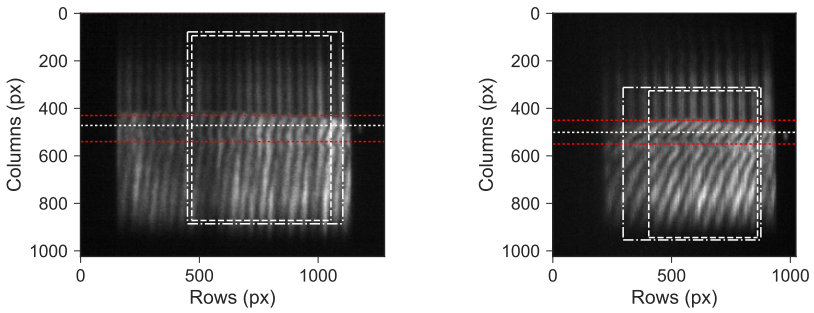

Figure 4.5: Annotated images from VISAR 1 (a) and VISAR 2 (b). The white dotted line is the fiducial location. The red line is the location of the fringe jumps. The larger box is the phase unwrapping region in XVIS and the smaller box is the region where the velocity trace is calculated.

The LLNL tool XVIS was used to calculate velocity traces from the streak images. A region of the image was selected for phase unwrapping. Out of the unwrapped region, a smaller region was selected to calculate the velocity trace and uncertainty bounds. The camera streak rate was nearly linear, so the time was calculated from the streak image by a fit between the 1024 time pixels and the time elapsed during the streak, 46 ns for VISAR 1 and 51 ns for VISAR 2. The fringe shifts were converted to velocity traces using the VPF. The time was shifted so that the beginning of the fiducial occurs at $t = 0$ for each VISAR result. The peak velocity, including uncertainty from each VISAR, was bounded and compared (Figure 4.6). In each case, only one pair of fringe jumps was feasible to match the two VISAR traces. The peak velocities were averaged to give a combined VISAR measurement and uncertainty. This analysis procedure was repeated for each drive targets.

Determining ripple pressure in recovery targets as a function of the shot energy required calibrating the fits determined in Section 4.3. For each drive target design, the breakout velocity as a function of Hyades energy was determined, $v_b = f_{v_b}(E_H)$. The ripple pressure was fit to breakout velocity, $P_r = f_{P_r}(v_b)$. These two fits allowed the ripple pressure in a recovery target to be calculated from the laser energy. However, the laser energy used in Hyades simulations differed from the shot energy by the Hyades factor, $F = E_H/E_s$. In order to compare the fits to experimental data, E_H was converted to E_S, so $v_b = f_{v_b}(E_s \times F)$ and $P_r = f_{P_r}\left(f_{v_b}\left(E_s \times F\right)\right)$.

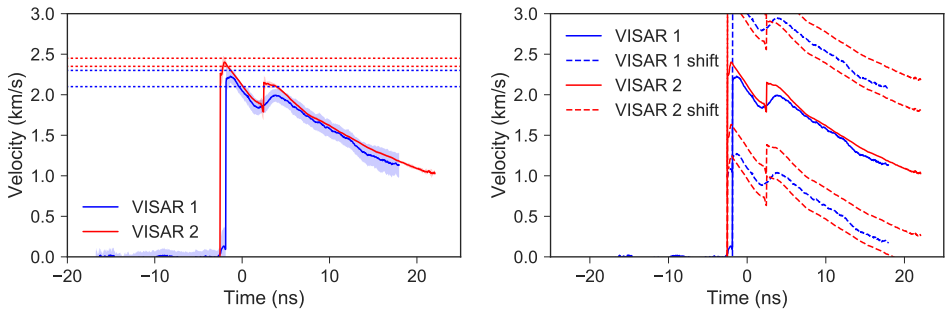

(a) (b)

Figure 4.6: Velocity traces from XVIS (a). The solid lines are the velocity traces and the shaded region surrounding the traces are the uncertainty bounds output by XVIS. The horizontal dashed lines are the upper and lower bounds of the peak breakout velocity. The traces with different possible fringe jumps only match for one reasonable post shock velocity (b).

Breakout velocities from each drive shot were plotted as a function shot energy and compared against the fits calculated from Hyades simulations. The Hyades factor was changed until the fit overlapped the drive shot data. Uncertainty bounds were chosen to contain all experimental values. Once the Hyades factor was determined, the recovery target ripple pressures was determined from the shot energy.

Polystyrene-tantalum drive target calibration

A summary of all drive shots is given in Table 4.1. The VISAR results were treated separately, so each stepped drive target produced two measured breakout velocities.

Breakout velocities from each drive shot were plotted as a function shot energy (Figure 4.7). As each side of the step targets differ from the flat target, each of the three sets of drive data were fit independently. The 50 μm step used the same ablator as the flat drive target, but used a thicker sample. The 15 μm step ablator was longer at 250 μm.

The 0.39 Hyades factor required to fit the flat simulations was closer to the 0.33 Hyades factor required to fit the 50 μm stepped target simulations than the 0.29 required to fit the 15 μm stepped target simulations. The lower factor indicates that for a given laser drive, the Hyades simulations overpredicts the breakout velocity. It is possible the greater difference in the 15 μm step targets was due to the longer ablator. If Hyades underpredicted attenuation in the ablator, the shock reaching the ablator-sample interface in the experiment was weaker than in the simulations, resulting in a slower breakout velocity. If this is the correct interpretation, then the

difference in Hyades factor between the flat targets and the 50 μm targets was likely due to a similar underprediction of attenuation in the tantalum sample.

As the drive calibration appeared to be very sensitive to ablator length and somewhat sensitive to sample length, only the flat targets were used in the calibration. The flat targets matched the ablator length used in the recovery targets, and the thinner sample reduced errors introduced by attenuation. Along with the Hyades factor for flat drive targets, the fit of ripple pressure to breakout velocity was used with the fit of breakout velocity to drive energy to determine the bulk pressure for a given drive energy.

One drive shot used the smaller circular phase plate. Because the area of the spot size for either phase plate was not precisely known, this drive shot could not be included in the calibration. However, the assumed spot area was verified. The energy of the shot was converted to an energy equivalent to the larger spot size by multiplying by the ratio of spot size areas. A ratio of 2.65 placed the drive shot in the center of the existing calibration. If the square phase plate spot size area was 1 mm^2, the small phase plate produced a circle with diameter of 690 μm, close to the expected 600 μm. Bulk pressures in recovery targets using the circular phase plate were calculated by first multiplying the energy by 2.65 and then applying the calibrated fit from Hyades.

A constant uncertainty of ±150 m/s was sufficient to contain the uncertainty on all of the drive shot results except for F1. As F2 was driven with nearly the same energy (139 J compared to 132 J) the uncertainty of F1 was taken to be a better indicator of the uncertainty in this range.

Table 4.1: Summary of polystyrene-tantalum drive targets. The target name and abbreviation are used to refer to the shot in the text.

Name	ID	Target type	Phase plate	Shot energy (J)
Flat 1 (F1)	070314 s1	Flat	Square	132
Flat 2 (F2)	070314 s2	Flat	Square	139
Stepped 1 (S1)	071414 s4	Stepped	Square	313
Flat 3 (F3)	070714 s1	Flat	Square	361
Stepped 2 (S2)	071514 s4	Stepped	Square	408
Circle 1 (C1)	071714 s3	Flat	Circle	119

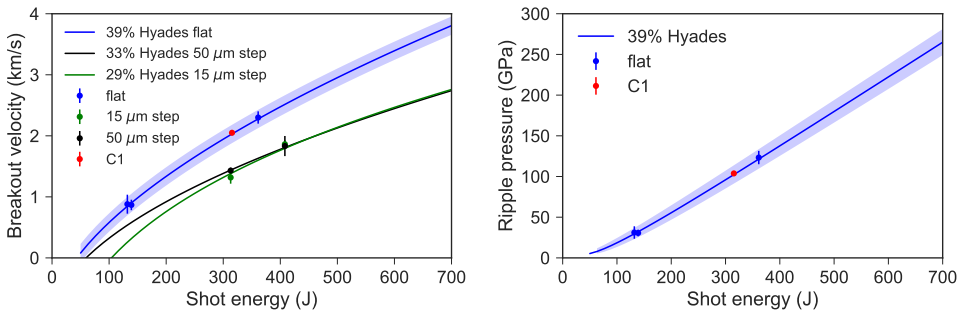

(a) (b)

Figure 4.7: Plot of breakout velocities from drive targets along with best fit of the Hyades results (a) and the resulting ripple pressure determined from the flat drive targets (b). Uncertainty bounds do not contain F1, but do contain the more certain F2, driven with nearly the same energy.

CRF-copper drive target calibration

The CRF-copper drive shots were more difficult than the CH-tantalum drive shots. JLF does not commonly delivery drive laser pulses in the low energy range used to drive recovery targets with a CRF ablator. With a CH ablator, differences between the requested and delivered energy did not significantly affect the transit time of the shock through the target, meaning the approximately 50 ns streak camera window was more than long enough to account for uncertainty in timing. However, the transit time of the shock in the CRF was much more sensitive to variations in shot energy. Differences between requested and delivered energy meant that missing the shock breakout on a low energy shot was possible.

Without a window, the shock breakout from the sample could result in a loss of reflectivity at shock breakout. Higher energy drive shots resulted in loss of signal immediately after the shock breakout (Figure 4.8). Lower energy drive shots fared better, but resulted in failures to capture shock breakout due to sensitivity of transit time to drive laser energy. In order to overcome this difficulty, a LiF window was attached to a flat drive target for shot L1.

These difficulties meant that out of the four breakouts summarized in Table 4.2, only S1 and L1 produced usable VISAR data. Two additional drive shots failed to capture any breakout. Because of the window added to L1, S1 and L1 required independent Hyades simulations and independent Hyades factors.

The step target data contained only a single breakout, meaning the field of view of the VISAR did not contain the step. Based on the transit time of the shock, the

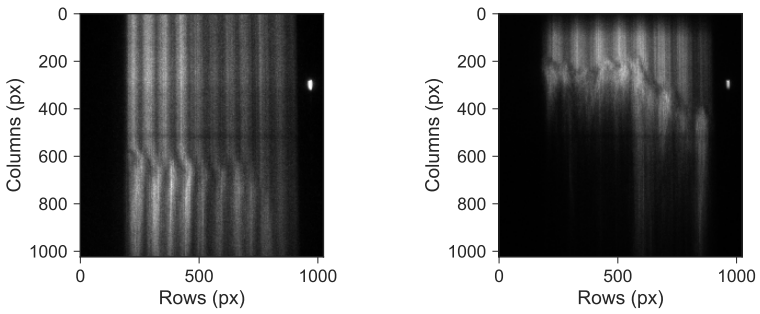

(a) (b)

Figure 4.8: Streak images from VISAR 2 of shot S1 at 18 J (a), an example of a usable VISAR image, and of shot F2 at 53 J (b), an example of a VISAR image rendered unusable by loss of fringes at shock breakout.

breakout was from the thinner 25 μm step.

The calibrations for S1 and L1 are shown in Figure 4.9. Shot L1 was better fit by 74% scaling instead of the 65% scaling that worked best for S1. As the ablator length and sample thickness was the same, any difference in scaling was due to the model for LiF in Hyades. In order to include the uncertainty from this difference the 74% scaling was taken, but the uncertainty was expanded to ±200 m/s in order to include the result from shot S1.

One heated drive shot was attempted, but no breakout was captured. It is possible that the thermal expansion of the target caused delamination of the ablator and sample.

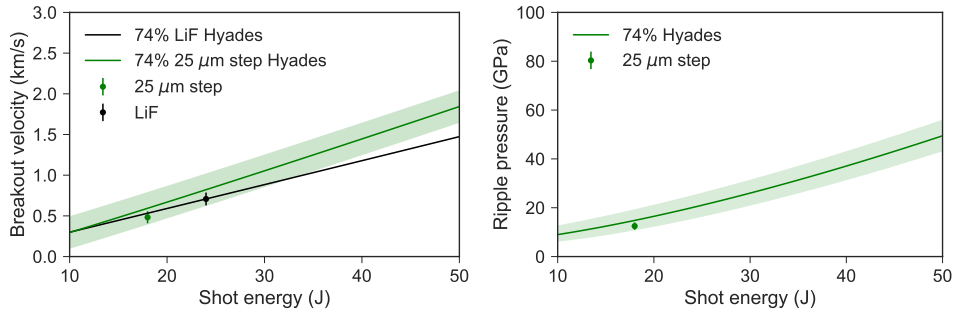

(a) (b)

Figure 4.9: Plot of breakout velocities from drive targets along with best fit of the Hyades results (a) and the resulting ripple pressure determined from the flat drive targets (b).

Table 4.2: Summary of CRF-copper drive targets. The target name and abbreviation will be used to refer to the shot in the text. F1 and F2, while producing a breakout, could not be interpreted.

Name	ID	Target type	Phase plate	Shot energy (J)
Flat 1 (F1)	150803 s2	Flat	Square	53
Flat 2 (F2)	150804 s3	Flat	Square	33
Stepped 1 (S1)	150811 s5	Stepped	Square	18
LiF 1 (L1)	150813 s7	Flat with LiF window	Square	24

4.6 Introduction to CTH

The experiments provided initial condition and the final condition of the instability growth. Simulations were used to understand how the instability developed in time. Simulations also provided a platform to test the sensitivity of instabilities to material strength.

Instability growth simulations were carried out in CTH, a 3D hydrodynamics code developed by Sandia National Laboratories. The name CTH is not a simple acronym. The name and the code are derived from a predecessor, CHART D, created in 1969. CTH uses a Lagrangian step to calculate deformation. The deformed mesh is then remapped to its original position, preventing large mesh deformations over the course of a simulation. This scheme permits simulation of significant plastic flow [50].

4.7 Geometry definition

Two simplifications were made to the target geometry. First, no glue was simulated. In the conformal targets, the ablator material was used to fill the gaps in the ablator-sample interface. Second, a 220 μm long ablator was used for all targets, matching the polystyrene ablator used in experiments, but not the 250 μm CRF ablator.

The 2D and 3D simulation domains were reduced using no-penetration boundary conditions that enforce zero velocity perpendicular to the domain boundaries. The simulations of 3D targets used a square domain $\sqrt{2}\lambda/4$ on a side (Figure 4.10(a)). The simulation of 2D targets used a domain $\lambda/2$ wide (Figure 4.10(b)).

In a 2D and 3D simulations, the perturbed ablator-sample interface distorted the shock, focusing it in the trough and creating a loading condition that varied across the length of the perturbation. This variation was necessary for the instability to occur, but it made describing the loading condition difficult. Additional 1D simulations of the ablator-sample interface described the behavior of the bulk sample material.

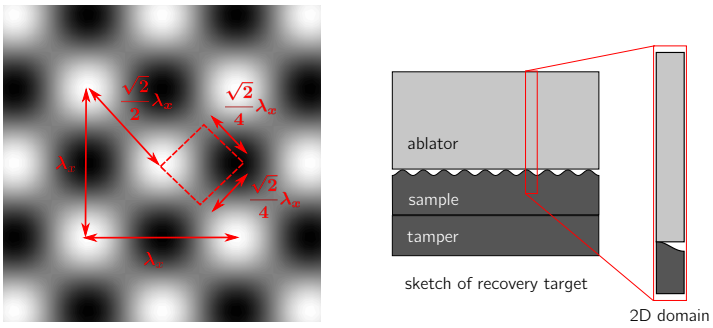

(a) (b)

Figure 4.10: Definition of the domain for 3D targets, the dashed square region in (a). A half wavelength wide domain was used for the 2D simulations (b).

Like the Hyades simulations, this bulk state was calculated by averaging over a region between 1-10 μm into the sample. The maximum pressure in the bulk state during shock passage was defined as the ripple pressure.

When reducing from 2D to 1D, the line crossing the peak of the initial perturbation was chosen. This choice eliminated the distinction between conformal and nonconformal targets in 1D simulations. In either case, the ablator was in contact with the sample.

4.8 CTH simulation scheme

CTH cannot model laser-matter interaction, so a laser cannot be used as the source of the drive. Hyades simulations demonstrated that the energy from the laser was deposited mostly in the first few microns of the ablator. As an approximation of the laser-matter interaction, CTH simulations were initialized with all of the laser energy deposited evenly in the first micron of the ablator, the *energy source*. At the start of each simulation, the energy source expanded rapidly and launched a loading wave through the ablator.

Because the mechanism depositing energy in the ablator was different than laser ablation, the energy required to generate a particular loading wave in CTH was not the same as the energy required to generate the same loading wave in Hyades. However, because both laser ablation and the energy source deposit energy rapidly in a small portion of the ablator, it was assumed the loading wave produced by each would be similar. This assumption allows CTH simulations and experiments to be compared by matching the ripple pressure from the CTH simulation to the ripple pressure determined from the calibrated Hyades simulations.

In summary, drive shot data was used to calibrated Hyades simulations. On a given recovery shot, the pressure experienced by the interface perturbation was determined from the calibrated Hyades simulations. A CTH simulation where the same ripple pressure was produced by the energy source was then used to understand the instability growth in the recovery target.

4.9 Meshing scheme

Two meshing schemes were used to simulate the target geometry. The first scheme was sufficiently resolved to model the expansion of the energy source and the generation of the loading wave. The small width of the energy source required a high mesh resolution. The state of the ablator when the shock had traveled to within 50 μm of the ablator-sample interface was stored. Because the propagation of the shock through the ablator was 1D, the stored state could be used to initialize the ablator in later 1D, 2D, and 3D simulations. After the loading wave had propagated this far, the high energy density and high wave speed conditions behind the shock had dissipated, allowing longer times steps and decreasing the run time of subsequent simulations. The second meshing scheme, designed for simulations initialized after the loading wave was generated, required lower resolution and resulted in shortened run time for 2D and 3D hydrodynamic instability simulations.

CTH allows expanding or contracting zones, where the ratio of consecutive zone lengths is given by r. An expanding mesh is defined with $r > 1$. Sections of mesh with different r can be defined adjacent to each other, providing higher or lower resolution where necessary. Zone width was matched across section boundaries where r was changed.

A vacuum outflow condition, where pressure is set to zero and mass is allowed to leave the mesh, was enforced on the left hand side of the mesh. This boundary condition allowed the expanding ablator plume to exit the mesh. A half space approximating boundary condition was enforced on the right hand side. This boundary condition does not perfectly simulate a half space, however, and produced a small reflection when absorbing the loading wave. The mesh was designed to be long enough so that no reflection from this boundary interfered with the simulation. In 2D and 3D simulations, a no-penetration boundary condition was enforced on the lateral boundaries.

Energy source mesh

A 1D mesh consisting of three sections was used to study the energy source initialization. The main section, in the center, contained the ablator and sample materials, Figure 4.11. The mesh to the left of the ablator was extended to keep the plume from the expanding energy source in the mesh for a small amount of time. The mesh to the right of the sample was extended to approximate a half space and to prevent the loading wave from reaching the boundary of the mesh.

The number of zones in the constant region was set to 4000 in the tantalum simulations and 8000 in the copper simulations as proven sufficient by a mesh convergence study (Appendix B.1).

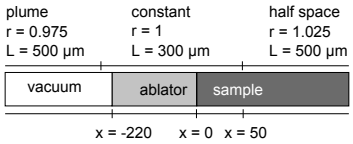

Figure 4.11: Axial variation of mesh used to study energy source initialization. Expansion of zone widths is given by r. The length of the mesh section is L.

Hydrodynamic instability mesh

In hydrodynamic instability simulations, the axial mesh contained a constant section and an expanding section approximating a half space. No ablator-side extension was used as these simulations were initialized after the energy source had expanded and driven a loading wave through most of the ablator. Only 200 μm of the ablator material was meshed, as much of the ablator material has already been converted into a low density ablation plume exiting the domain.

1D simulations, used to determine the bulk state of the sample, consisted of only the axial mesh. 2D and 3D simulations required mesh in the lateral directions. A constant mesh with the same resolution as the constant section of the axial mesh was used in each lateral direction. This mesh definition produced square and cubic zones, in 2D and 3D respectively, in the constant axial mesh section containing the ablator-sample interface. The number of zones in the constant region was set to 300 as proven sufficient by a mesh convergence study (Appendix B.2).

4.10 Source of data from CTH simulations

Data was exported from CTH using Lagrangian tracers which move with the deformation. In the 1D simulations, Lagrangian tracers were embedded in the sample. In the 2D and 3D simulations, 200 tracers per wavelength were embedded 0.5

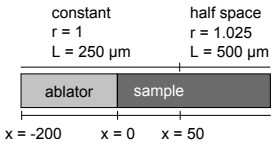

Figure 4.12: Axial variation of mesh used to study instability growth. Expansion of zone widths is given by r. The length of the mesh section is L.

μm beneath the ablator-sample interface perturbation. The tracers moved with the interface as it deformed, recording the location of the interface perturbation.

4.11 Material models

The tantalum targets were modeled using a Mie-Grüneisen EOS and Steinberg-Lund strength model for tantalum and a Sesame EOS for the polystyrene. The Mie-Grüneisen EOS is a good approximation of the tantalum EOS during shock compression.

The copper targets were modeled using a Sesame EOS and Steinberg-Guinan strength model for copper and a Sesame EOS with a P-α porosity model for silica aerogel in place of a model for CRF. CTH contains a Sesame EOS for both carbon and silica aerogel at an initial density of 0.12 g/cc. However, the carbon aerogel generated many warnings and anomalous states during release from a shock compressed state. A comparison between shock compression of the two EOS demonstrated that the two aerogel EOS produced roughly the same loading wave (Figure B.8). Shock compression simulations using the silica aerogel were not free of warnings, but the loading wave release was smoother.

The strength model of the sample material was varied to determine the influence of strength on the instability growth. When studying tantalum, the Steinberg-Guinan strength model was used in place of the Steinberg-Lund strength model. The Steinberg-Lund strength model for tantalum saturates at a strain rate around 10^5 1/s, resulting in rate independent strength. Instability growth took place at higher strain rates, meaning a rate independent model captured the relevant strength behavior in the Steinberg-Lund model.

To scale the Steinberg-Guinan model, the constant multiplier Y_0 and the maximum yield stress $Y_{\max}$ were scaled equally. For example, a doubly strong Steinberg-Guinan model, written $2 \times SG$, used $2 \times Y_{\max}$ and $2 \times Y_0$.

Chapter 5

RESULTS

Three paths of analysis were brought together to generate results. First, Hyades simulations of the laser-ablation drive were calibrated to experimental drive shot data. The calibrated simulations were used to calculate the loading condition experienced by the sample during separate experimental recovery shots. Second, CTH simulations of 2D and 3D instability growth were performed for a range of loading conditions approximating those achieved during the experiment. Third, the perturbation growth was measured in experimental recovery shots.

5.1 Loading felt by the sample

The bulk states generated by the loading wave were studied for a range of energy sources using CTH. In a CH ablator, the energy source created a loading wave with three important features, shown in Figure 5.1. The first was a shock. Following the shock was a release to a plateau at intermediate pressure. After approximately 10 ns, a second release brought the state down to nearly zero pressure. For the smallest energy sources, the first release and the second release blended together, resulting in a single release from the shocked state.

The spatial averaging in the bulk state calculation smoothed out shock waves. While the 5 J energy source seems to produce a velocity ramp (Figure 5.1), the loading was a shock wave. When the shock entered the sample, only the first 1-2 μm was shocked to a high pressure, so the average over 1-10 μm results in a relatively low average velocity compared to a few nanosecond later when the entire 1-10 μm region was moving at the shocked particle velocity.

The loading wave generated by the CRF energy source was simpler (Figure 5.1). The sample shocked to a high pressure state. This shocked state immediately released, taking the sample to zero pressure.

The amount of energy in the energy source is not an intuitive way to refer to a certain loading wave. Future sections refer to the ripple pressure, the maximum bulk pressure during the loading, instead.

These loading conditions were generated by the expansion of a small region of the ablator initialized at a higher energy state, mimicking laser ablation. The

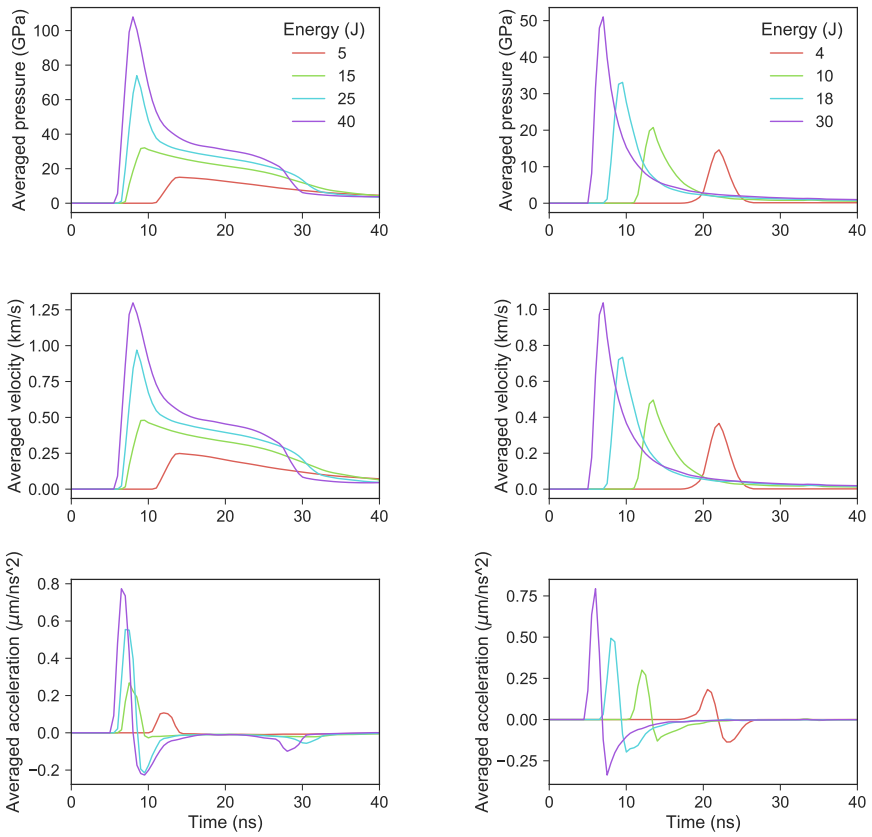

Figure 5.1: Bulk properties created by loading wave in the CH-tantalum target (a) and in the CRF-copper target (b).

resulting loading waves only approximate the loading waves generated in a laser ablation simulation (Figure 4.1). To evaluate this approximation, CTH energy source loading conditions were plotted with the most similar loading condition from Hyades in Figure 5.2. For low ripple pressures loading waves in the CH-tantalum targets, Hyades predicted a faster release than in CTH. At high ripple pressures, the two codes roughly agreed, but Hyades predicted a shorter intermediate pressure plateau than CTH did. In the CRF drive at low ripple pressures, Hyades predicted a longer release than CTH did. Again, the codes agreed better at higher ripple pressure.

5.2 Influence of loading on growth factor

The classic RMI and RTI models assume a supported shock and a constant acceleration, respectively. The loading waves in CH-tantalum and in CRF-copper targets differ from these classic cases. The development of the instability was due to both

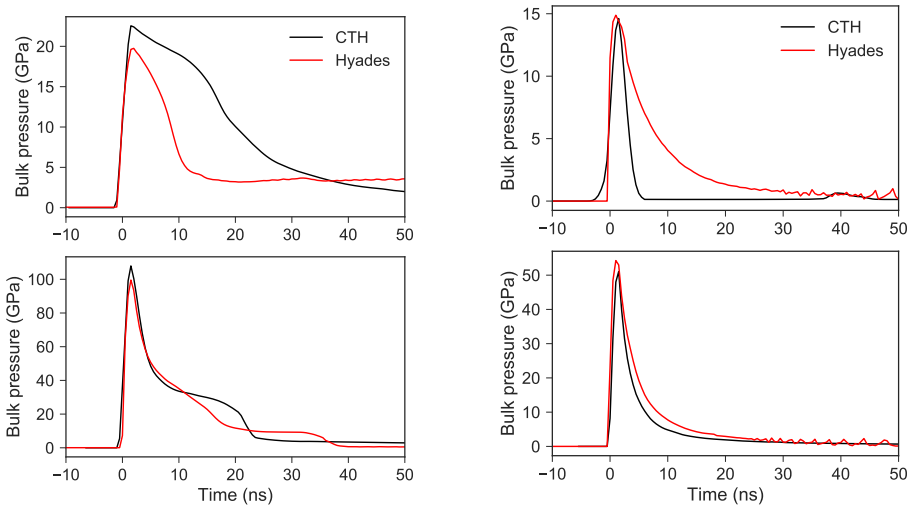

Figure 5.2: Bulk pressure created by two different loading waves from the CH-tantalum target (a) and from the CRF-copper target (b) calculated in CTH and in Hyades. The ripple pressure in each simulation was not precisely matched across codes, so this comparison is qualitative.

a shock and an acceleration which varied with time. To understand how the loading wave affected the instability, the growth of the perturbation amplitude in CTH simulations was studied with no strength model.

In the CH-tantalum simulations, the amplitude shrunk as the material at the ablator-sample interface was compressed by the shock. Immediately afterwards, RMI caused a steep rise in amplitude. The first release corresponded to a slight decrease in growth rate, most apparent with a 108 GPa ripple pressure, Figure 5.3. The second release halted and reversed growth. The strongest drives also caused the strongest releases, reducing the amplitude to its initial value by the end of the simulation.

The release created spikes in the trough of the ripple which outgrew the ripple peaks. When this happened, the growth factor stopped being a measure of ripple peak to ripple valley and instead measured the distance between the spike tip and the ripple valley, causing the abrupt growth towards the end of the simulation for the 108 GPa ripple pressure drive.

The CRF drive similarly caused a steep rise in amplitude due to RMI, followed by a decrease in growth rate due to the release (Figure 5.4). There was no second release and amplitude growth continued unabated, closely following a linear growth rate. The lack of a second release allowed the interface to develop into a more classic

RMI shape by the end of the simulation.

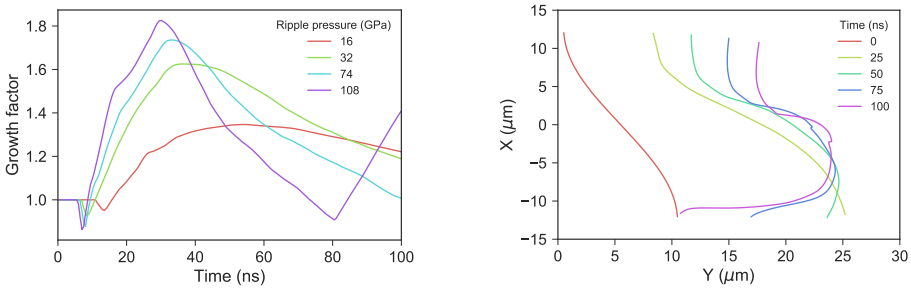

(a) (b)

Figure 5.3: Evolution of 2D perturbation amplitude without strength in the tantalum targets for different ripple pressure drives (a) and snapshots of the instability growth at different times due to a 108 GPa ripple pressure (b).

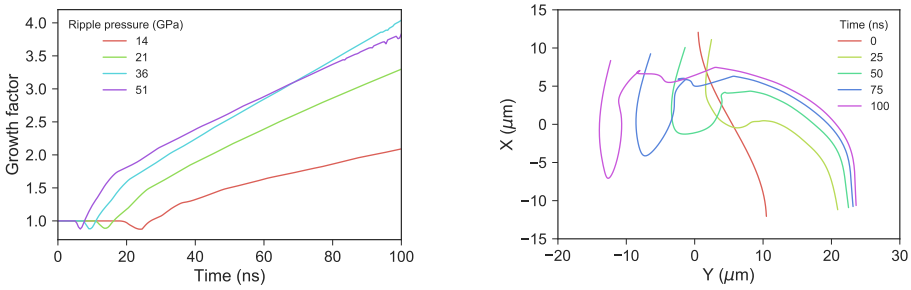

(a) (b)

Figure 5.4: Evolution of 2D perturbation amplitude without strength in the copper targets for different ripple pressure drives (a) and snapshots of the instability growth at different times due to a 51 GPa ripple pressure (b).

The differences between the CTH and the Hyades loading conditions are important to remember when interpreting CTH instability results. At low ripple pressures the CTH loading wave, more similar to a supported shock, would drive more RMI growth than the Hyades loading wave would. Conversely the low ripple pressure CRF drives would result in less growth than Hyades simulations predict.

5.3 Influence of strength on growth factor

Adding strength to the CTH instability simulations arrested the instability after a period of growth. In the CH-tantalum targets (Figure 5.5), the lowest ripple pressure loading waves resulted in instability growth which reached a maximum growth factor and then stopped. Higher ripple pressure drives achieved higher growth factor maximums, but the stronger release decreased the amplitude before growth

was arrested. No spike in the trough was formed, but the trough was flattened by the release.

The lower ripple pressure drives, where increasing ripple pressure increased recovered growth factor, are referred to as *RMI-dominated* results. The RMI growth was the most significant contributor to the recovered growth as ripple pressure was increased. The higher ripple pressure drives, where increasing ripple pressure decreased the recovered growth factor are referred to as *RTI-dominated* results. As the ripple pressure was increased, the increasing strength of the release was more influential than the increase in initial RMI growth rate and recovered growth factor decreased.

In the copper targets, Figure 5.6, the lack of a second release meant the instability growth was arrested at or near its maximum value, resulting in RMI-dominated behavior for all ripple pressures. Melt at the ablator-copper interface freed a small amount of the copper at the interface from the bulk material, forming the spikes at late time. For 51 GPa ripple pressure, this small spike resulted in the bump in growth factor at the end of the simulation.

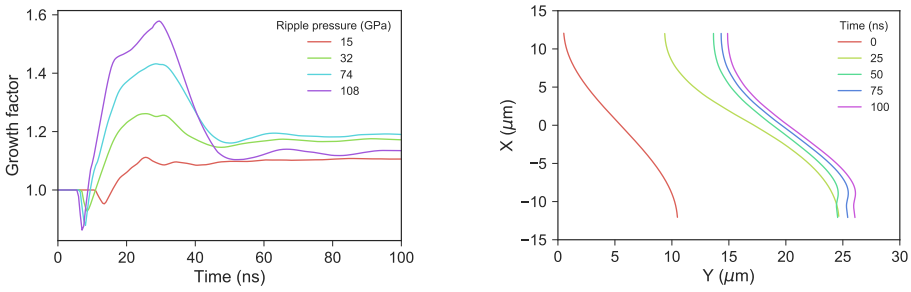

(a) (b)

Figure 5.5: Evolution of 2D perturbation amplitude with strength in the tantalum targets for different ripple pressure drives (a) and snapshots of the interface growth due to a 108 GPa ripple pressure (b).

5.4 Loading relevant during instability growth

The instability growth was affected by the material strength which was in turn a function of the material state. It is important to identify the conditions the material was under during instability growth. In addition to the thermodynamic state, the SG strength model is a function of plastic strain and the SL strength model is also a function of plastic strain rate. As an example, the lowest and the highest energy

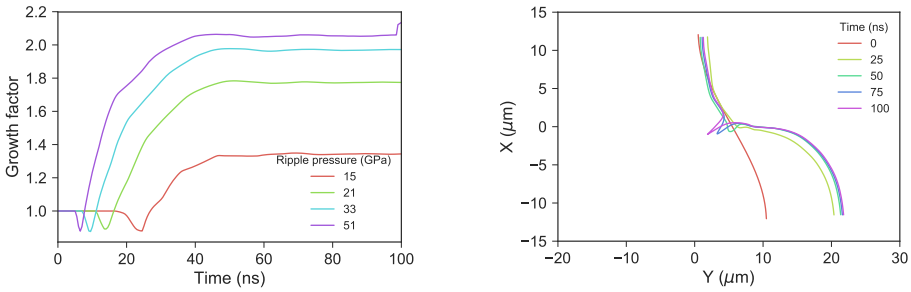

(a) (b)

Figure 5.6: Evolution of 2D perturbation amplitude with strength in the copper targets for different ripple pressure drives (a) and snapshots of the interface growth due to a 51 GPa ripple pressure (b).

1D energy source drives were studied in the CH ablator (Figure 5.7) and in the CRF ablator (Figure 5.8).

In the low energy CH drive, the ablator-sample interface experienced a shock and then a release. The interface released half the shocked pressure by the time the instability growth ceased. At high energy, the highest pressure was maintained only for the initial compression of the interface, before RMI growth started. During RMI growth, the bulk pressure dropped to a intermediate plateau, approximately 30 GPa. As the second release dropped the interface pressure to zero, the amplitude reversed growth.

The plastic strain rate covered three decades during the 20 ns of amplitude evolution. The amplitude growth due to RMI was influenced by the strength at strain rates above 10^7 1/s. During the pressure plateau and final amplitude growth, the strain rate dropped to 10^6 1/s. During the second release, strain rate dropped further, into the 10^5 1/s decade. The transition from 10^6 1/s to 10^5 1/s is vital to the SL strength model for tantalum. At the upper end of this strain rate range, the strength saturates and becomes strain rate dependent. To the SL strength model, the strength should be strain rate independent during the instability growth, but becomes strain rate dependent during the reversal of amplitude growth.

In the CRF drive, the highest pressure was again maintained only for the initial RMI growth. The bulk pressure released below 10 GPa before the RMI growth was half over. As in the CH-tantalum target simulations, the plastic strain rate states spanned three decades, from 10^5 1/s to 10^8 1/s during the instability growth.

Because the strain rate component of the SL strength model is saturated at these

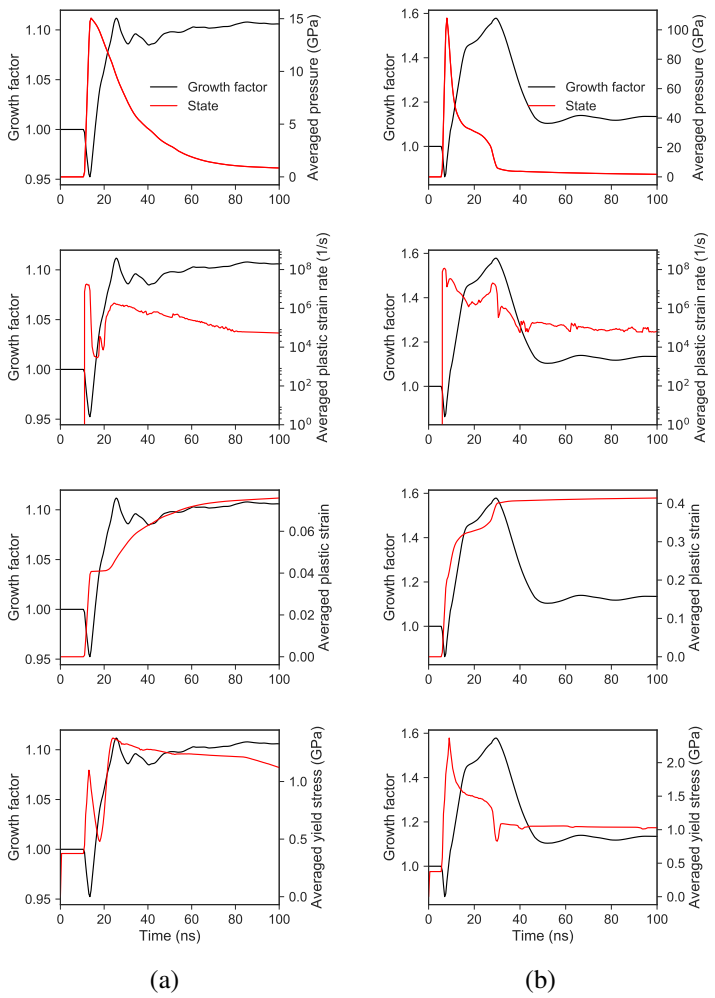

Figure 5.7: Bulk states compared to the amplitude growth in the CH-tantalum target for the 5 J energy source (a) and the 40 J energy source (b).

strain rates, it is easier to think about strength in terms of the SG model. In tantalum samples, the most important effect was pressure hardening. The ambient value of strength in tantalum is 770 MPa with an upper limit due to work hardened tantalum set at 1.1 GPa. As the shock compressed the sample, the yield strength increased by a factor of roughly 1.2 to 2.0 over the range of ripple pressures simulated. Work hardening increased strength by a factor up to 1.4. Thermal softening due to shock heating reduced the strength in the released sample. In the highest ripple pressure drive, the final strength was approximately 0.8 its ambient value.

Copper has a higher work hardening exponent than tantalum and felt a greater contribution from work hardening than pressure hardening. The ambient value of strength in copper is 120 MPa with an upper limit due to work hardening set at 640

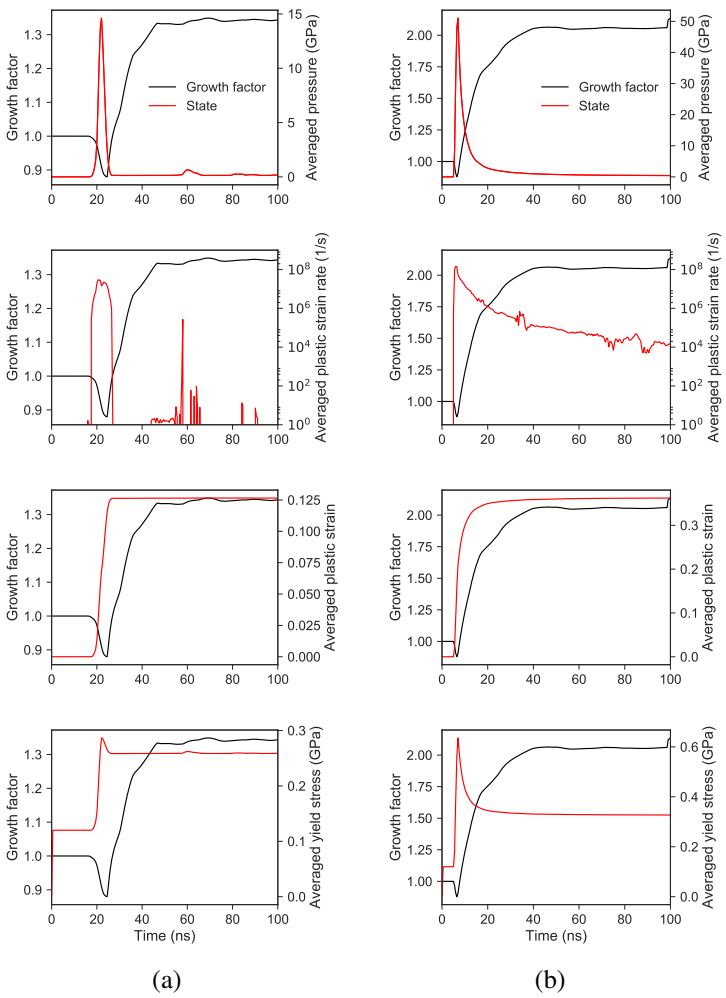

Figure 5.8: Bulk states compared to the amplitude growth in the CRF-copper target for the 4 J energy source (a) and the 30 J energy source (b).

MPa. Pressure hardening increased strength by a factor from 1.4 to 2.0 over the range of ripple pressures. The 1D states plotted in Figure 5.8 are a good estimate of the state near the perturbation in the 2D and 3D targets. However, the 1D plastic strain underestimated the strain near a 2D or 3D perturbation. During instability growth, some parts of the ripple experienced strain up to 1.0. Work hardening during the lowest ripple pressure drives doubled the strength of the copper. At the highest ripple pressure, strength was increased by a factor of 4. As in tantalum, thermal softening caused by shock heating reduced the strength in the released copper to roughly 0.8 its ambient value.

5.5 Sensitivity of growth factor in tantalum samples to strength variation

The strain rate dependence in the SL model was saturated for most of the instability growth, so the SL model was replaced by the simpler strain rate independent SG model. The maximum growth factor achieved during the simulation and the final growth factor at the end of the simulation were compared (Figure 5.9). The final growth factor was calculated by averaging the amplitude from 80 ns to 100 ns to remove the contribution of small oscillations after growth stopped.

The maximum growth factor increased as drive strength increased, expected as stronger shock waves cause a larger initial RMI growth rate. A stronger strength model reduced the maximum growth factor.

The relationship between final growth factor and drive strength changed with the strength model. The weakest and most fluid-like strength model, $1/2 \times SG$, did the least to arrest amplitude growth. The lowest ripple pressure drives did not posses a strong enough release to undo the RMI amplitude growth, so the strength preserved more and more amplitude. However, once the release became significant, the final growth factor decreased with increasing drive strength. Increasing the strength of the material forced this transition point to higher ripple pressure drives. Increasing strength decreased the maximum achievable final growth factor and extended the range of RMI-dominated results to higher ripple pressures. Consequently, a stronger sample could produce more recovered growth than a weaker sample, if the stronger sample growth was RMI-dominated while the weaker sample growth was RTI-dominated.

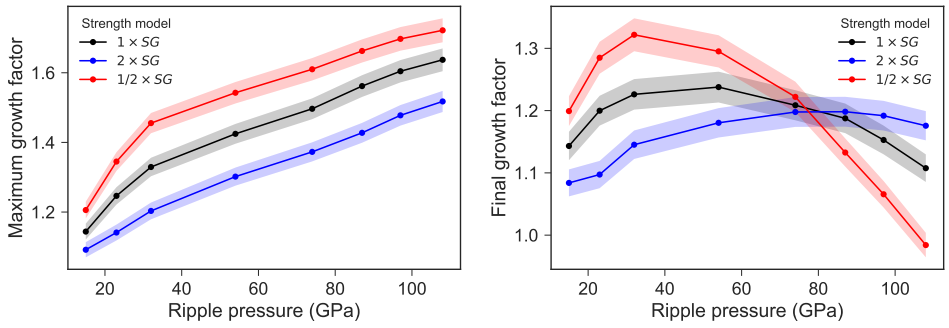

(a) (b)

Figure 5.9: Maximum achieved growth factor (a) and final recovered growth factor (b) in the CH-tantalum targets with different strength models.

5.6 Sensitivity of growth factor in copper samples to strength variation

Simulations of the copper targets were compared to simulations using a stronger model, $2 \times SG$, and a weaker model, $1/2 \times SG$, Figure 5.10. All results were RMI-dominated. Stronger drives caused higher initial instability growth rate and higher final growth factor. Weakening the strength model resulted in higher recovered growth. The strength of copper as a function of initial temperature was also studied. A higher initial temperature resulted in a higher temperature in the shocked state and decreased strength, causing a larger final growth factor. Increases spanned 1-2 μm for a 500 K temperature increase.

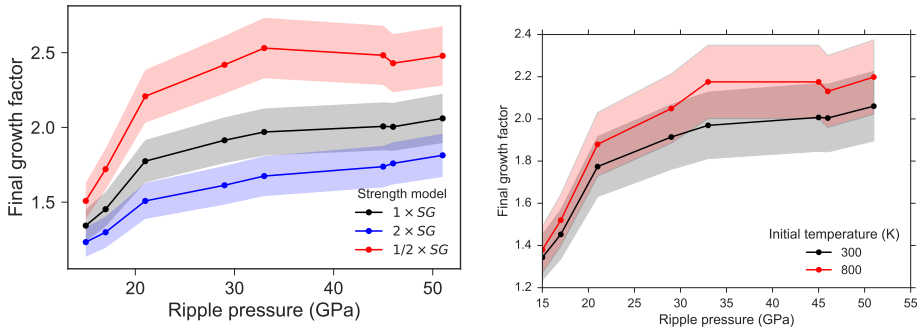

Figure 5.10: Final growth factor in the CRF-copper targets with different strength models (a) and different initial temperatures (b).

5.7 The influence of wavelength on growth factor

Decreasing the initial perturbation wavelength increases the growth rate of the RMI and the RTI. To study the influence of wavelength on instability growth due a shock and a release, additional 2D simulations were run with a 71 μm and a 100 μm wavelength.

In simulations of CH-tantalum targets (Figure 5.11) the maximum growth factor increased as wavelength decreased, the result of a higher initial RMI growth rate. The 50 μm wavelength results transitioned from RMI-dominated to RTI-dominated regimes. The larger wavelength perturbations remained RMI-dominated for all drives simulated. All results in the CRF-copper simulations were RMI-dominated (Figure 5.12).

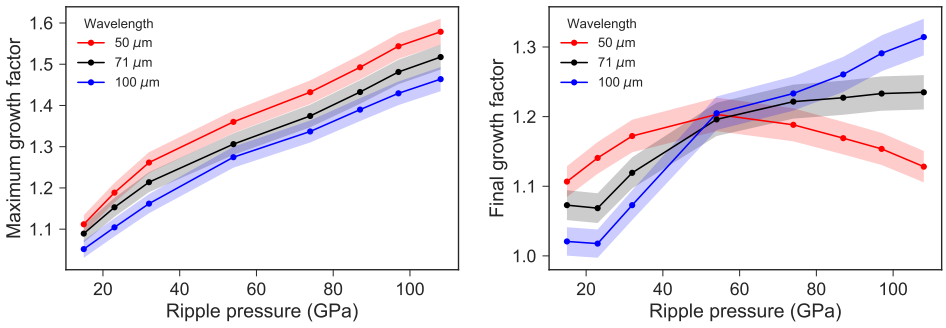

(a) (b)

Figure 5.11: Maximum (a) and final (b) growth factor for 2D CH-tantalum targets with different wavelength initial perturbations.

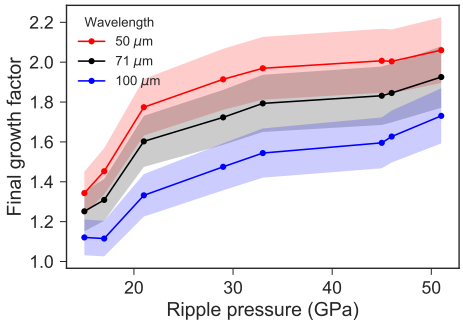

Figure 5.12: Maximum growth factor for 2D CRF-copper targets with different wavelength initial perturbations.

5.8 The influence of 2D or 3D initial perturbations on growth factor

Simulations of 3D perturbations used a wavelength $\lambda_x = \lambda_y = 100$ μm with $\lambda = 50\sqrt{2}$ μm to match experimental results. The 3D results were compared to 2D simulations with a $\lambda = \lambda_x = 50\sqrt{2}$ μm wavelength. From the results of Section 5.7, all 2D simulations with $\lambda = 50\sqrt{2}$ μm were RMI-dominated.

Matching the wavelength in 2D and 3D simulations resulted in identical initial instability growth rate. As the perturbations grew, the growth rates eventually slowed and the 3D perturbations outgrew the 2D perturbations (Figure 5.13). Subjected to the higher ripple pressure drive, 3D perturbation outgrew the 2D perturbation, but the amplitude of the 3D perturbation shrunk more rapidly than the 2D perturbation during the release, resulting in a lower final amplitude.

The 2D and 3D simulations were compared using different strength models (Figure 5.14). The unmodified and strengthened SG model resulted in RMI-dominated behavior for all ripple pressures. The weakened SG model, however, allowed

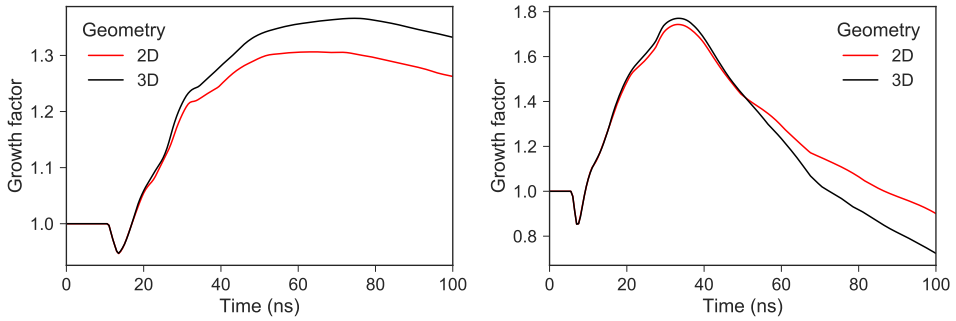

(a) (b)

Figure 5.13: Amplitude evolution in CH-tantalum targets with no strength shocked to 16 GPa ripple pressure (a) and 108 GPa ripple pressure (b).

a transition into RTI-dominated behavior in the CH-tantalum targets. The 3D perturbation growth was lower, seemingly consistent with a slightly stronger sample, and was quite similar to the 2D perturbation growth in a stronger sample. The best agreement is between the 3D $1/2\times SG$ simulation and the 2D $1\times SG$ simulation. In CRF-copper simulations, the final growth factors in 3D targets were lower than in the 2D simulations, similar to the effect of strengthening the sample (Figure 5.10(a)).

The 2D and 3D simulations were also compared by subtracting the final growth factor in the 2D simulations from the final growth factor 3D simulations (Figure 5.15). In the CH-tantalum targets, the decreasing slope of the difference between 2D and 3D final growth factor indicated that the 3D targets grew more relative to the 2D targets as ripple pressure increased. Distinguishing a trend with strength was not possible given the uncertainty.

All simulations of the CRF-copper targets were RMI-dominated. Despite the large uncertainty, the difference between recovered amplitude was roughly constant, without the slope seen in the CH-tantalum targets, consistent with the approximately RMI growth in the CRF-copper targets. No trend with strength is discernible.

5.9 Images of recovered instability growth

Scanning electron microscope (SEM) images helped comprehend the deformation caused by the laser ablation drive. Images of a tantalum samples with 2D initial perturbations (Figure 5.16) and 3D initial perturbations (Figure 5.17) showed surface features varying radially from the shot center. At the shot center, the surface was covered with micron-sized features that may be due to the melting of ablator-sample interface. This region, in samples driven using then 1 mm^2 spot area square phase

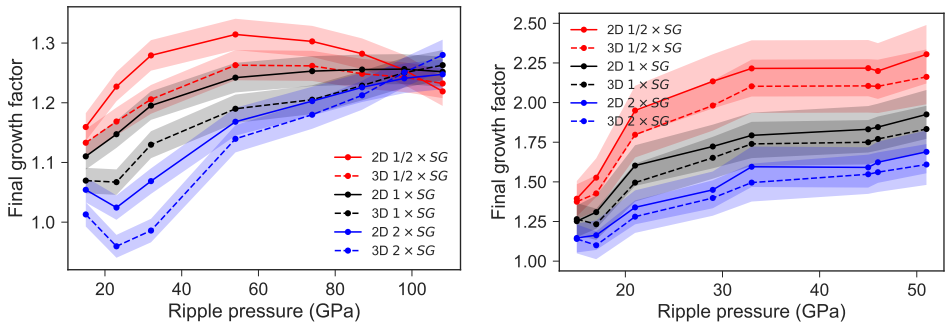

Figure 5.14: Final growth factor for 2D initial perturbations and 3D initial perturbations for simulations with CH-tantalum targets (a) and CRF-copper targets (b) with different strength models.

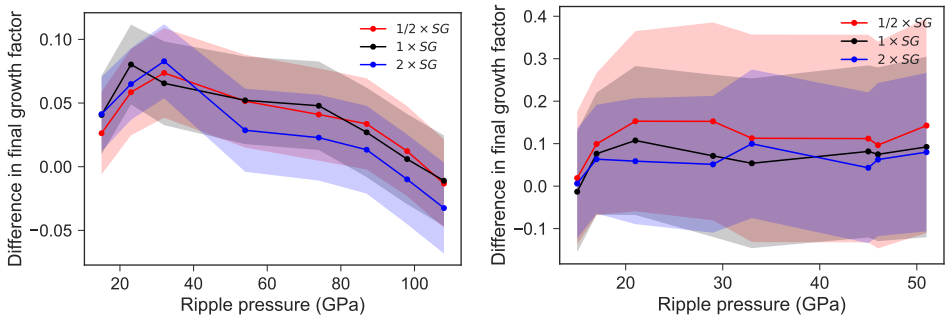

Figure 5.15: Difference in final growth factor for 2D initial perturbations with respect to 3D initial perturbations for simulations with CH-tantalum targets (a) and CRF-copper targets (b) with different strength models. A positive value means the 2D final amplitude was larger than the 3D final amplitude.

plate, was approximately 500 μm in diameter. Outside this region was another region, approximately 1 mm in diameter, with finer surface features. The surface does not appear affected by the drive outside of this region. The change in surface features indicated a change in loading conditions, meaning radial effects became important at most 250 μm from the shot center.

SEM images of recovered copper samples with 2D (Figure 5.18) and 3D (Figure 5.19) initial perturbations showed more severe deformation than the images of recovered tantalum samples. Both 2D and 3D perturbations were more irregular, with deviations from the initially periodic pattern evident in the second image in each figure. The 2D peaks seem truncated. Unlike the tantalum samples, the shot

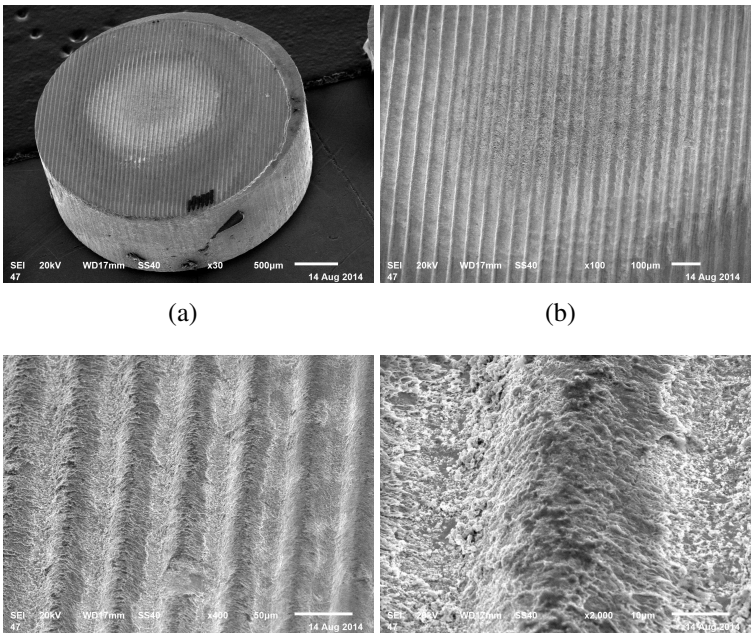

(a) (b)

(c) (d)

Figure 5.16: SEM images of a 2D tantalum sample driven with 110 GPa ripple pressure using the square phase plate, at increasing levels of zoom.

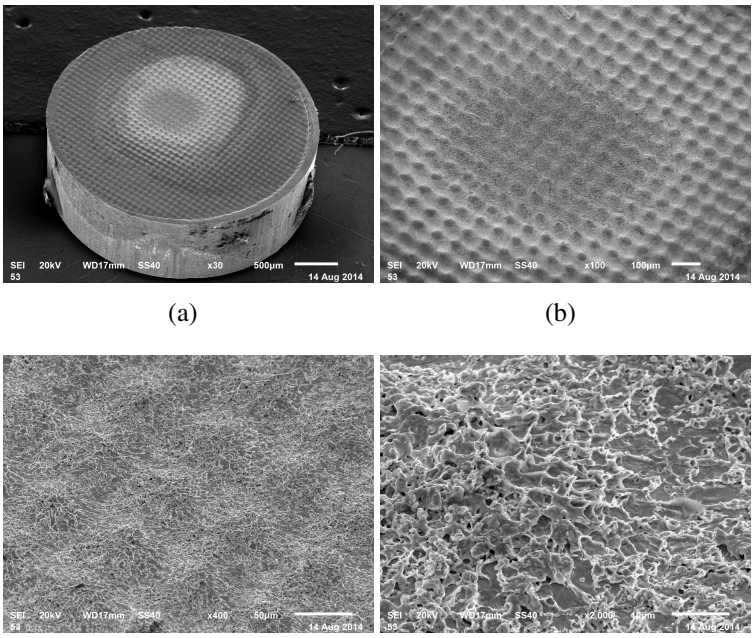

(a) (b)

(c) (d)

Figure 5.17: SEM images of a 3D tantalum sample driven with 120 GPa ripple pressure using the square phase plate, at increasing levels of zoom.

area was not clearly defined, but appeared to be at least 500 μm in diameter.

5.10 Experimentally recovered growth factors

If the driven region was 1D, then there should be no radial variation of PTV from the shot center. This assumption will break down at some point. The limiting cases for the 1D assumption were set by the recovery targets shot with the smaller approximately 600 μm diameter phase plate during the 2014 campaign. Based on 2D cylindrical simulations of the shock propagation through the ablator, 1D behavior was assumed to hold in a circle of radius 100 μm from the shot center.

The experimentally determined growth factors for R_c = 100 μm were plotted using ripple pressures determined from calibrated Hyades simulations. The uncertainty in growth factor was derived from the standard deviation of the PTV in the averaged region. The uncertainty in ripple pressure was derived from the uncertainty in the Hyades calibration to drive shot data.

The transition between RMI- and RTI-dominated regimes was not clear in the tantalum sample experimental results (Figure 5.20). The lowest ripple pressure drives produced a growth factor of 1.2 for 2D and 3D initial perturbations. In the 2D results, growth factor plateaued around 50 GPa. Starting at roughly 60 GPa, the recovered 2D perturbations grew with ripple pressure to a maximum 1.4 growth factor. At the highest ripple pressures, growth factor decreased. Importantly, the wavenumber of the 2D and 3D initial perturbations are not matched so they cannot be compared directly, but they can be compared to simulation results.

The CRF-copper targets exhibited a clearer trend, Figure 5.21. The growth started at ripple pressures below the weakest drive achievable during the experiment. The growth occurred over a small range of ripple pressures, approximately 10 GPa, before saturating. The 3D targets reached the same growth factors as the 2D targets at a higher ripple pressure. The 2D targets reached a growth factor of 2.2 at the highest ripple pressure, while the 3D targets saturated at a growth factor of approximately 2.0.

5.11 Growth uniformity

The process of producing a single growth factor data point for a recovery target removed any information about spatial variations of PTV. The calculated post-shot PTV did vary with radius from the shot center (Figure 5.22) indicated by an increase of the cumulative PTV uncertainty with radius. Small increases in local uncertainty

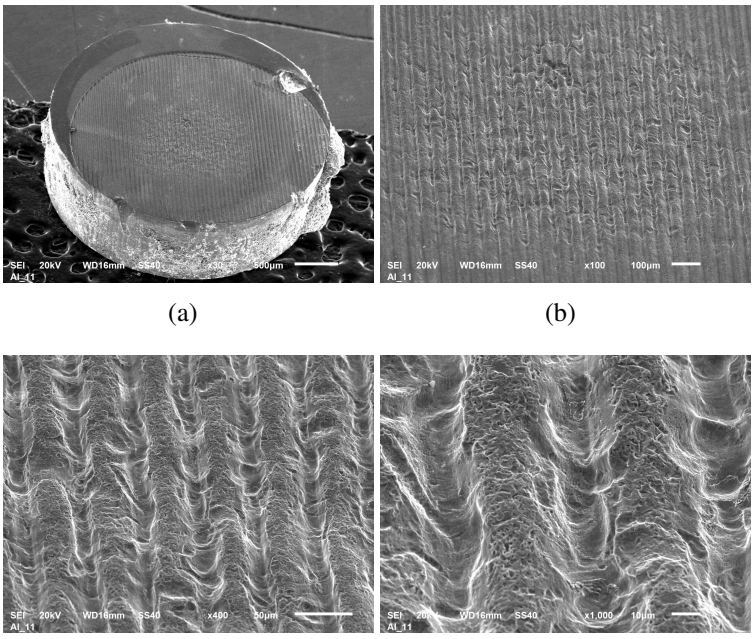

(a) (b)

(c) (d)

Figure 5.18: SEM images of a 2D copper sample driven with 10 GPa ripple pressure using the square phase plate, at increasing levels of zoom.

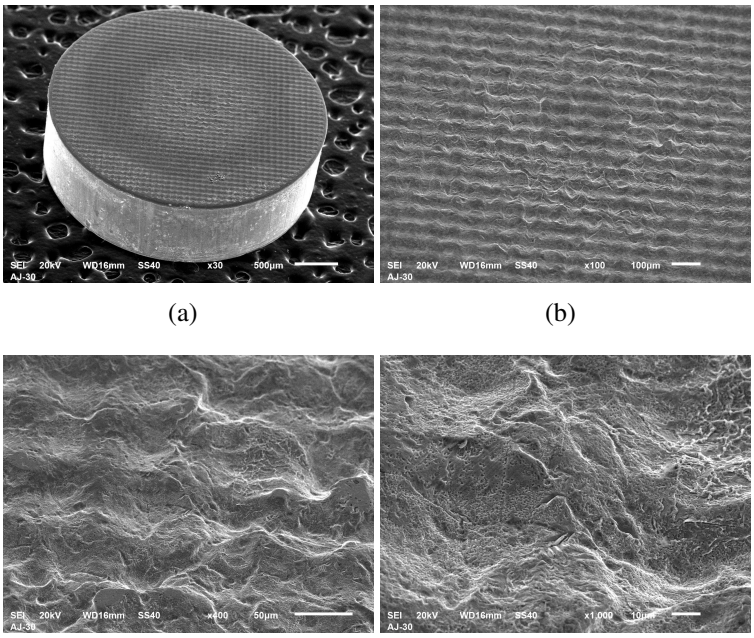

(a) (b)

(c) (d)

Figure 5.19: SEM images of a 3D copper sample driven with 10 GPa ripple pressure using the square phase plate, at increasing levels of zoom.

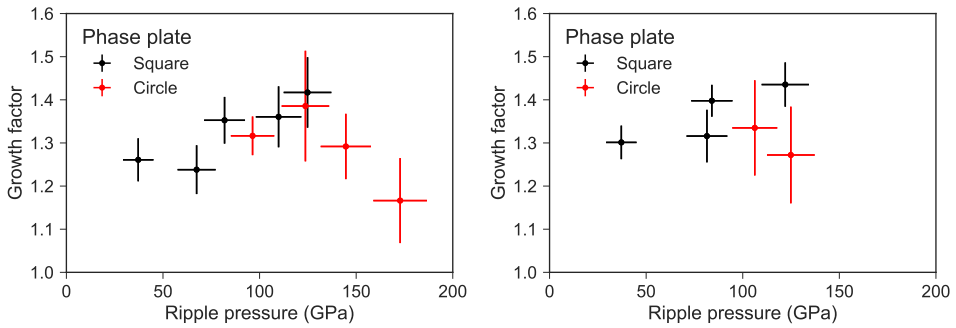

(a) (b)

Figure 5.20: Experimental recovered growth factor in tantalum samples with 2D (a) and 3D (b) initial perturbations.

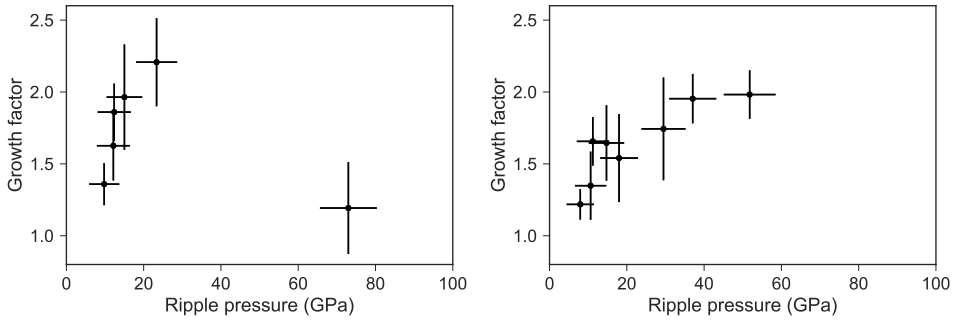

(a) (b)

Figure 5.21: Experimental recovered growth factor in copper samples with 2D (a) and 3D (b) initial perturbations.

in the pre-shot profile were due to long wavelength deformation in the sample. Cumulative uncertainty, however, was small.

The growth factor calculation depended on the choice of filter. Filtering removed surface features that were not part of the instability growth and contributed at least 1 μm of growth to the recovered PTV. However, filtering also removed some periodic content that was part of the instability growth. The filter removed periodic content from both pre- and post-shot profiles, so some of the difference was offset when calculating the growth factor. To bound the influence of the filter, two data sets were created, with and without a 2 μm Gaussian filter.

The recovered PTV was calculated using R_c = 100 μm and R_c = 250 μm for each filter Figure 5.23. Differences between the filtered and unfiltered results were due to the influence of surface features. Tantalum samples were more affected by the

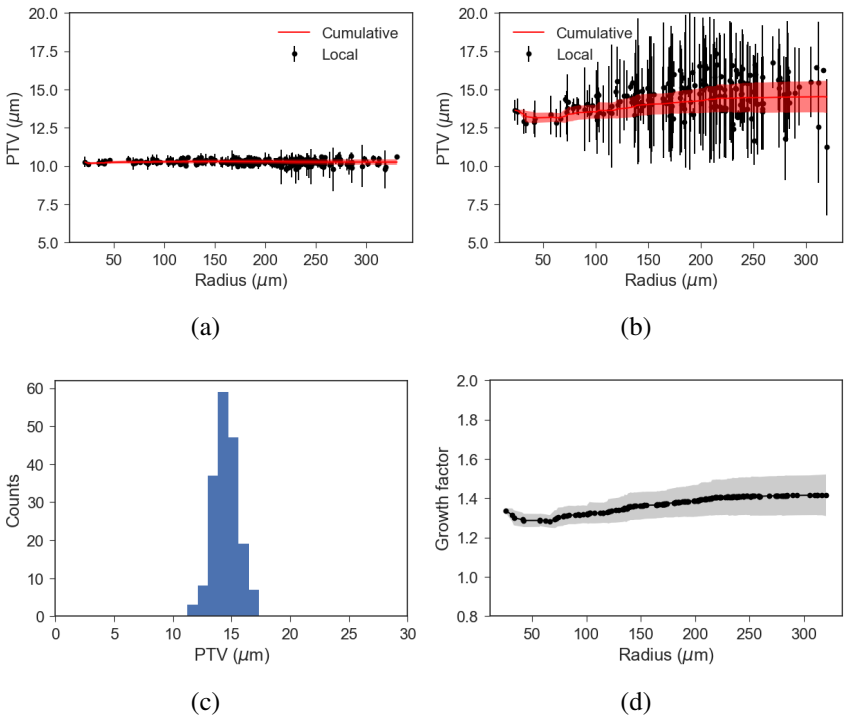

Figure 5.22: Summary of PTV statistics for a 2D tantalum sample driven with 100 GPa ripple pressure using the small circular phase plate and analyzed with no filter. Plotted is the PTV in the pre-shot profile (a), the PTV in the post-shot profile (b), a histogram of the PTV in the post-shot profile (c), and the growth factor as a function of radius from the shot center (d).

filter than copper samples.

5.12 Comparison between recovered growth factor from experiment and simulation

In the CH-tantalum targets, both the maximum and the final recovered growth factor determined from simulations were plotted to bound the growth factor range reached in simulations. The simulations correctly predicted the plateau of recovered growth factor at low ripple pressure in 2D samples (Figure 5.24). This plateau in growth factor corresponds to the transition between RMI-dominated and RTI-dominated behavior. However, at higher ripple pressures, the experiment disagreed with the simulations. The experimentally recovered growth factor continued to grow, whereas growth factor decreased in simulations. The filtered results agreed better with simulations than the unfiltered results.

The experimentally recovered 3D sample PTV fell between the final and maximum PTV determined from simulation. The simulations predicted RMI-dominated be-

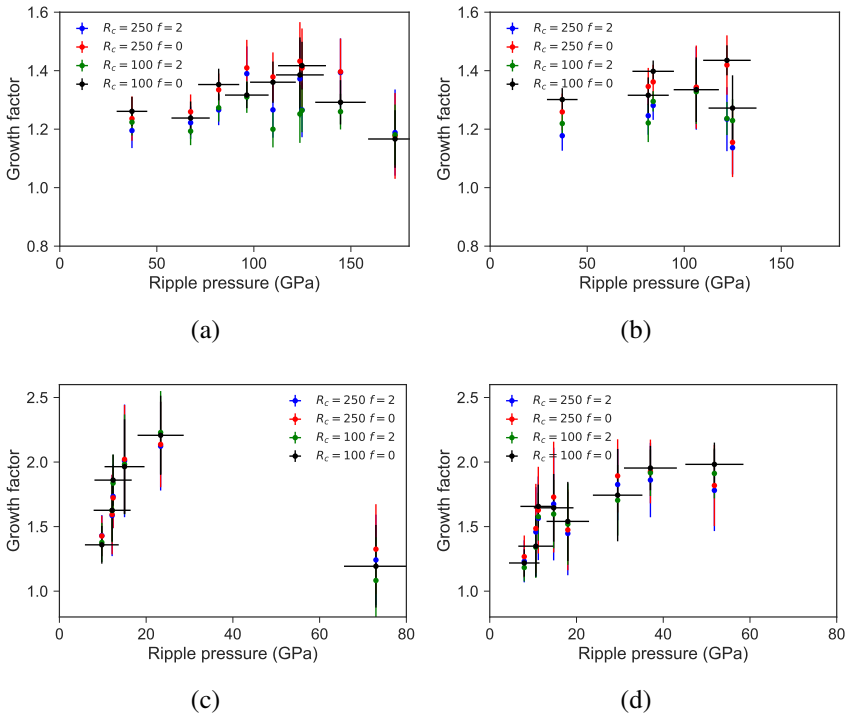

Figure 5.23: Growth factor plots of all recovered samples using different values of R_c and different filtering to calculate the final growth factor. Plots are for 2D tantalum (a), 3D tantalum (b), 2D copper (c), and 3D copper (d) samples. Values of R_c and f are in microns.

havior. The experimental results, however, do not show a clear trend of growth factor with ripple pressure.

Several explanations are possible for the difference between simulation and experimental growth factors for 2D initial perturbations. One, the approximation of the drive used in CTH simulations could be incorrect. Hyades simulations predicted a sharper release than CTH at low ripple pressures. However, this is the opposite trend that is needed to bring simulations in line with experiments. Further, CTH and Hyades simulations agreed at higher ripple pressure where the disagreement between simulation and experiment is the largest. Two, the model for tantalum could be incorrect at these conditions. However, similar deviations would be expected in the 3D targets near these states. The 3D simulations would agree better with experiment at low ripple pressures if the strength model were weakened. Weakening the strength model in the RTI-dominated 2D simulations would decrease the recovered growth, taking experiment and simulation out of agreement. Three, the interpretation of RTI-dominated regime is incorrect.

The last explanation seems to be the most likely, as it accounts for the poor agreement in the higher ripple pressure 2D targets and better agreement in the higher ripple pressure 3D targets; the 3D targets are larger wavelength and are still RMI-dominated at the higher ripple pressures. Consequently, it is likely the recovered growth factor after the transition to RTI-dominated behavior is poorly predicted by simulations.

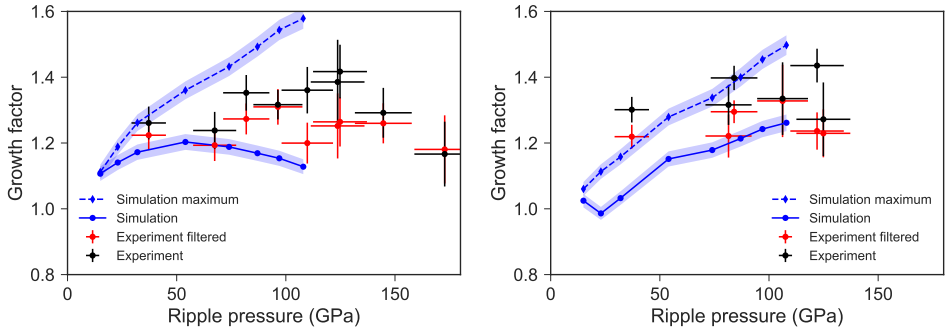

Figure 5.24: Experimental recovered growth factor in tantalum with 2D (a) and 3D (b) initial perturbations compared to simulation results.

In the CRF-copper comparison (Figure 5.25) the simulations consistently predicted lower growth factors than seen in the experiment. Again, offsets could be due to poor simulation of the laser drive or a difference in the material model. Liberal assumptions, using a quartz aerogel EOS at 0.12 mg/cc instead of the CRF at 0.115 g/cc in the manufactured target and using instantaneously deposited energy instead of modeling laser ablation, were necessary to run CRF-copper simulations in CTH.

The 3D simulations predicted that the growth factor saturate near 1.8 as ripple pressure increased. Strengthening or weakening the strength model would decrease agreement with experiment here. The difference between results from experiment and simulation could not be accounted for by changing the strength model. This disagreement leads to the conclusion that the energy source drive used in CTH simulations produced too little RMI growth in CRF-copper targets at ripple pressures below 30 GPa.

5.13 Inferring strength from recovered growth factor

In all comparisons between CTH and experimental results of RMI-dominated growth, the CTH simulations predicted lower growth than the experimental results. Doubt about the accuracy of the drive modeled in CTH makes it impossible to assign all offsets solely to differences in strength. However, disagreement be-

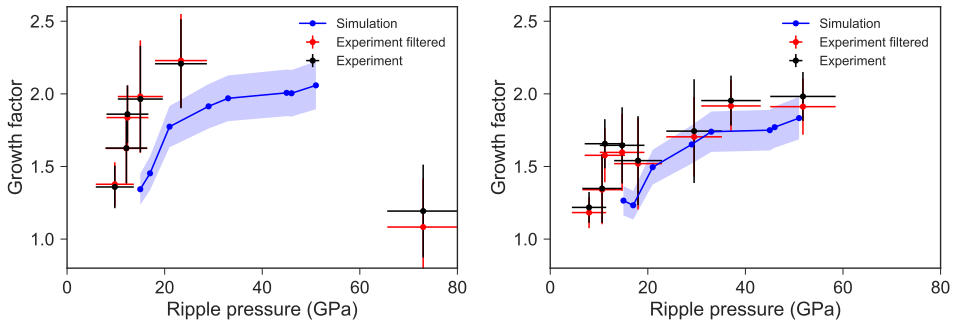

(a) (b)

Figure 5.25: Experimental recovered growth factor in copper with 2D (a) and 3D (b) initial perturbations compared to simulation results.

tween the CTH energy source drive simulations and the Hyades laser ablation drive simulations change with ripple pressure. It would be interesting if a weakening or strengthening of the strength model brings the simulations and experiments in closer agreement for a wide range of ripple pressures.

Tantalum samples

The $1/2 \times SG$ model was used to simulate the instability growth (Figure 5.26). Most recovered 2D tantalum samples fell beyond the RMI-dominated range. Two recovered samples were driven to the transition between RMI- and RTI-dominated behavior. Weakening the strength model shifted the transition to RTI-dominated behavior to lower ripple pressure. The half strength model weakened the tantalum too much, resulting in an overshoot of the lowest ripple pressure 2D data point. In 3D, the half strength model simulation predicted a recovered growth factor within experimental uncertainty of the filtered growth factors. This is only a slight improvement over the original strength model, where the simulation results were mostly in agreement with experimental results with the exception of the lowest ripple pressure result. Improving the match between simulation and experiment would require strengthening the 2D simulations without altering the 3D simulations, which is impossible.

Copper samples

Weakening the copper, by using the $1/2 \times SG$ strength model, slightly improved agreement between experiment and simulation, but only at lower ripple pressures (Figure 5.27). At higher ripple pressures, weakening the strength model resulted in more recovered growth than in the experiment. Uncertainty in the drive modeled in

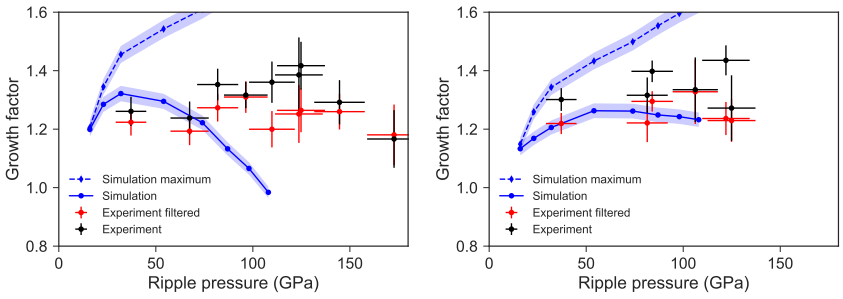

Figure 5.26: Recovered growth factors from tantalum samples with 2D (a) and 3D (b) initial perturbations compared to simulations using the $1/2 \times SG$ strength model.

CTH, possibly producing too little RMI growth at lower ripple pressures, is more likely the source of the disagreement between simulations and experiment than the strength model.

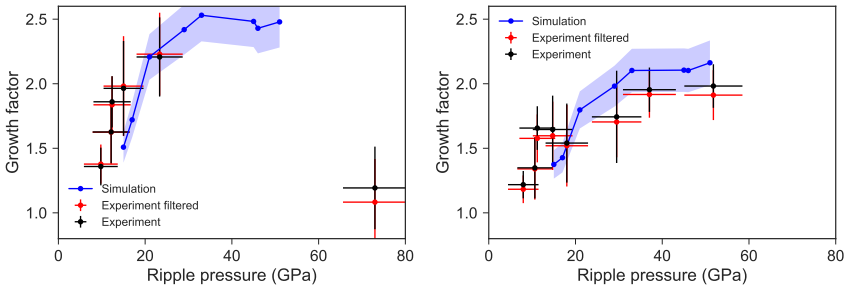

Figure 5.27: Recovered growth factors from copper samples with 2D (a) and 3D (b) initial perturbations compared to simulations using the $1/2 \times$ SG strength model.

One copper target with a 3D initial perturbation was driven from a preheated state, approximately 800 K. The increase in growth was on average 10 μm, but uncertainty increased significantly so that recovered growth factors from the preheated and ambient temperature shot results overlapped. This uncertainty made any inference about strength, beyond the observation that preheat weakened the sample, impossible.

Chapter 6

CONCLUSIONS

6.1 The effectiveness of recovery hydrodynamic instability experiments

Blast loading generated by laser ablation has been shown to load metallic samples above 10 GPa and drive hydrodynamic instabilities, producing strain rates in excess of 10^5 1/s. The loading did not destroy the robust recovery sample, but was sufficient to produce measurable perturbation growth.

The brevity of the blast loading limited the maximum recovered growth factor. In tantalum targets, recovered growth factors in the RMI-dominated regime did not exceed 1.4. Uncertainty in the recovered PTV complicated interpreting results. Small surface features contributed 1 to 2 μm to the PTV. As the maximum recovered growth was below 4 μm, this uncertainty made results difficult to interpret.

Larger recovered growth factor resulted in clearer trends when analyzing the CRF-copper results. However, producing loading waves in the range of ripple pressures where the CRF-copper targets grew required finer than normal control of the laser energy. Challenges in modeling shock compression of the CRF ablator complicated analysis of CRF-copper targets and hindered the comparison to simulation results.

Some issues cannot be solved without fundamentally changing the design of the experiment. The CRF ablator, which was difficult to simulate, was a necessity for preheated samples. A supported shock would have driven more RMI growth, but generating supported shocks with laser ablation requires consistent pulse shaping, which was not available at JLF.

Simulations of the CH-tantalum targets resulted in an unexpectedly important transition from increasing growth with ripple pressure to decreasing growth with ripple pressure. Attempting to maximize final growth factor by maximizing ripple pressure may not be effective for a given target. Future experiments would need to guarantee sufficiently low uncertainty, a growth range that is RMI-dominated, and a loading condition that can be simulated reliably.

6.2 Challenges of inferring strength from recovered samples

Experimentally recovered instability growth in tantalum was higher than predicted by simulations. Both 2D and 3D data sets could not be satisfied simultaneously

by altering the strength model of tantalum. Halving the strength model took the 2D simulation results further out of agreement with experiment, but marginally improved agreement with 3D simulation results. This disagreement was likely due to errors in modeling the loading conditions.

The $1 \times SG$ model for copper correctly predicted the recovered growth factor for high ripple pressure drives. Simulations did not agree with experimental results at low ripple pressure, possibly due to problems simulating the CRF ablator. One preheated copper sample grew more than an unheated copper sample driven with the same ripple pressure. However, the growth was nonuniform and could not be interpreted.

6.3 Future work

The target profiles, SEM images, and simulation results are a large catalog of information and more time could be spent in analysis. Current analysis could be improved and several avenues of analysis have not been pursued. Aspects of the experiment could be improved in order to generate better results.

Further study of the instability dynamics

The ripple pressures covered by simulations showed the existence of an RMI- and an RTI-dominated regime in CH-tantalum targets and only an RMI-dominated regime in CRF-copper targets. This description may only hold for the range of ripple pressure drives simulated. Simulations with strengthened models appear to show a low pressure limit to the RMI-dominated region, which is not understood (Figure 5.14(a)). The weakest ripple pressure drive in 3D CRF-copper simulations may show the same behavior, but it is within uncertainty (Figure 5.14(b)). The upper limit of the RMI-dominate regime in Figure 5.14(a) is also questionable. Higher ripple pressure drives would help show the full transition to RTI-dominated behavior and help compare the evolution of 2D to 3D initial perturbations.

Improvement of CRF drive simulation

The silica aerogel is not a perfect replacement for the CRF model. Finding a way to run simulations with the porous carbon EOS may improve agreement between simulation and experiment.

Numerical difficulties, even when using the silica EOS, caused issues at low ripple pressures. In 2D and 3D simulations, the shocked ablator was initialized from 1D results. Specifying the compaction parameter in the aerogel EOS resulted in

numerical errors at initial time. The erroneous state generated waves which briefly disrupted the shock. The shock mostly reformed as it traveled the final 50 μm before impacting the sample, but this disruption should be removed.

In the lowest ripple pressure simulation, an error from the silica aerogel EOS caused a local increase in pressure that deformed the surface of the copper sample. This pressure increase did not occur when using the same drive in a 2D simulation. Such errors set a lower bound on CRF-copper target simulations. Unfortunately, it is this ripple pressure range that is most relevant to the experimental results.

Interesting SEM features

SEM images of post-shot targets revealed interesting features not predicted by simulations. Radial variations in the loading pushed over perturbations, forming features that look like breaking waves (Figure 6.1). The waves appear at a certain radius from the shot center and then abruptly disappear after a few wavelengths.

An additional set of experiments with iron samples, using the same target design as the 2015 copper targets, showed an interesting change in surface features with preheat (Figure 6.2). The surface of the sample driven from ambient condition results in smooth peaks. When the sample is preheated, the peaks in the recovered target appear truncated like in the copper samples.

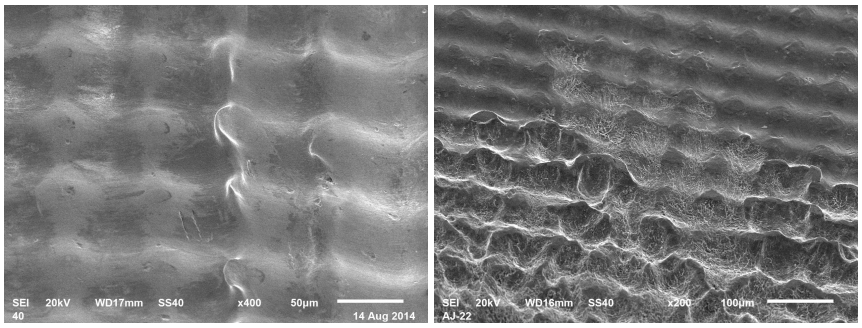

Figure 6.1: Interesting breaking wave SEM features at the edge of the shot area, from a 3D tantalum sample (a) and a 3D copper sample (b).

Additional preheated experiments

Time spent troubleshooting the preheating target mount reduced the number of preheated recovery shots. The one recovered preheated copper targets was too deformed to measure a growth factor with reasonable uncertainty. Additional preheating results would help bound the sensitivity of strength in copper to temperature.

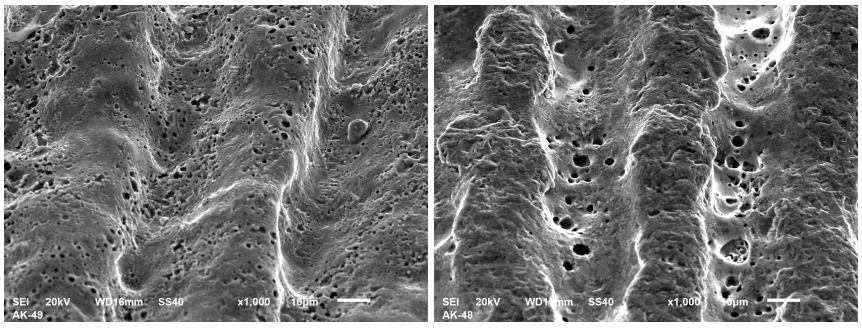

Figure 6.2: Change in peak shape of perturbations on iron samples driven with roughly the same ripple pressure with no preheat (a) and with preheat (b).

BIBLIOGRAPHY

[1] E. Asphaug, C. B. Agnor, and Q. Williams. "Hit-and-run planetary collisions". In: *Nature* 439.7073 (Jan. 2006), pp. 155–160. ISSN: 0028-0836. DOI: 10.1038/nature04311. URL: http://www.nature.com/nature/journal/v439/n7073/full/nature04311.html.

[2] E. Asphaug and H. J. Melosh. "The Stickney Impact of Phobos: A Dynamical Model". In: *Icarus* 101.1 (Jan. 1993), pp. 144–164. ISSN: 0019-1035. DOI: 10.1006/icar.1993.1012. URL: http://www.sciencedirect.com/science/article/pii/S0019103583710122.

[3] L. M. Barker and R. E. Hollenbach. "Laser interferometer for measuring high velocities of any reflecting surface". In: *Journal of Applied Physics* 43.11 (Nov. 1972), pp. 4669–4675. ISSN: 0021-8979, 1089-7550. DOI: 10.1063/1.1660986. URL: http://scitation.aip.org/content/aip/journal/jap/43/11/10.1063/1.1660986.

[4] J. F. Barnes et al. "Further experimentation on Taylor instability in solids". In: *Journal of Applied Physics* 51.9 (May 1980), pp. 4678–4679. ISSN: 0021-8979, 1089-7550. DOI: 10.1063/1.328339. URL: http://scitation.aip.org/content/aip/journal/jap/51/9/10.1063/1.328339.

[5] J. F. Barnes et al. "Taylor instability in solids". In: *Journal of Applied Physics* 45.2 (Aug. 1973), pp. 727–732. ISSN: 0021-8979, 1089-7550. DOI: 10.1063/1.1663310. URL: http://scitation.aip.org/content/aip/journal/jap/45/2/10.1063/1.1663310.

[6] N. R. Barton et al. "A multiscale strength model for extreme loading conditions". In: *Journal of Applied Physics* 109.7 (Apr. 2011), p. 073501. ISSN: 0021-8979, 1089-7550. DOI: 10.1063/1.3553718. URL: http://scitation.aip.org/content/aip/journal/jap/109/7/10.1063/1.3553718.

[7] B. I. Bennett et al. *Recent Developments in the Sesame Equation-of-State Library*. Tech. rep. LA-7130. Los Alamos Scientific Lab., N.Mex. (USA), Feb. 1978. URL: http://www.osti.gov/scitech/biblio/5150206.

[8] D. D. Bloomquist and S. A. Sheffield. "Optically recording interferometer for velocity measurements with subnanosecond resolution". In: *Journal of Applied Physics* 54.4 (Apr. 1983), pp. 1717–1722. ISSN: 0021-8979, 1089-7550. DOI: 10.1063/1.332222. URL: http://scitation.aip.org.clsproxy.library.caltech.edu/content/aip/journal/jap/54/4/10.1063/1.332222.

[9] E. M. Bringa et al. "Shock deformation of face-centred-cubic metals on subnanosecond timescales". In: *Nature Materials* 5.10 (Oct. 2006), pp. 805–809.

ISSN: 1476-1122. DOI: 10.1038/nmat1735. URL: http://www.nature.com/nmat/journal/v5/n10/abs/nmat1735.html.

[10] L. S. Bruesch and E. Asphaug. "Modeling global impact effects on middle-sized icy bodies: applications to Saturn's moons". In: *Icarus* 168.2 (Apr. 2004), pp. 457–466. ISSN: 0019-1035. DOI: 10.1016/j.icarus.2003.11.007. URL: http://www.sciencedirect.com/science/article/pii/S0019103503003890.

[11] W. T. Buttler et al. "Unstable Richtmyer–Meshkov growth of solid and liquid metals in vacuum". In: *Journal of Fluid Mechanics* 703 (2012), pp. 60–84. DOI: 10.1017/jfm.2012.190.

[12] A. G. W. Cameron and W. R. Ward. "The origin of the Moon". In: *Lunar and Planetary Science Conference*. Vol. 7. 1976, p. 120.

[13] R. M. Canup and E. Asphaug. "Origin of the Moon in a giant impact near the end of the Earth's formation". In: *Nature* 412.6848 (Aug. 2001), pp. 708–712. ISSN: 0028-0836. DOI: 10.1038/35089010. URL: http://www.nature.com/nature/journal/v412/n6848/abs/412708a0.html.

[14] P. M. Celliers et al. "Line-imaging velocimeter for shock diagnostics at the OMEGA laser facility". In: *Review of Scientific Instruments* 75.11 (Nov. 2004), pp. 4916–4929. ISSN: 0034-6748, 1089-7623. DOI: 10.1063/1.1807008. URL: http://scitation.aip.org/content/aip/journal/rsi/75/11/10.1063/1.1807008.

[15] P. R. Chapman and J. W. Jacobs. "Experiments on the three-dimensional incompressible Richtmyer-Meshkov instability". In: *Physics of Fluids (1994-present)* 18.7 (July 2006), p. 074101. ISSN: 1070-6631, 1089-7666. DOI: 10.1063/1.2214647. URL: http://scitation.aip.org/content/aip/journal/pof2/18/7/10.1063/1.2214647.

[16] R. J. Clifton. "Response of materials under dynamic loading". In: *International Journal of Solids and Structures* 37.1–2 (Jan. 2000), pp. 105–113. ISSN: 0020-7683. DOI: 10.1016/S0020-7683(99)00082-7. URL: http://www.sciencedirect.com/science/article/pii/S0020768399000827.

[17] G. S. Collins et al. "Hydrocode Simulations of Chicxulub Crater Collapse and Peak-Ring Formation". In: *Icarus* 157.1 (May 2002), pp. 24–33. ISSN: 0019-1035. DOI: 10.1006/icar.2002.6822. URL: http://www.sciencedirect.com/science/article/pii/S0019103502968223.

[18] J. D. Colvin et al. "A model for instability growth in accelerated solid metals". In: *Journal of Applied Physics* 93.9 (Apr. 2003), pp. 5287–5301. ISSN: 0021-8979, 1089-7550. DOI: 10.1063/1.1565188. URL: http://scitation.aip.org/content/aip/journal/jap/93/9/10.1063/1.1565188.

[19] R. Courant and K. O. Friedrichs. *Supersonic flow and shock waves*. Vol. 21. Springer Science & Business Media, 1999.

[20] L. Davison and R. A Graham. “Shock compression of solids”. In: *Physics Reports* 55.4 (Oct. 1979), pp. 255–379. ISSN: 0370-1573. DOI: 10.1016/0370-1573(79)90026-7. URL: http://www.sciencedirect.com/science/article/pii/0370157379900267.

[21] G. Dimonte, R. Gore, and M. Schneider. “Rayleigh-Taylor Instability in Elastic-Plastic Materials”. In: *Physical Review Letters* 80.6 (Feb. 1998), pp. 1212–1215. DOI: 10.1103/PhysRevLett.80.1212. URL: http://link.aps.org/doi/10.1103/PhysRevLett.80.1212.

[22] G. Dimonte et al. “Use of the Richtmyer-Meshkov Instability to Infer Yield Stress at High-Energy Densities”. In: *Physical Review Letters* 107.26 (Dec. 2011), p. 264502. DOI: 10.1103/PhysRevLett.107.264502. URL: http://link.aps.org/doi/10.1103/PhysRevLett.107.264502.

[23] D. H. Dolan. *Foundations of VISAR analysis*. Sandia National Laboratories, 2006.

[24] K. E. Duprey and R. J. Clifton. “Dynamic Constitutive Response of Tantalum at High Strain Rates”. In: *AIP Conference Proceedings* 429.1 (July 1998). ISSN: 0094-243X. DOI: 10.1063/1.55661. URL: http://www.osti.gov/scitech/biblio/21185649.

[25] J. E. Field et al. “Review of experimental techniques for high rate deformation and shock studies”. In: *International Journal of Impact Engineering* 30.7 (2004), pp. 725–775.

[26] P. S. Follansbee and G. T. Gray. “Dynamic deformation of shock prestrained copper”. In: *Materials Science and Engineering: A* 138.1 (May 1991), pp. 23–31. ISSN: 0921-5093. DOI: 10.1016/0921-5093(91)90673-B. URL: http://www.sciencedirect.com/science/article/pii/092150939190673B.

[27] C. A. Forest. “Isentrope energy, Hugoniot temperature, and the Mie-Gruneisen equation of state”. In: *AIP Conference Proceedings*. Vol. 370. AIP Publishing, May 1996, pp. 31–34. DOI: 10.1063/1.50715. URL: http://scitation.aip.org/content/aip/proceeding/aipcp/10.1063/1.50715.

[28] K. J. Frutschy and R. J. Clifton. “High-temperature pressure-shear plate impact experiments on OFHC copper”. In: *Journal of the Mechanics and Physics of Solids* 46.10 (Oct. 1998), pp. 1723–1744. ISSN: 0022-5096. DOI: 10.1016/S0022-5096(98)00055-6. URL: http://www.sciencedirect.com/science/article/pii/S0022509698000556.

[29] B. A. Gama, S. L. Lopatnikov, and J. W. Jr. Gillespie. “Hopkinson bar experimental technique: A critical review”. In: *Applied Mechanics Reviews* 57.4 (Oct. 2004), pp. 223–250. ISSN: 0003-6900. DOI: 10.1115/1.1704626. URL: http://dx.doi.org/10.1115/1.1704626.

[30] V. N. Goncharov. “Analytical Model of Nonlinear, Single-Mode, Classical Rayleigh-Taylor Instability at Arbitrary Atwood Numbers”. In: *Physical Review Letters* 88.13 (Mar. 2002), p. 134502. DOI: 10.1103/PhysRevLett.88.134502. URL: http://link.aps.org/doi/10.1103/PhysRevLett.88.134502.

[31] G. T. Gray. “Shock Wave Testing of Ductile Materials.” In: *Materials Park, OH: ASM International, 2000.* (2000), pp. 530–538.

[32] W. K. Hartmann and D. R. Davis. “Satellite-sized planetesimals and lunar origin”. In: *Icarus* 24.4 (Apr. 1975), pp. 504–515. ISSN: 0019-1035. DOI: 10.1016/0019-1035(75)90070-6. URL: http://www.sciencedirect.com/science/article/pii/0019103575900706.

[33] W. Herrmann. “Constitutive Equation for the Dynamic Compaction of Ductile Porous Materials”. In: *Journal of Applied Physics* 40.6 (May 1969), pp. 2490–2499. ISSN: 0021-8979, 1089-7550. DOI: 10.1063/1.1658021. URL: http://scitation.aip.org/content/aip/journal/jap/40/6/10.1063/1.1658021.

[34] R. L. Hilliard and G. G. Shepherd. “Wide-Angle Michelson Interferometer for Measuring Doppler Line Widths*”. In: *Journal of the Optical Society of America* 56.3 (Mar. 1966), p. 362. ISSN: 0030-3941. DOI: 10.1364/JOSA.56.000362. URL: https://www.osapublishing.org/abstract.cfm?URI=josa-56-3-362.

[35] K. G. Hoge and A. K. Mukherjee. “The temperature and strain rate dependence of the flow stress of tantalum”. In: *Journal of Materials Science* 12.8 (Aug. 1977), pp. 1666–1672. ISSN: 0022-2461, 1573-4803. DOI: 10.1007/BF00542818. URL: http://link.springer.com/article/10.1007/BF00542818.

[36] A. K. Hopkins and P. C. Chou. *Dynamic Response of Materials to Intense Impulsive Loading*. Tech. rep. Aug. 1972.

[37] B. A. Ivanov, D. Deniem, and G. Neukum. “Implementation of dynamic strength models into 2D hydrocodes: Applications for atmospheric breakup and impact cratering”. In: *International Journal of Impact Engineering*. Hypervelocity Impact Proceedings of the 1996 Symposium 20.1–5 (1997), pp. 411–430. ISSN: 0734-743X. DOI: 10.1016/S0734-743X(97)87511-2. URL: http://www.sciencedirect.com/science/article/pii/S0734743X97875112.

[38] J. W. Jacobs and I. Catton. “Three-dimensional Rayleigh-Taylor instability Part 1. Weakly nonlinear theory”. In: *Journal of Fluid Mechanics* 187 (Feb. 1988), pp. 329–352. ISSN: 1469-7645. DOI: 10.1017/S002211208800045X. URL: http://journals.cambridge.org/article_S002211208800045X.

[39] J. W. Jacobs and I. Catton. "Three-dimensional Rayleigh-Taylor instability Part 2. Experiment". In: *Journal of Fluid Mechanics* 187 (Feb. 1988), pp. 353–371. ISSN: 1469-7645. DOI: 10.1017/S0022112088000461. URL: http://journals.cambridge.org/article_S0022112088000461.

[40] D. H. Kalantar et al. "Solid-state experiments at high pressure and strain rate". In: *Physics of Plasmas (1994-present)* 7.5 (May 2000), pp. 1999–2006. ISSN: 1070-664X, 1089-7674. DOI: 10.1063/1.874021. URL: http://scitation.aip.org/content/aip/journal/pop/7/5/10.1063/1.874021.

[41] R. G. Kraus. Personal communication. 2013.

[42] H. J. Kull. "Theory of the Rayleigh-Taylor instability". In: *Physics Reports* 206.5 (Aug. 1991), pp. 197–325. ISSN: 0370-1573. DOI: 10.1016/0370-1573(91)90153-D. URL: http://www.sciencedirect.com/science/article/pii/037015739190153D.

[43] A. Kumar and R. G. Kumble. "Viscous Drag on Dislocations at High Strain Rates in Copper". In: *Journal of Applied Physics* 40.9 (Aug. 1969), pp. 3475–3480. ISSN: 0021-8979, 1089-7550. DOI: 10.1063/1.1658222. URL: http://scitation.aip.org.clsproxy.library.caltech.edu/content/aip/journal/jap/40/9/10.1063/1.1658222.

[44] J. T. Larsen. Personal communication. 2015.

[45] J. T. Larsen and S. M. Lane. "HYADES — A plasma hydrodynamics code for dense plasma studies". In: *Journal of Quantitative Spectroscopy and Radiative Transfer* 51.1–2 (Jan. 1994), pp. 179–186. ISSN: 0022-4073. DOI: 10.1016/0022-4073(94)90078-7. URL: http://www.sciencedirect.com/science/article/pii/0022407394900787.

[46] A. I. Lebedev, P. N. Nisovtsev, and V. A. Rayevsky. "Rayleigh-Taylor instability in solids". In: *Proceedings of the 4th International Workshop on the Physics of Compressible Turbulent Mixing* (Mar. 1993), p. 81.

[47] J. Lindl. "Development of the indirect-drive approach to inertial confinement fusion and the target physics basis for ignition and gain". In: *Physics of Plasmas (1994-present)* 2.11 (Nov. 1995), pp. 3933–4024. ISSN: 1070-664X, 1089-7674. DOI: 10.1063/1.871025. URL: http://scitation.aip.org/content/aip/journal/pop/2/11/10.1063/1.871025.

[48] W. M. Manheimer, D. G. Colombant, and J. H. Gardner. *Steady-State Planar Ablative Flow*. Tech. rep. Nov. 1981.

[49] M. M. Marinak et al. "Three-Dimensional Single Mode Rayleigh-Taylor Experiments on Nova". In: *Physical Review Letters* 75.20 (Nov. 1995), pp. 3677–3680. DOI: 10.1103/PhysRevLett.75.3677. URL: http://link.aps.org/doi/10.1103/PhysRevLett.75.3677.

[50] J. M. McGlaun, S. L. Thompson, and M. G. Elrick. "CTH: A three-dimensional shock wave physics code". In: *International Journal of Impact Engineering* 10.1 (Jan. 1990), pp. 351–360. ISSN: 0734-743X. DOI: 10.1016/0734-743X(90)90071-3. URL: http://www.sciencedirect.com/science/article/pii/0734743X90900713.

[51] R. Menikoff. "Complete Mie-Gruneisen Equation of State". In: *Chem. Phys* 113 (2000), pp. 7492–7501.

[52] R. Menikoff. "Empirical equations of state for solids". In: *Shock Wave Science and Technology Reference Library*. Springer, 2007, pp. 143–188.

[53] R. Menikoff and B. J. Plohr. "The Riemann problem for fluid flow of real materials". In: *Reviews of Modern Physics* 61.1 (Jan. 1989), pp. 75–130. DOI: 10.1103/RevModPhys.61.75. URL: http://link.aps.org/doi/10.1103/RevModPhys.61.75.

[54] E. E. Meshkov. "Instability of the interface of two gases accelerated by a shock wave". In: *Fluid Dynamics* 4.5 (1969), pp. 101–104. ISSN: 0015-4628, 1573-8507. DOI: 10.1007/BF01015969. URL: http://link.springer.com/article/10.1007/BF01015969.

[55] K. A. Meyer and P. J. Blewett. "Numerical Investigation of the Stability of a Shock-Accelerated Interface between Two Fluids". In: *Physics of Fluids (1958-1988)* 15.5 (May 1972), pp. 753–759. ISSN: 0031-9171. DOI: 10.1063/1.1693980. URL: http://scitation.aip.org.clsproxy.library.caltech.edu/content/aip/journal/pof1/15/5/10.1063/1.1693980.

[56] M. A. Meyers. *Dynamic Behavior of Materials*. John Wiley & Sons, Oct. 1994. ISBN: 978-0-471-58262-5.

[57] M. A. Meyers et al. "High-strain, high-strain-rate behavior of tantalum". In: *Metallurgical and Materials Transactions A* 26.10 (Oct. 1995), pp. 2493–2501. ISSN: 1073-5623, 1543-1940. DOI: 10.1007/BF02669407. URL: http://link.springer.com/article/10.1007/BF02669407.

[58] M. A. Meyers et al. "Laser-induced shock compression of monocrystalline copper: characterization and analysis". In: *Acta Materialia* 51.5 (Mar. 2003), pp. 1211–1228. ISSN: 1359-6454. DOI: 10.1016/S1359-6454(02)00420-2. URL: http://www.sciencedirect.com/science/article/pii/S1359645402004202.

[59] K. O. Mikaelian. "Design of a Rayleigh–Taylor experiment to measure strength at high pressures". In: *Physics of Plasmas (1994-present)* 17.9 (Sept. 2010), p. 092701. ISSN: 1070-664X, 1089-7674. DOI: 10.1063/1.3478987. URL: http://scitation.aip.org/content/aip/journal/pop/17/9/10.1063/1.3478987.

[60] K. O. Mikaelian. “Growth rate of the Richtmyer-Meshkov instability at shocked interfaces”. In: *Physical Review Letters* 71.18 (Nov. 1993), pp. 2903–2906. DOI: 10.1103/PhysRevLett.71.2903. URL: http://link.aps.org/doi/10.1103/PhysRevLett.71.2903.

[61] K. O. Mikaelian. “Shock-induced interface instability in viscous fluids and metals”. In: *Physical Review E* 87.3 (Mar. 2013), p. 031003. DOI: 10.1103/PhysRevE.87.031003. URL: http://link.aps.org/doi/10.1103/PhysRevE.87.031003.

[62] W. J. Murphy et al. “The strength of single crystal copper under uniaxial shock compression at 100 GPa”. In: *Journal of Physics: Condensed Matter* 22.6 (2010), p. 065404. ISSN: 0953-8984. DOI: 10.1088/0953-8984/22/6/065404. URL: http://stacks.iop.org/0953-8984/22/i=6/a=065404.

[63] H.-S. Park et al. “Grain-Size-Independent Plastic Flow at Ultrahigh Pressures and Strain Rates”. In: *Physical Review Letters* 114.6 (Feb. 2015), p. 065502. DOI: 10.1103/PhysRevLett.114.065502. URL: http://link.aps.org/doi/10.1103/PhysRevLett.114.065502.

[64] H.-S. Park et al. “Strong stabilization of the Rayleigh–Taylor instability by material strength at megabar pressures”. In: *Physics of Plasmas* 17.5 (May 2010), p. 056314. ISSN: 1070-664X, 1089-7674. DOI: 10.1063/1.3363170. URL: http://scitation.aip.org.clsproxy.library.caltech.edu/content/aip/journal/pop/17/5/10.1063/1.3363170.

[65] H.-S. Park et al. “Viscous Rayleigh-Taylor Instability Experiments at High Pressure and Strain Rate”. In: *Physical Review Letters* 104.13 (Apr. 2010), p. 135504. DOI: 10.1103/PhysRevLett.104.135504. URL: http://link.aps.org/doi/10.1103/PhysRevLett.104.135504.

[66] A. R. Piriz et al. “Rayleigh-Taylor instability in elastic solids”. In: *Physical Review E* 72.5 (Nov. 2005), p. 056313. DOI: 10.1103/PhysRevE.72.056313. URL: http://link.aps.org/doi/10.1103/PhysRevE.72.056313.

[67] A. R. Piriz et al. “Richtmyer-Meshkov instability in elastic-plastic media”. In: *Physical Review E* 78.5 (Nov. 2008), p. 056401. DOI: 10.1103/PhysRevE.78.056401. URL: http://link.aps.org/doi/10.1103/PhysRevE.78.056401.

[68] D. L. Preston, D. L. Tonks, and D. C. Wallace. “Model of plastic deformation for extreme loading conditions”. In: *Journal of Applied Physics* 93.1 (Jan. 2003), pp. 211–220. ISSN: 0021-8979, 1089-7550. DOI: 10.1063/1.1524706. URL: http://scitation.aip.org/content/aip/journal/jap/93/1/10.1063/1.1524706.

[69] M. B. Prime et al. “Using Richtmyer–Meshkov Instabilities to Estimate Metal Strength at Very High Rates”. In: *Dynamic Behavior of Materials, Volume 1*. Ed. by B. Song et al. Conference Proceedings of the Society for Experimental Mechanics Series. DOI: 10.1007/978-3-319-22452-7_27. Springer International Publishing, 2016, pp. 191–197. ISBN: 978-3-319-22451-0 978-3-319-22452-7. URL: http://link.springer.com/chapter/10.1007/978-3-319-22452-7_27.

[70] G. C. Randall et al. “Developments in Microcoining Rippled Metal Foils”. In: *Fusion Science and Technology* 63.2 (Mar. 2013), pp. 274–281. URL: http://epubs.ans.org/?a=16350.

[71] G. Regazzoni, U. F. Kocks, and P. S. Follansbee. “Dislocation kinetics at high strain rates”. In: *Acta Metallurgica* 35.12 (Dec. 1987), pp. 2865–2875. ISSN: 0001-6160. DOI: 10.1016/0001-6160(87)90285-9. URL: http://www.sciencedirect.com/science/article/pii/0001616087902859.

[72] B. A. Remington et al. “Material dynamics under extreme conditions of pressure and strain rate”. In: *Materials Science and Technology* 22.4 (Apr. 2006), pp. 474–488. ISSN: 0267-0836. DOI: 10.1179/174328406X91069. URL: http://www.maneyonline.com/doi/abs/10.1179/174328406X91069.

[73] B. A. Remington et al. “Materials science under extreme conditions of pressure and strain rate”. In: *Metallurgical and Materials Transactions A* 35.9 (Sept. 2004), pp. 2587–2607. ISSN: 1073-5623, 1543-1940. DOI: 10.1007/s11661-004-0205-6. URL: http://link.springer.com/article/10.1007/s11661-004-0205-6.

[74] M. H. Rice, R. G. McQueen, and J. M. Walsh. “Compression of solids by strong shock waves”. In: *Solid state physics* 6 (1958), pp. 1–63.

[75] R. D. Richtmyer. “Taylor instability in shock acceleration of compressible fluids”. In: *Communications on Pure and Applied Mathematics* 13.2 (1960), pp. 297–319. ISSN: 1097-0312. DOI: 10.1002/cpa.3160130207. URL: http://onlinelibrary.wiley.com/doi/10.1002/cpa.3160130207/abstract.

[76] D. Rittel et al. “Thermomechanical behavior of single crystalline tantalum in the static and dynamic regime”. In: *Mechanics of Materials* 41.12 (Dec. 2009), pp. 1323–1329. ISSN: 0167-6636. DOI: 10.1016/j.mechmat.2009.08.001. URL: http://www.sciencedirect.com/science/article/pii/S0167663609001318.

[77] D. Rittel et al. “Thermomechanical characterization of pure polycrystalline tantalum”. In: *Materials Science and Engineering: A* 447.1–2 (Feb. 2007), pp. 65–70. ISSN: 0921-5093. DOI: 10.1016/j.msea.2006.10.064. URL: http://www.sciencedirect.com/science/article/pii/S0921509306021812.

[78] L. E. Senft and S. T. Stewart. "Modeling impact cratering in layered surfaces". In: *Journal of Geophysical Research: Planets* 112.E11 (Nov. 2007), E11002. ISSN: 2156-2202. DOI: 10.1029/2007JE002894. URL: http://onlinelibrary.wiley.com/doi/10.1029/2007JE002894/abstract.

[79] D. J. Steinberg. *Equation of state and strength properties of selected materials*. Tech. rep. UCRL-MA-106439 (change 1). Lawrence Livermore National Laboratory, CA (USA), 1996.

[80] D. J. Steinberg, S. G. Cochran, and M. W. Guinan. "A constitutive model for metals applicable at high-strain rate". In: *Journal of Applied Physics* 51.3 (1980), pp. 1498–1504. ISSN: 0021-8979, 1089-7550. DOI: 10.1063/1.327799. URL: http://scitation.aip.org/content/aip/journal/jap/51/3/10.1063/1.327799.

[81] D. J. Steinberg and C. M. Lund. "A constitutive model for strain rates from 10^{-4} to 10^{6} s^{-1}". In: *Journal of Applied Physics* 65.4 (Feb. 1989), pp. 1528–1533. ISSN: 0021-8979, 1089-7550. DOI: 10.1063/1.342968. URL: http://scitation.aip.org/content/aip/journal/jap/65/4/10.1063/1.342968.

[82] J. W. Swegle and D. E. Grady. "Shock viscosity and the prediction of shock wave rise times". In: *Journal of Applied Physics* 58.2 (July 1985), pp. 692–701. ISSN: 0021-8979, 1089-7550. DOI: 10.1063/1.336184. URL: http://scitation.aip.org/content/aip/journal/jap/58/2/10.1063/1.336184.

[83] D. C. Swift and R. G. Kraus. "Properties of plastic ablators in laser-driven material dynamics experiments". In: *Physical Review E* 77.6 (June 2008), p. 066402. DOI: 10.1103/PhysRevE.77.066402. URL: http://link.aps.org/doi/10.1103/PhysRevE.77.066402.

[84] M. Takeda, H. Ina, and S. Kobayashi. "Fourier-transform method of fringe-pattern analysis for computer-based topography and interferometry". In: *Journal of the Optical Society of America* 72.1 (Jan. 1982), p. 156. ISSN: 0030-3941. DOI: 10.1364/JOSA.72.000156. URL: https://www.osapublishing.org/abstract.cfm?URI=josa-72-1-156.

[85] G. Taylor. "The Instability of Liquid Surfaces when Accelerated in a Direction Perpendicular to their Planes. I". In: *Proceedings of the Royal Society of London A: Mathematical, Physical and Engineering Sciences* 201.1065 (Mar. 1950), pp. 192–196. ISSN: 1364-5021, 1471-2946. DOI: 10.1098/rspa.1950.0052. URL: http://rspa.royalsocietypublishing.org/content/201/1065/192.

[86] W. Tong. "Pressure-shear stress wave analysis in plate impact experiments". In: *International journal of impact engineering* 19.2 (1997), pp. 147–164.

[87] W. Tong, R. J. Clifton, and S. Huang. "Pressure-shear impact investigation of strain rate history effects in oxygen-free high-conductivity copper". In: *Journal of the Mechanics and Physics of Solids* 40.6 (Aug. 1992), pp. 1251–1294. ISSN: 0022-5096. DOI: 10.1016/0022-5096(92)90015-T. URL: http://www.sciencedirect.com/science/article/pii/002250969290015T.

[88] J. T. Waddell, C. E. Niederhaus, and J. W. Jacobs. "Experimental study of Rayleigh–Taylor instability: Low Atwood number liquid systems with single-mode initial perturbations". In: *Physics of Fluids (1994-present)* 13.5 (May 2001), pp. 1263–1273. ISSN: 1070-6631, 1089-7666. DOI: 10.1063/1.1359762. URL: http://scitation.aip.org.clsproxy.library.caltech.edu/content/aip/journal/pof2/13/5/10.1063/1.1359762.

[89] D. C. Wallace. "Irreversible thermodynamics of overdriven shocks in solids". In: *Physical Review B* 24.10 (Nov. 1981), pp. 5597–5606. DOI: 10.1103/PhysRevB.24.5597. URL: http://link.aps.org/doi/10.1103/PhysRevB.24.5597.

[90] D. C. Wallace. "Nature of the process of overdriven shocks in metals". In: *Physical Review B* 24.10 (Nov. 1981), pp. 5607–5615. DOI: 10.1103/PhysRevB.24.5607. URL: http://link.aps.org/doi/10.1103/PhysRevB.24.5607.

[91] J. P. Wilkinson and J. W. Jacobs. "Experimental study of the single-mode three-dimensional Rayleigh-Taylor instability". In: *Physics of Fluids (1994-present)* 19.12 (2007), p. 124102.

[92] Ya. B. Zeldovich and Yu. P. Raizer. *Physics of shock waves and high-temperature hydrodynamic phenomena*. Ed. by W. D. Hayes and R. F. Probstein. 1965.

[93] F. J. Zerilli and R. W. Armstrong. "Dislocation-mechanics-based constitutive relations for material dynamics calculations". In: *Journal of Applied Physics* 61.5 (Mar. 1987), pp. 1816–1825. ISSN: 0021-8979, 1089-7550. DOI: 10.1063/1.338024. URL: http://scitation.aip.org/content/aip/journal/jap/61/5/10.1063/1.338024.

Appendix A

HYADES TARGET MESHING AND CONVERGENCE

A.1 Hyades mesh solver

The Hyades mesh points are referred to by mesh indices and the point between mesh points is referred to by zone indices. Indices start at 1. There is always one fewer zone point than mesh point. The location of a mesh point is given by x_j and the width of zone bordered by mesh points x_j and x_{j+1} is Δx_j, shown in Figure A.1.

State variables are assigned to either mesh points or zone points. For example, density, pressure, and temperature are zone properties while velocity is a mesh property. State variables will be referred to as ρ_j, p_j, T_j, and u_j, the density, pressure, temperature, and velocity respectively, where j is either the mesh index or the zone index. It is also useful to refer to m_j, the mass of zone j, where $m_j = \rho_j \Delta x_j$.

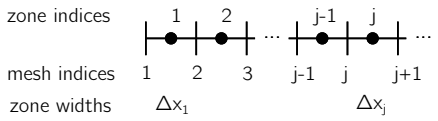

Figure A.1: Hyades mesh convention for naming mesh indices, zone indices, and describing the zone widths.

The geometry is divided into mesh sections with one of two types of mesh. The first is a constant mesh section, where the distance between mesh points is equal, Δx_j = constant. The second is a feathered mesh section, where the distance between the mesh points increases or decreases geometrically. Here, $\Delta x_j = r \Delta x_{j-1}$, where r is a ratio defining the expansion or contraction of zone widths. $r > 1$ spaces mesh points farther apart. If $r = 1$, then the feather mesh section is the same as a constant mesh section.

Goals of the solver

A good mesh is constrained by several conditions.

1. The maximum number of mesh points is 1999 and the maximum number of zones in 1998. This is a limit imposed by Hyades.

2. The mass per zone, $m_j = \rho \Delta x_j$, should be matched across mesh sections [44].

3. Assuming the laser strikes zone $j = 1$, $\Delta x_1 \sim 10^{-10}$ m to capture the laser-matter interaction accurately [41].

4. Expansion and contraction ratios should be less than 5% [83].

5. Zone widths should not exceed a certain length in order to accurately capture a shock. Mesh convergence studies show resolutions of < 1 μm/zone are sufficient, Section A.4.

As an example, start with a 250 μm polystyrene ablator attached to a 250 μm tantalum sample, shown in Figure A.2. A laser strikes zone 1. The first zones in the ablator should be approximately 1 Å wide. However, the sample is too large for the entire mesh to be this dense. A fraction of the CH is meshed by a feather mesh section with $r > 1$, so that Δx_j increases as j increases. This increase also causes m_j to rise. Once Δx_j increases to a reasonable values, a constant mesh section is used. This spacing cannot be maintained across the ablator-sample interface, because the change in density will cause a discontinuity in mass per zone. A second feather mesh section is used to match m in the ablator to m in the sample.

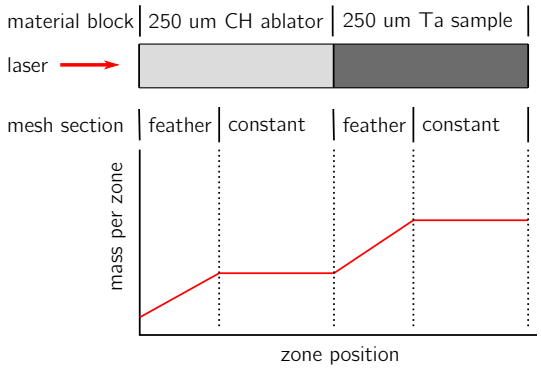

Figure A.2: A sample geometry split into constant and feather mesh sections. A desirable mass per zone profile is sketched below the geometry.

Solver procedure

A few assumptions are imposed on the mesh. First, the mesh is divided into *material blocks*, contiguous regions of the mesh that are assigned to the same material. Each material block is split into two *mesh sections*: a feathered section and a constant section. The feathered section will always come before the constant mesh section.

Let a superscript i indicate the i^{th} material block in the mesh and let a superscript $\star^{\text{F}_i}$ and $\star^{\text{C}_i}$ indicate a feathered and constant mesh section of material block i.

Each mesh section is defined by its own local numbering system from 1 to the total number of points in the mesh section, n. For example, $x_n^{\mathrm{F}_1}$ is the final mesh point in the feathered mesh section of material block 1. For a typical geometry, $i = 1$ is the ablator and $i = 2$ is the sample. A general material block i is labeled in Figure A.3.

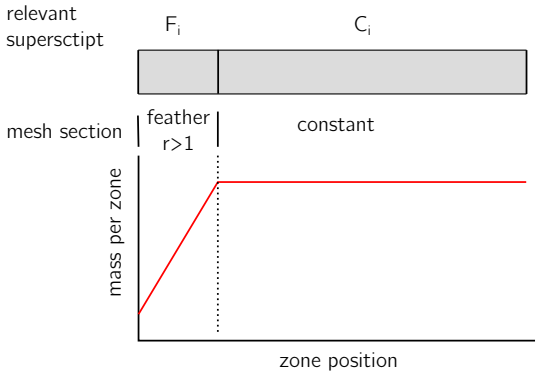

Figure A.3: An example region, i, with a feathered and a constant mesh section. The zone size increases in the feather.

As a first approximation of the meshing, the feathered regions are ignored and the mesh points are distributed so that each $w^{\mathrm{C}_i}\Delta x^{\mathrm{C}_i}$ is equal, where w^{C_i} is a weighting factor that allows some constant sections to receive a finer or coarser mesh than others. This step will satisfy goal 5 if the initial number of mesh points is sufficient. However, if the material blocks have different density, each constant mesh section will have a different mass per zone, in violation of goal 2. The feathered mesh sections are used to match the mass per zone difference.

Each material block receives a ρ^i through its material assignment. The feathered mesh section within material block i is defined by r^{F_i}, L^{F_i}, and n^{F_i}. In the feathered mesh section, these properties are related to each other by two equations. First, the zone widths are related by r. Only considering $\star^{\mathrm{F}_i}$ so the superscript is not shown,

$$\Delta x_1 r = \Delta x_2 \tag{A.1}$$

$$\Delta x_1 r^{(\bar{j}-1)} = \Delta x_{\bar{j}}, \tag{A.2}$$

which relates the first and any following zone widths in a feathered mesh section. This relation can also be used to write the length of feathered mesh section as the sum of all zone widths,

$$L = \Delta x_1 + (\Delta x_1)r + ((\Delta x_1 r)r)r + \ldots \tag{A.3}$$

$$= \Delta x_1(1 + r + r^2 + \ldots) \tag{A.4}$$

$$= \Delta x_1 \sum_{j=0}^{n-1} r^j \tag{A.5}$$

$$= \frac{\Delta x_1 \left(r^n - 1\right)}{r - 1}. \tag{A.6}$$

Together with a specified feathered mesh section length L, we have relations for the set of unknowns r, n, and Δx_1, so one more is needed.

Another condition on the feather is that it must match the mass per zone on its left and right boundaries. $i = 1$ is the trivial case where $\Delta x_1^{\mathrm{F}_1} = 1$ Å by goal 3. In this case, $\Delta x_n^{\mathrm{F}_1} = \Delta x_1^{\mathrm{C}_1}$ by goal 2. The mass condition reduces to a zone width condition because both mesh sections are part of material block 1 and share the same density. $\Delta x_1^{\mathrm{C}_1}$ is determined from the original even distribution of points, so r^{F_1} can be calculated from Equation A.2. Then n^{F_1} can be calculated from Equation A.6.

It is less simple to solve for the properties of $\star^{\mathrm{F}_2}$. There are two mass match conditions. The first comes from Δx^{C_2} which is known. The second comes from m^{C_1}. The final wrinkle is that each r may not fall in the range $0.95 < r < 1.05$, as recommended by [83]. The method must be iterated until this conditions is satisfied.

A.2 Recovery target simulation meshes

The variation in dimensions between CH-tantalum and CRF-copper targets meant a single drive target mesh could not be used. However, each target used a similar meshing scheme. The ablator was meshed with a 50 μm feather, followed by a constant section for the remaining length of the ablator. The transition between the ablator and the sample is handled by a 10 μm feather. The following length of the sample, up to 40 μm, uses a constant mesh. To prevent reflections from the end of the window before the end of the simulation, the sample mesh is extended with a 100 μm long feather leading to a 50 μm long constant section with a 0.1 weighting, forcing a very coarse mesh as the accuracy of the results over 50 μm beyond the ablator-sample interface is unimportant.

For example, the mesh used for the CH-tantalum recovery targets is plotted in Figure A.4. Jumps in zone widths correspond to changes in material. Constant mesh sections in the ablator (-170 μm to 0 μm) and the sample (10 μm to 50 μm) used the same weight and have the same zone width as a result.

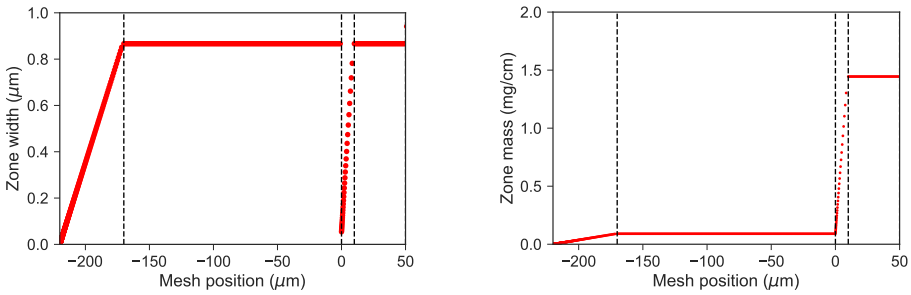

(a) (b)

Figure A.4: Plots of the zone width (a) and zone mass (b). Dotted lines divide mesh sections. The ablator-sample interface is at position 0 μm.

A.3 Drive target simulation meshes

The drive target ablators were meshed in the same way as the recovery target ablators. If a window is used, the mesh weighting in the sample is set to 5 to force a denser mesh in the sample and decrease the mass per zone in the sample. This weighting reduces the feather ratio needed to match mass per zone over the sample-window interface. The window is meshed with a 15 μm feather leading to a 5 μm constant region. The window is extended in the same way as the sample in the recovery targets.

For example, the mesh used for the flat CH-tantalum drive targets is plotted in Figure A.5. The small zone widths used to mesh the sample (0 μm to 15 μm) were forced with a higher weight. Only a small section of the coarse zones used to mesh the majority of the window are shown.

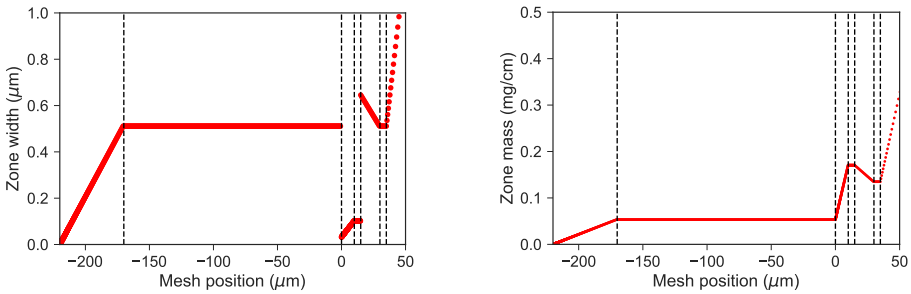

(a) (b)

Figure A.5: Plots of the zone width (a) and zone mass (b). Dotted lines divide mesh sections. The ablator-sample interface is at position 0 μm.

A.4 Recovery target mesh convergence studies

Mesh convergence studies were conducted over the CH-tantalum and CRF-copper recovery target geometries. In both cases, the bulk pressure, the pressure averaged between points 1 μm and 10 μm into the sample, and the bulk velocity were calculated. The maximum bulk quantity was calculated and compared between mesh resolutions (Figure A.6). The laser source, a 120 J pulse for the CH-tantalum targets and a 20 J pulse for the CRF-copper targets, was selected to be a representative loading, roughly in the middle of loadings used in experiments.

Even at the lowest mesh resolution, incremental changes in mesh resolution of the CH-tantalum targets did not change the maximum bulk pressure and velocity significantly. Any mesh resolution less than 1 μm/zone was sufficient in the constant regions. The CRF-copper simulations converged similarly, with a resolution of 1 μm/zone in the constant region sufficient for incremental changes in maximum bulk pressure of $< 1\%$. To satisfy this study, all simulations used a constant region mesh resolution of < 1.0 μm/zone.

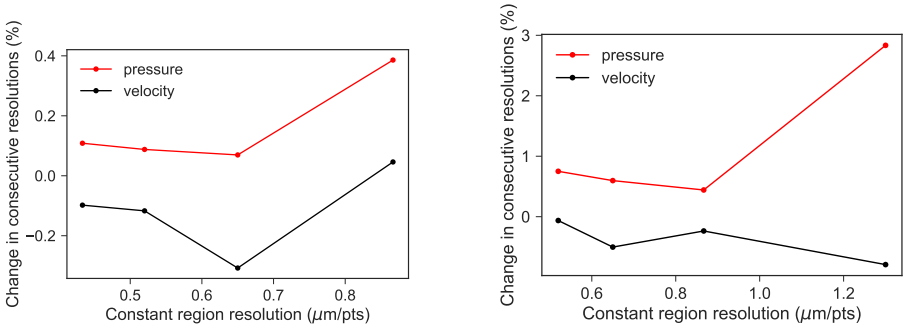

(a) (b)

Figure A.6: Mesh convergence study for a CH-tantalum recovery target (a) and a CRF-copper recovery target (b).

Appendix B

CTH TARGET MESHING AND CONVERGENCE

B.1 Convergence of energy source mesh

The meshing scheme in Figure 4.11 was used to simulate a 1D energy source loading for a range of mesh resolutions. The mesh resolution was varied by setting the mesh resolution in the constant section. Increasing the mesh resolution in the constant section also increased resolution in the expanding and contracting mesh sections as the zone width was matched across mesh sections.

Mesh convergence was studied in the tantalum targets using a 30 J energy source and in the copper targets using a 10 J energy source. Mesh convergence was tested by comparing the maximum bulk pressure, temperature, density, and particle velocity (Figure B.1). The polystyrene ablator in the tantalum targets converged rapidly. A resolution of 0.075 μm/zone was sufficient to keep peak state changes under 5% when adding 1,000 additional zones. The CRF ablator in the copper targets converged much more slowly. The peak state continually oscillated 5% when adding 1,000 additional zones. A resolution of 4,000 zones was selected for tantalum targets and 8,000 zones for copper targets.

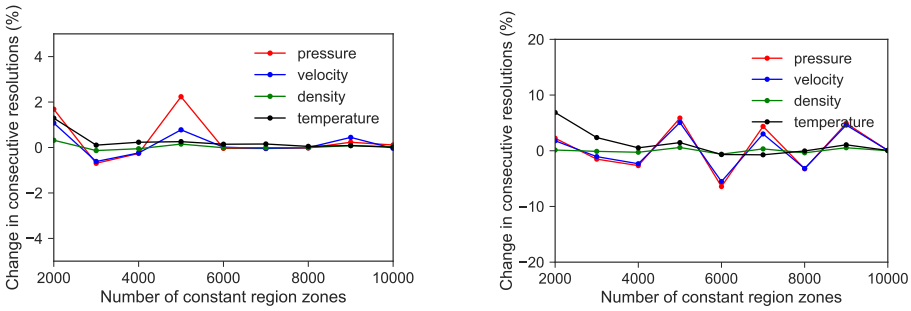

Figure B.1: Percent change in peak states 5 μm into the sample material as the number of zones in the constant mesh section was increased for the tantalum target (a) and for the copper target (b).

B.2 Convergence of hydrodynamic instability mesh

The meshing scheme in Figure 4.12 was used to study mesh convergence in 2D and 3D simulations. The simulations were initialized with the shock generated by

converged simulations of the 30 J energy source for tantalum targets and by the 10 J energy source for copper targets.

The energy source simulations used a significantly higher resolution than used in the hydrodynamic instability simulations in order to resolve the 1 μm thick energy source. Consequently, the shock state saved from the energy source simulations was much higher resolutions than the hydrodynamic instability simulation mesh initialized by the energy source simulations. The lower resolution meshes smoothed out the shock wave and produced different loading conditions. Increasing the mesh resolution therefore changed two aspects of the simulation. First, higher resolution better resolved the ablator-sample interface and the instability growth. Second, higher resolution resulted in a different loading condition.

In order to maintain loading conditions across simulations, a single mesh resolution was selected for 2D and 3D simulations for both tantalum and copper targets. This decision meant that the upper limit of mesh resolution was set by the more expensive 3D simulations.

Convergence was determined by comparing the growth factor over increases in mesh resolution (Figure B.2 in 2D and Figure B.3 in 3D). The final amplitude of the perturbation was determined by averaging over the final 20 ns of the simulation to remove elastic oscillations of the ripple after instability growth ceased.

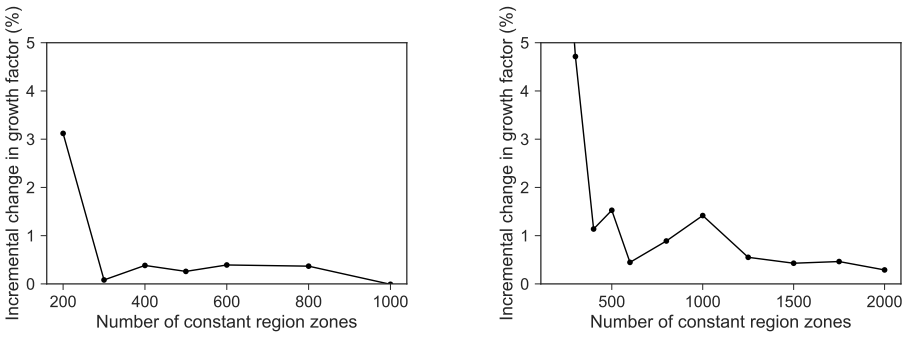

(a) (b)

Figure B.2: Percent change in growth factor as the number of zones in the constant mesh section was increased for 2D simulations of the tantalum target (a) and for the copper target (b).

As in the 1D case, the tantalum target simulations converged rapidly, with $< 1\%$ increments in amplitude. The copper target simulations do not converge as rapidly. The growth factor continued to increment by 1% as mesh resolution is increased

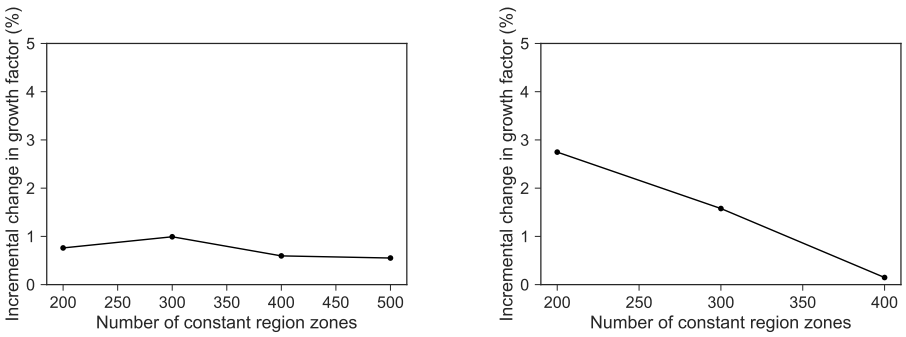

Figure B.3: Percent change in growth factor as the number of points in the constant mesh section was increased for 3D simulations of the tantalum target (a) and for the copper target (b).

until over 1,250 zones were used. As seen in the energy source mesh convergence, the loading wave propagation in CRF was more sensitive to mesh resolution than in CH. A resolution increase of over 1,400 zones in the constant region was required to decreases incremental percent change to $< 1\%$, indicating this level of resolution was converged to the same level as the CH-tantalum simulations. Additional resolution in the 3D hydrodynamic simulations were too expensive, so the maximum mesh resolution possible was 300 zones in the constant mesh section. The residual mesh sensitivity in CRF was not eliminated.

To quantify uncertainty in using a lower resolution mesh, the percent difference between each lower resolution final amplitude and the highest resolution final amplitude was calculated (Figure B.4). In CH-tantalum targets, uncertainty at 300 zones in the constant section was $< 2\%$. In CRF-copper targets, the same resolution resulted in an error of $< 8\%$. An uncertainty of $\pm 8\%$ was assumed to hold for 2D and 3D CRF-copper targets over the range of drives simulated.

As the resolution increased in hydrodynamic instability convergence study, the resolution of the loading wave also increased, changing the loading conditions and affecting the growth factor. This effect is quantified in Figure B.5. For low mesh resolutions, additional resolution increased the ripple pressure and consequently the growth factor. At higher mesh resolutions, the ripple pressure and growth factor were less correlated, indicating that the loading condition was converged and only the convergence of the growth factor was tested.

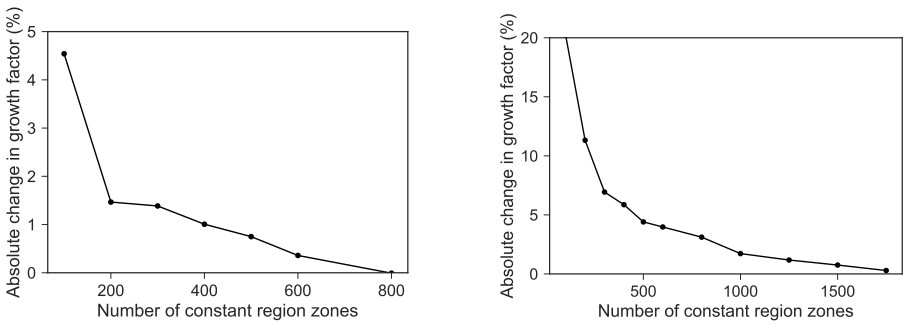

(a) (b)

Figure B.4: Percent difference between the growth factors of a given 2D CH-tantalum target simulation and the highest resolution simulation, indicating < 2% error for 300 zones in the constant region (a). Results from CRF-copper target simulations indicate slower convergence and < 8% error (b).

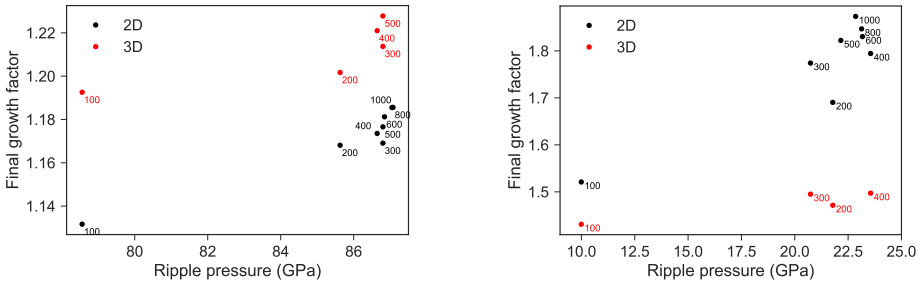

(a) (b)

Figure B.5: Final growth factor as a function of ripple pressure for different mesh resolutions. Each point is labeled with the number of zones used in the constant mesh section. Convergence is plotted for the tantalum targets (a) and for the copper targets (b).

B.3 Comparison of silica and carbon aerogel EOS

The energy source mesh convergence study was conducted for both the carbon aerogel and the silica aerogel Sesame EOS. Both the silica and the carbon aerogel converged slower than CH, with 5% oscillations in peak pressure and velocity even at the highest resolution (Figure B.6). However, the release from the peak state as the loading wave moved through the ablator was jagged in the carbon, but smooth in the silica (Figure B.7). The release influences the instability evolution, so this mesh sensitivity and jaggedness was concerning.

The loading conditions for simulations with 8,000 zones in the constant mesh section (Figure B.8) were similar. The averaging in the bulk pressure calculation smooth

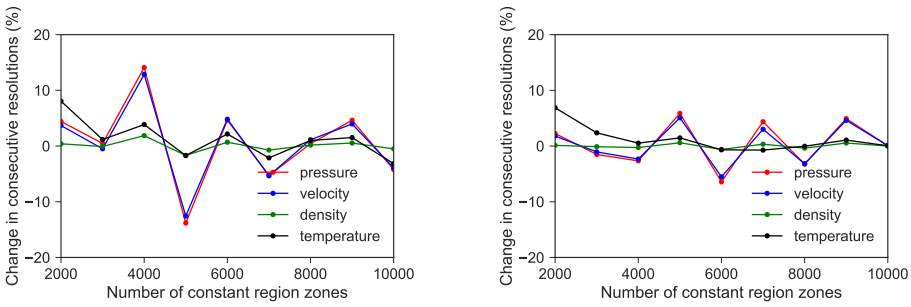

Figure B.6: Change in ripple state as a function of number of zones in the constant mesh section. Convergence is plotted for the carbon aerogel (a) and for the silica aerogel (b).

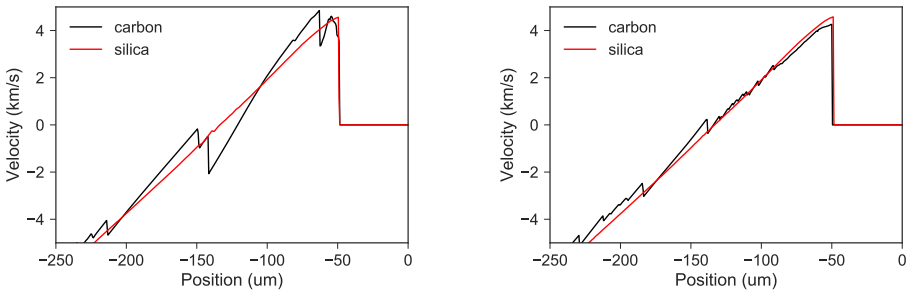

Figure B.7: Velocity in the ablator behind the shock for the silica and carbon aerogel EOS with 5,000 zones in the constant mesh section (a) and 10,000 zones (b).

out the jaggedness in the release, so it was not seen in this plot. The velocity behind the shock was nearly identical. The difference in bulk pressure felt by the sample was caused by a difference in the density the foams compact to behind the shock.

The goal of the simulations was to demonstrate trends in growth factor, so matching the shock and immediate release was important, while matching the peak condition was less important. The silica EOS was selected to provide a smooth release that is insensitive to mesh resolution, unlike the carbon EOS, while keeping in mind that the peak state is only converged to within 5%.

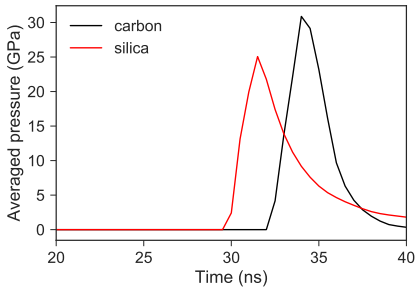

Figure B.8: Comparison of bulk pressure for a 10 J energy source using the carbon aerogel EOS and the silica aerogel EOS.

Appendix C

SUMMARY OF SAMPLE PROFILES

C.1 Summary of tantalum sample profiles

To calculate the growth factor of the instability, the post-shot and the pre-shot perturbation amplitudes were averaged in a 100 μm radius surrounding the shot center, within the assumed planar loading region. Additionally, a larger portion of the profile was analyzed to determine the validity of the assumed planar loading region and to understand the effect of radially varying loading on the deformation of the sample.

Two additional metrics were used to understand the affect of radially varying loading. The shape of the crater left by dynamically compressing the sample was calculated by applying a Gaussian filter with a standard deviation of the perturbation wavelength to the profile. Additionally, radially varying loading pushed the perturbation peaks away from the shot center. This asymmetry effect was quantified by measuring the difference in distance between an extrema and its neighboring extrema.

Three types of plots based on these metrics were calculated for all tantalum sample profiles are shown in Figures C.1, C.2, C.3, and C.4. Samples are described by an ID number, the peak pressure, the spot shape produced by the phase plate used (either a square 1 mm on a side or a 0.6 mm diameter circle) and the beams used (E for east and W for west, with E+W meaning overlapped beams).

In order to calculate a PTV, the extrema neighboring a given extrema were found. For the 2D initial perturbation each extrema should have two neighbors. Each 3D initial perturbation extrema should have four neighbors. In some profiles, extrema were so deformed the extrema finding algorithm and neighbor finding algorithm did not find the correct number of neighbors. These regions were masked with black. These plots use X and Y as the lateral directions opposed to earlier profile plots where X was the axial direction.

The crater lineout plots show the average across a 200 μm wide strip through the shot center, filtered to remove the initial perturbations. As peak pressure increased, the bottom of this profile steepened, to the point where the profile changed more the 2 μm in a 100 μm radius of the shot center where the PTV was averaged. The

profile at the shot center was expected to be flat based on planar loading; increased curvature here demonstrates a departure from this assumption. It was expected that a higher peak pressure would result in a deeper crater. Two sample profiles, ID 44 and 51, were outliers. The crater on sample ID 44 was very asymmetric which is not understand. The crater on sample ID 51 was much smaller than expected given the peak pressure. The PTV was also low, consistent with a lower peak pressure. The laser energy on this shot was estimated because the system normally used to measure the energy did not work. It is possible this estimation was incorrect.

The PTV lineout plots show the average PTV across the same 200 μm strip through the shot center, plotted with the filtered crater profile as a reference. As peak pressure increased, the PTV in the shot center increased more than at the edges of the shot, consistent with a loading that decays radially from the shot center. However, for profiles with the 2D initial perturbation driven to peak pressures above roughly 100 GPa, the PTV increased outside the shot center before decaying again, forming an annulus. The peak occurred within the extent of the laser spot, but outside of the 100 μm radius where planar loading was expected.

The reason for this increase in PTV is not known. The loading should be weakened by the release, resulting in a lower initial growth rate of the instability and a lower final PTV. This annular increase in PTV did not occur in samples with the 3D initial perturbation.

In addition to seeing a weaker loading perpendicular to the face of the sample, the region outside the shot center saw a radial component of loading that could have pushed the peaks away from the shot center. The extent of the radial deformation is captured by the asymmetry lineout plots. Positive values indicate peaks pushed to the left. For all samples, the asymmetry value decreased with increasing X, consistent with peaks pushed away from the shot center.

These conclusions hold roughly over the entire profile (Figures C.5, C.6, C.7, and C.8). The asymmetry of the perturbation is more apparent over the entire domain. Referring to the contours of the crater height, the asymmetry begins near the edge of the laser spot and peaks near the rim of the crater. The annular region of extra PTV growth occurred at a smaller radius than the peak asymmetry, on the walls of the crater. Regions with peak asymmetry also frequently caused issues for the extrema neighbor finding algorithm, resulting in the black masked regions.

When the profile was filtered with a 2 μm standard deviation Gaussian filter and

subtracted from the unfiltered profile, small bumps in the shot region were revealed (Figures C.9 and C.10). It is not clear what caused the small bumps. Even at roughly the same peak pressure, the square spot produced bumps while the circle spot did not. The bumps occurred when the sample was driven with the east beam and with the two beams overlapped. Features stand out at the edge of the shot region on samples driven with the circle phase plate, but these corresponds to radially deformed perturbations and not small bumps in the shot center.

C.2 Summary of copper sample profiles

The profiles of recovered copper samples were qualitatively different than the profiles of recovered tantalum samples. The crater profile was much shallower and much flatter (Figures C.11, C.12, and C.13). The crater shape was less uniform, with local extrema showing up in the crater. These local extrema made defining a shot center difficult. All shot centers were selected by eye, leading to imprecision. Increased deformation in the profiles resulted in more problems in the extrema neighbor identifying algorithm, so much of the lineouts are masked. Contour plots reveal these deformations cover the entire shot region (Figures C.14, C.15, and C.16). Compared to the tantalum profile results, the trends in PTV and asymmetry were inconsistent.

Some samples were heated before the shot. The preheat system did not work as planned during the experiment. The sample may have been heated to a temperature up to 600-800 K, but lower temperatures were also possible.

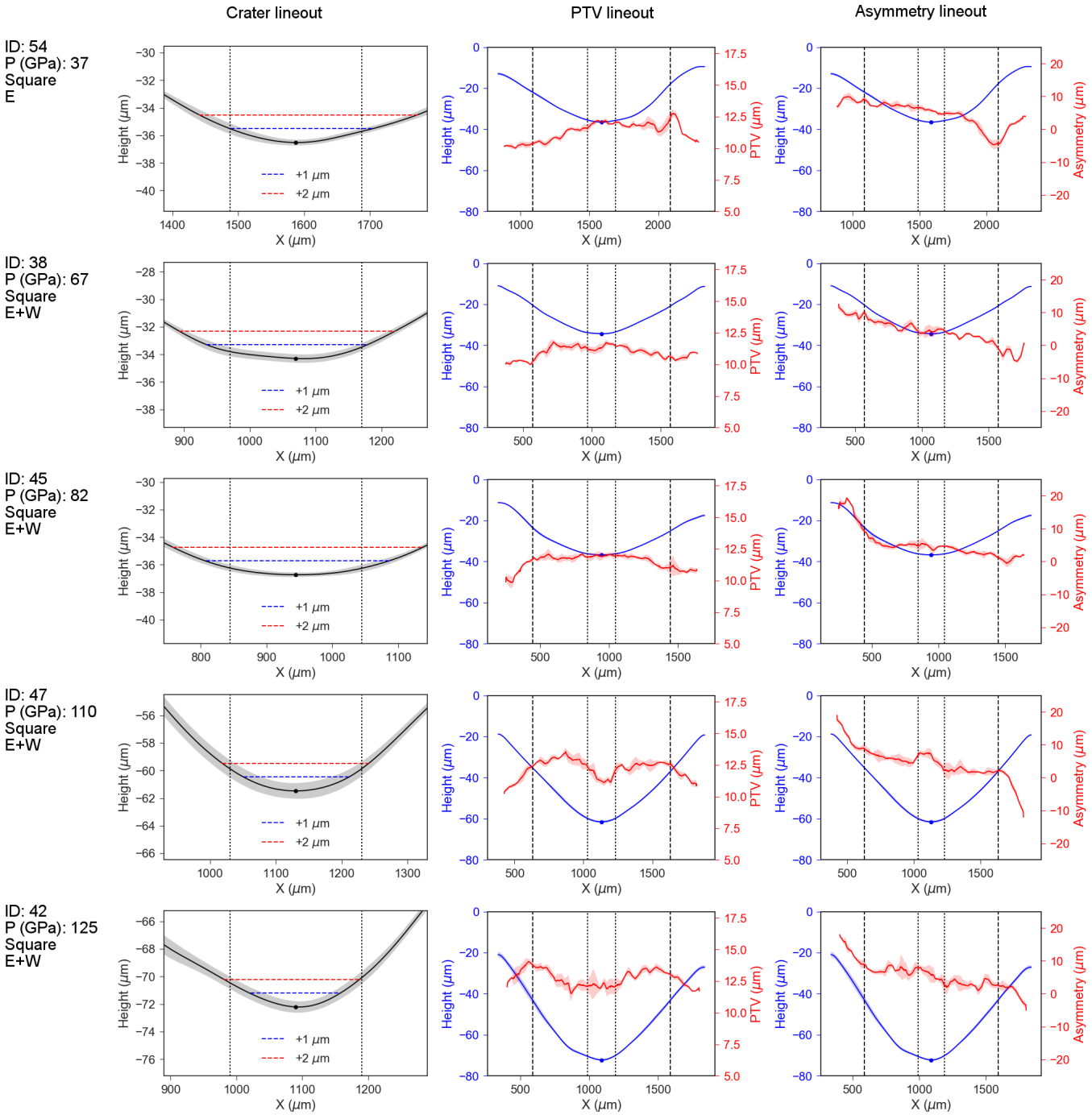

Figure C.1: Summary of profiles of tantalum samples manufactured with a 2D initial profile and driven with the square spot phase plate. All profiles were filtered with a 2 μm standard deviation Gaussian filter. Lineouts were taken from a 200 μm wide strip running in the X direction through the center of the profile. Dotted lines highlight the 100 μm radius region where the PTV was averaged to calculated the growth factor. The dashed lines highlight the extent of the laser spot. The standard deviation of the average used to calculate each curve is shown in the shading surrounding the curve.

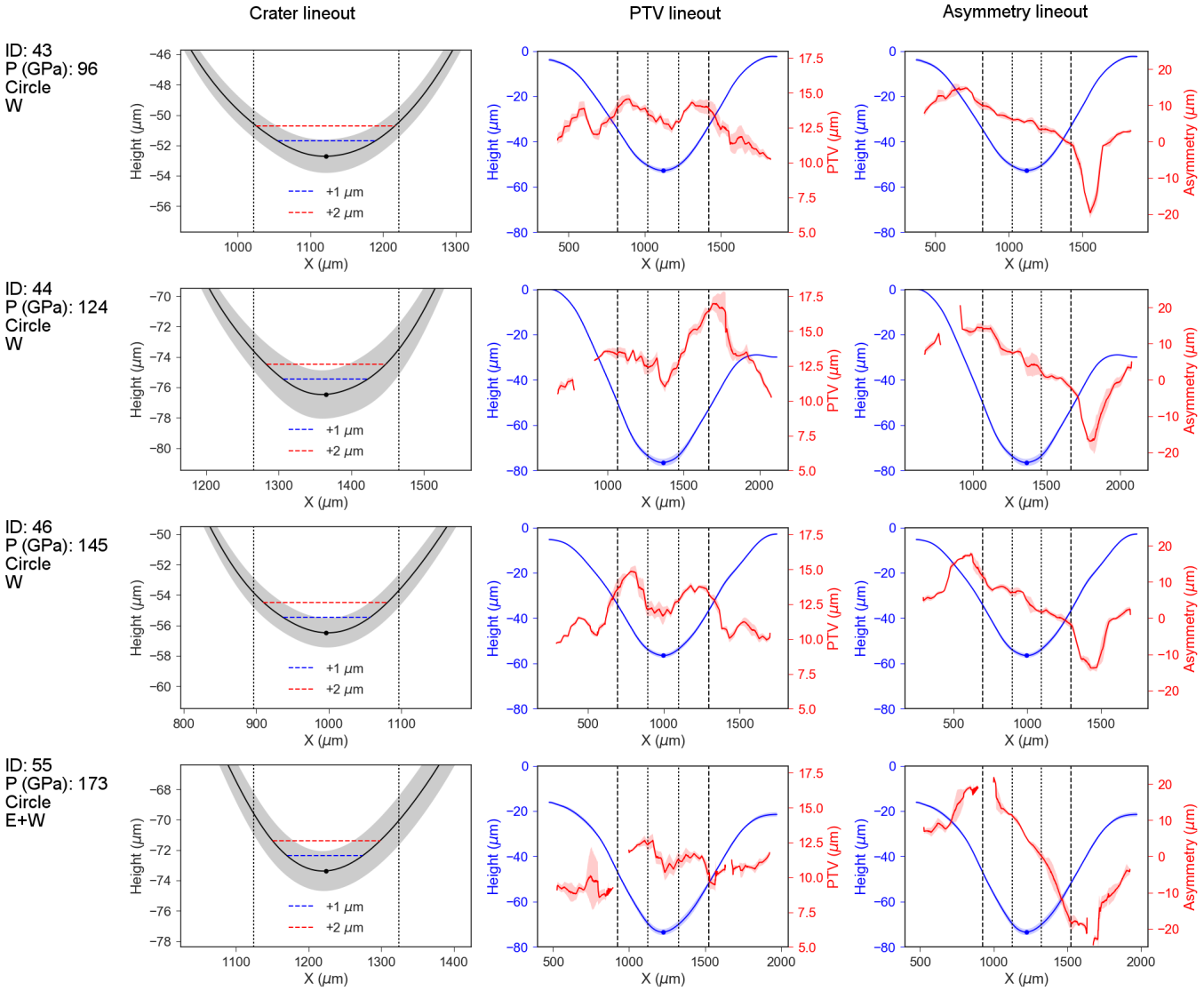

Figure C.2: Summary of profiles of tantalum samples manufactured with a 2D initial profile and driven with the circle spot phase plate. All profiles were filtered with a 2 μm standard deviation Gaussian filter. Lineouts were taken from a 200 μm wide strip running in the X direction through the center of the profile. Dotted lines highlight the 100 μm radius region where the PTV was averaged to calculated the growth factor. The dashed lines highlight the extent of the laser spot. The standard deviation of the average used to calculate each curve is shown in the shading surrounding the curve.

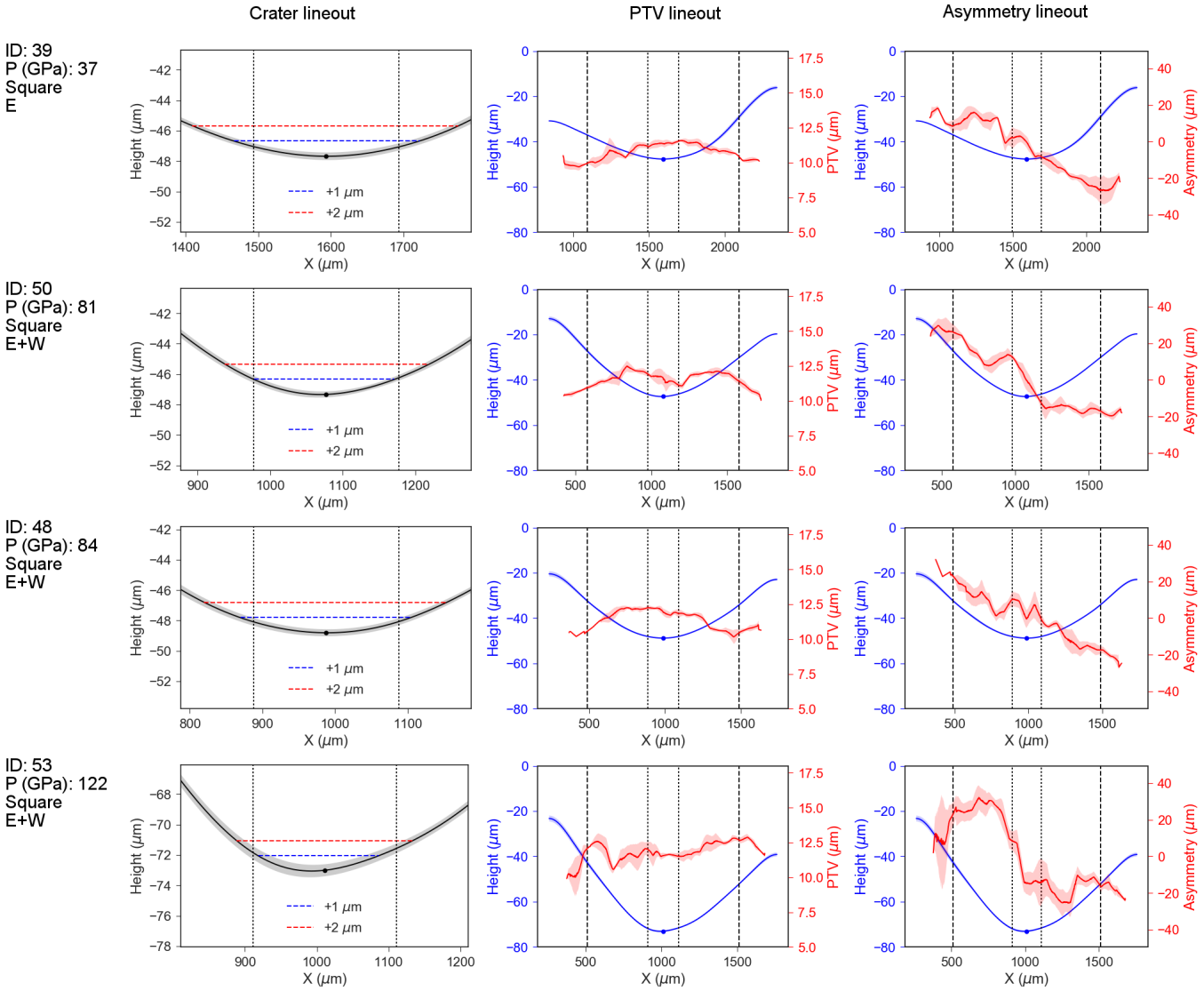

Figure C.3: Summary of profiles of tantalum samples manufactured with a 3D initial profile and driven with the square spot phase plate. All profiles were filtered with a 2 μm standard deviation Gaussian filter. Lineouts were taken from a 200 μm wide strip running in the X direction through the center of the profile. Dotted lines highlight the 100 μm radius region where the PTV was averaged to calculated the growth factor. The dashed lines highlight the extent of the laser spot. The standard deviation of the average used to calculate each curve is shown in the shading surrounding the curve.

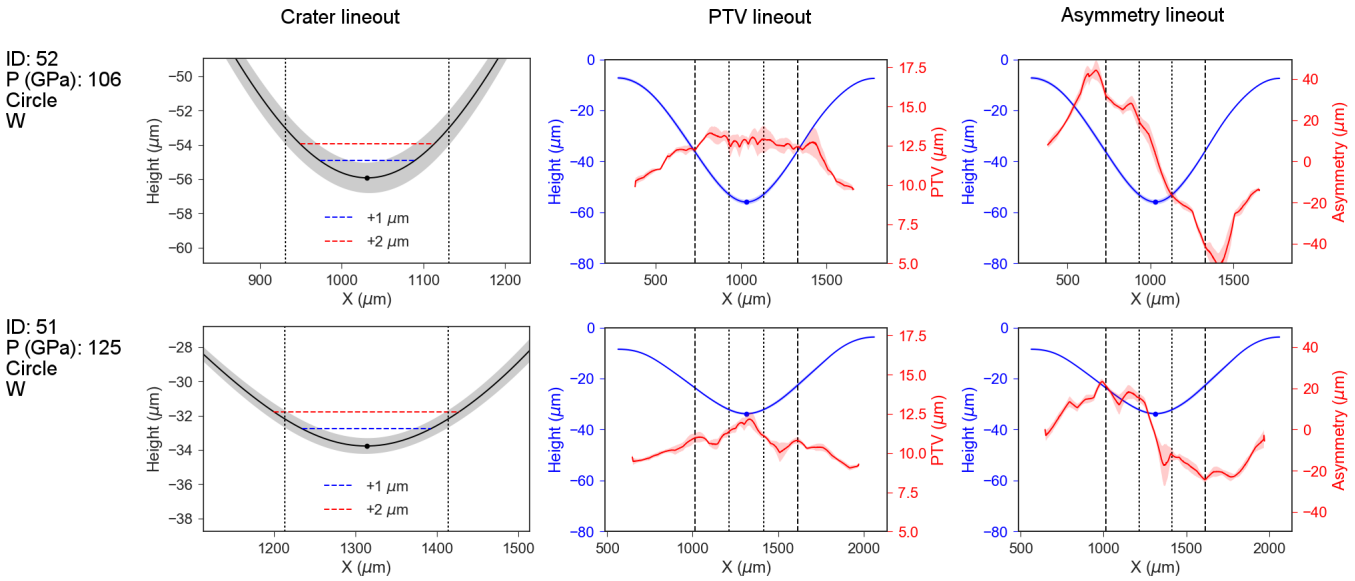

Figure C.4: Summary of profiles of tantalum samples manufactured with a 3D initial profile and driven with the circle spot phase plate. All profiles were filtered with a 2 μm standard deviation Gaussian filter. Lineouts were taken from a 200 μm wide strip running in the X direction through the center of the profile. Dotted lines highlight the 100 μm radius region where the PTV was averaged to calculated the growth factor. The dashed lines highlight the extent of the laser spot. The standard deviation of the average used to calculate each curve is shown in the shading surrounding the curve.

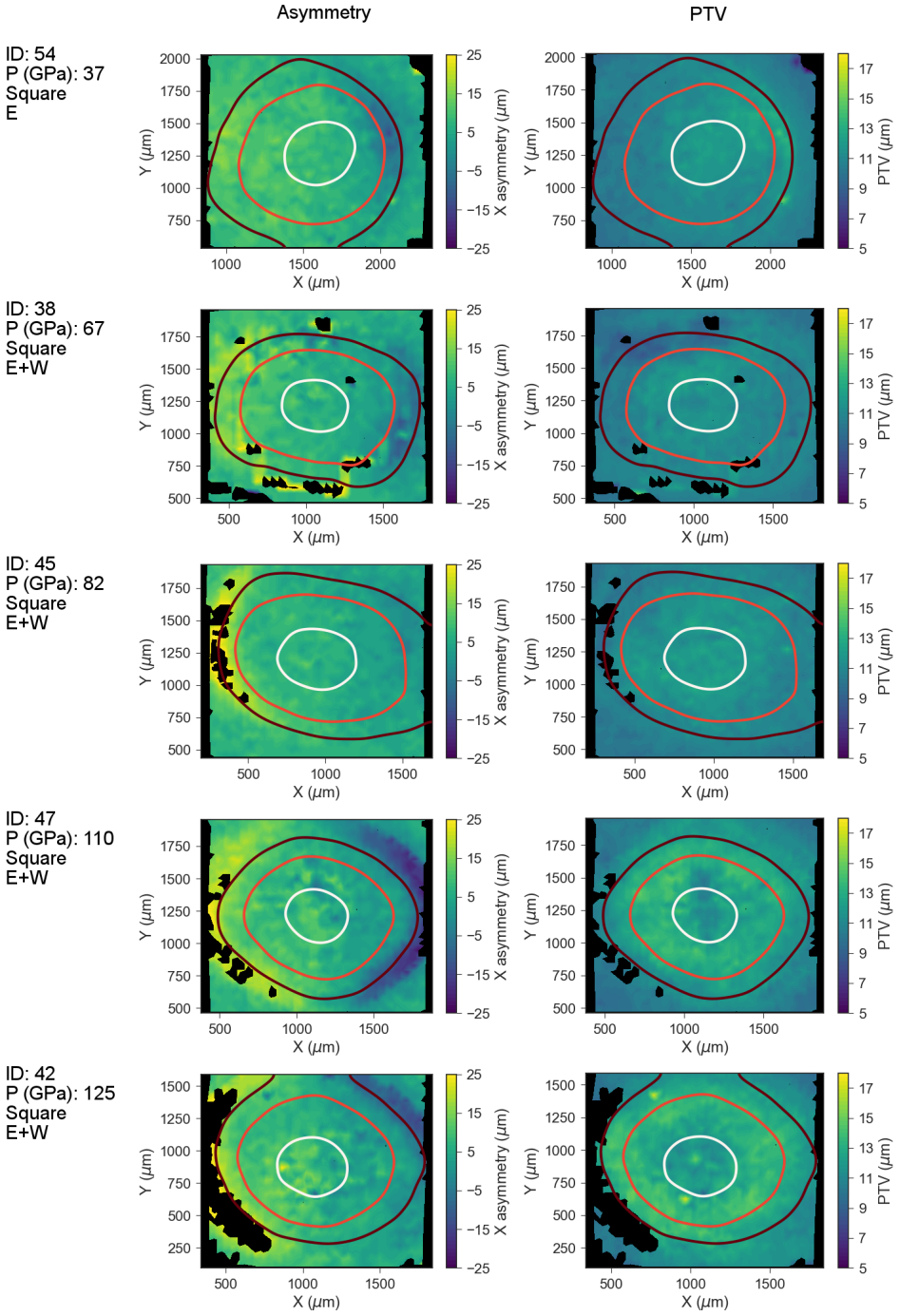

Figure C.5: Summary of profiles of tantalum samples manufactured with a 2D initial profile and driven with the square spot phase plate. All profiles were filtered with a 2 μm standard deviation Gaussian filter. Contours mark 40%, 60%, and 90% the maximum depth of the crater.

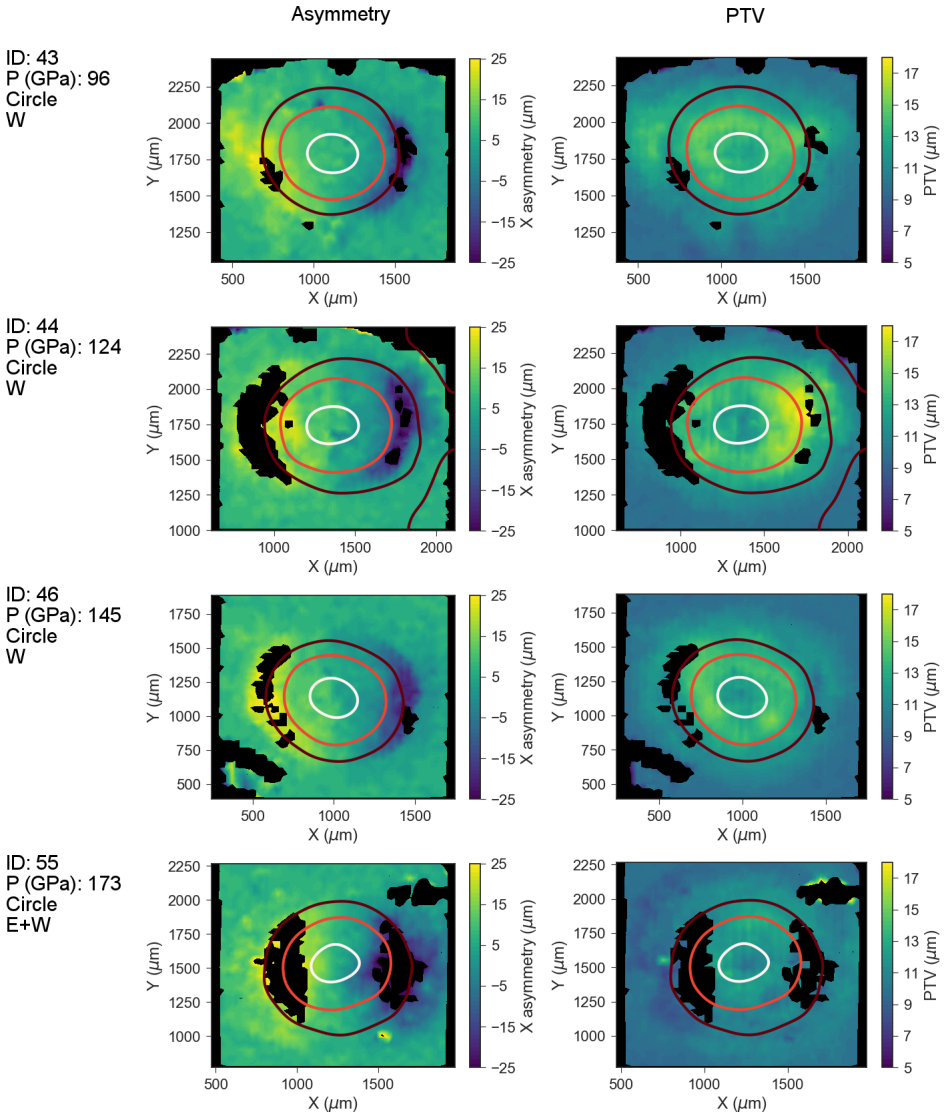

Figure C.6: Summary of profiles of tantalum samples manufactured with a 2D initial profile and driven with the circle spot phase plate. All profiles were filtered with a 2 μm standard deviation Gaussian filter. Contours mark 40%, 60%, and 90% the maximum depth of the crater.

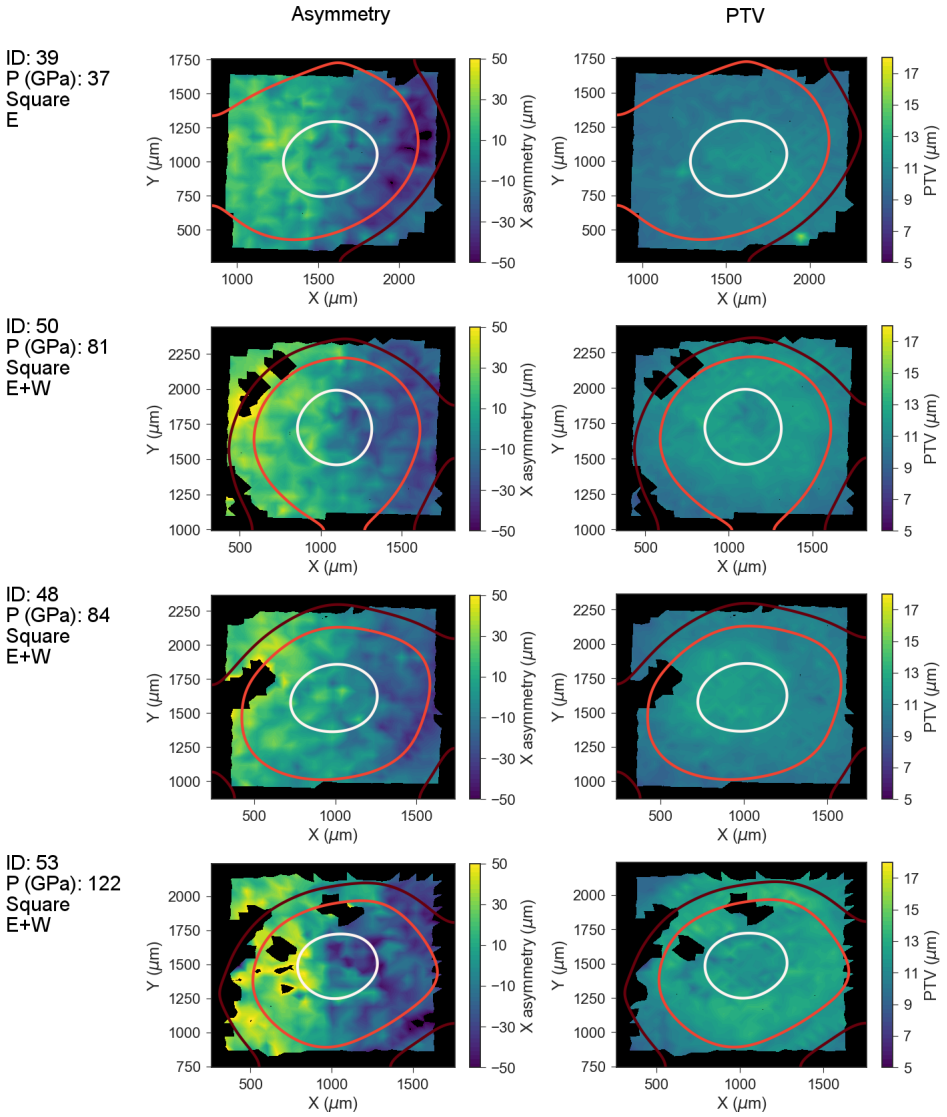

Figure C.7: Summary of profiles of tantalum samples manufactured with a 3D initial profile and driven with the square spot phase plate. All profiles were filtered with a 2 μm standard deviation Gaussian filter. Contours mark 40%, 60%, and 90% the maximum depth of the crater.

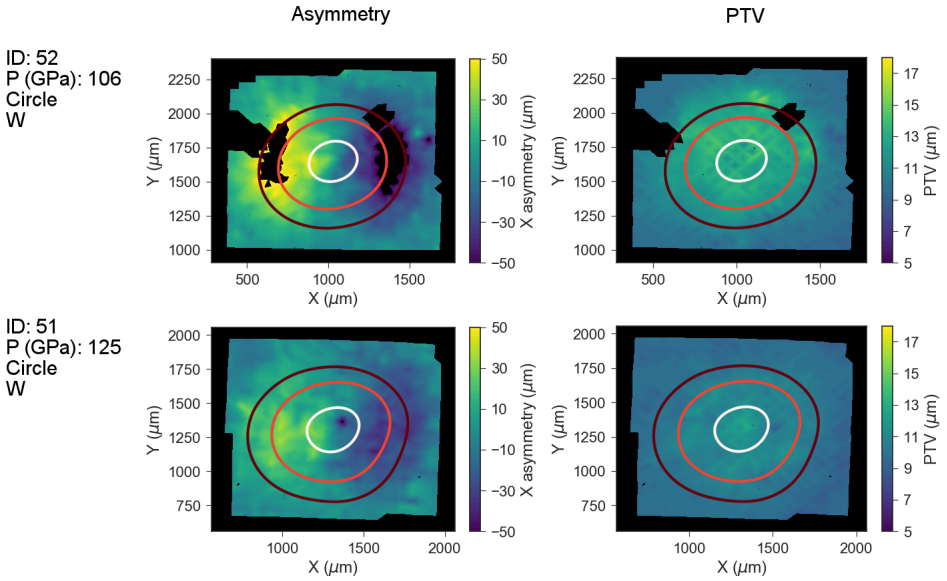

Figure C.8: Summary of profiles of tantalum samples manufactured with a 3D initial profile and driven with the circle spot phase plate. All profiles were filtered with a 2 μm standard deviation Gaussian filter. Contours mark 40%, 60%, and 90% the maximum depth of the crater.

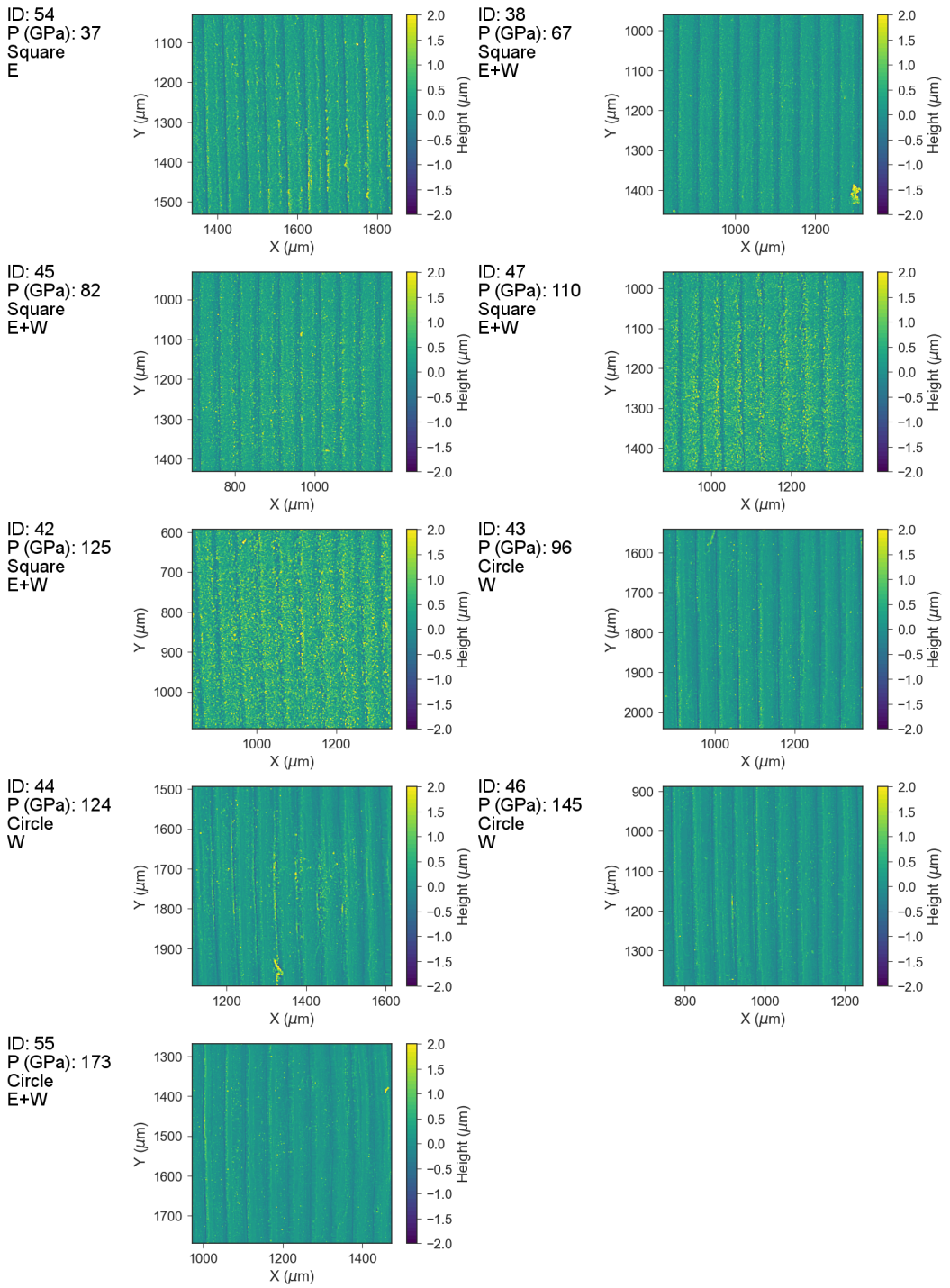

Figure C.9: Plots of the difference in profiles of tantalum samples manufactured with a 2D initial profile with and without the 2 μm standard deviation Gaussian filter.

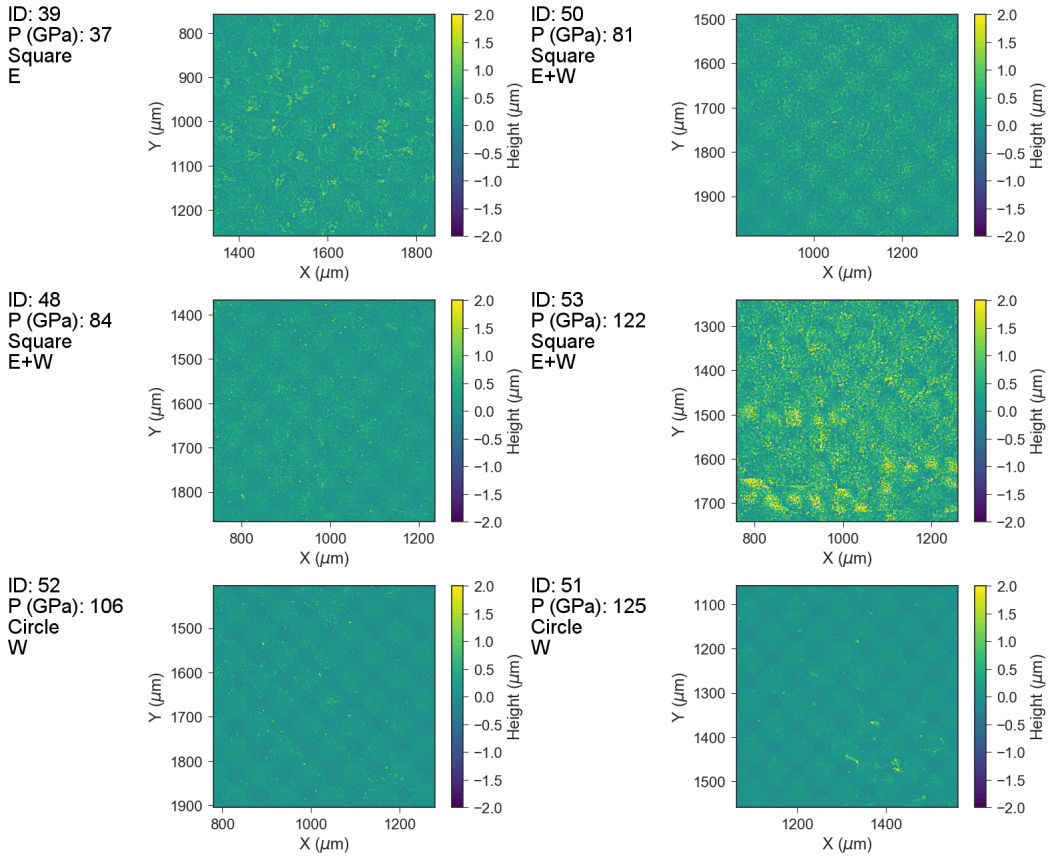

Figure C.10: Plots of the difference in profiles of tantalum samples manufactured with a 3D initial profile with and without the 2 μm standard deviation Gaussian filter. The barred regions on sample 53 are artifacts from stitching the profile together.

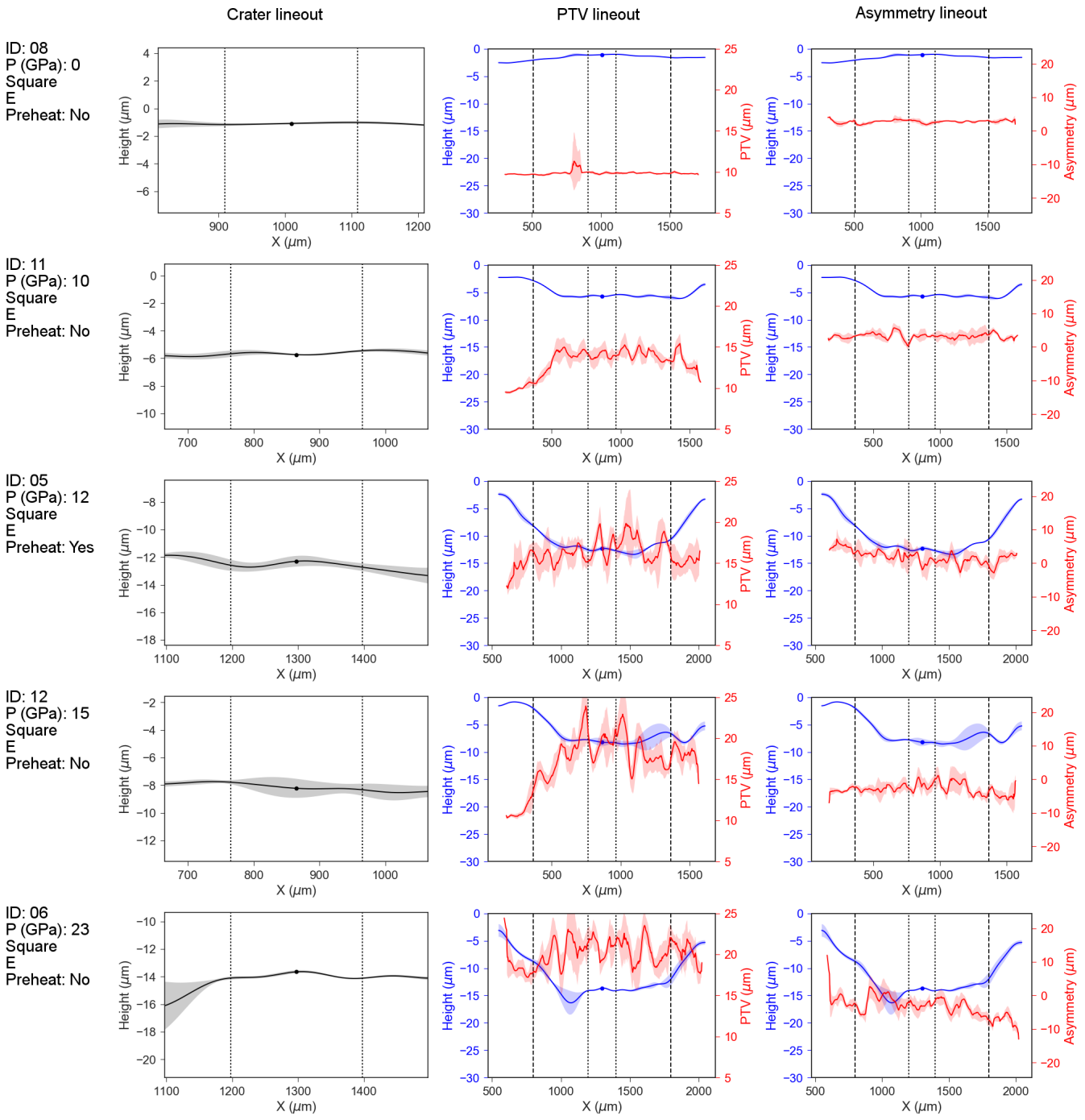

Figure C.11: Summary of profiles of copper samples manufactured with a 2D initial profile and driven with the square spot phase plate. Lineouts were taken from a 200 μm wide strip running in the X direction through the center of the profile. Dotted lines highlight the 100 μm radius region where the PTV was averaged to calculated the growth factor. The dashed lines highlight the extent of the laser spot. The standard deviation of the average used to calculate each curve is shown in the shading surrounding the curve. The bump in the sample 8 PTV was from a fiber left on the sample.

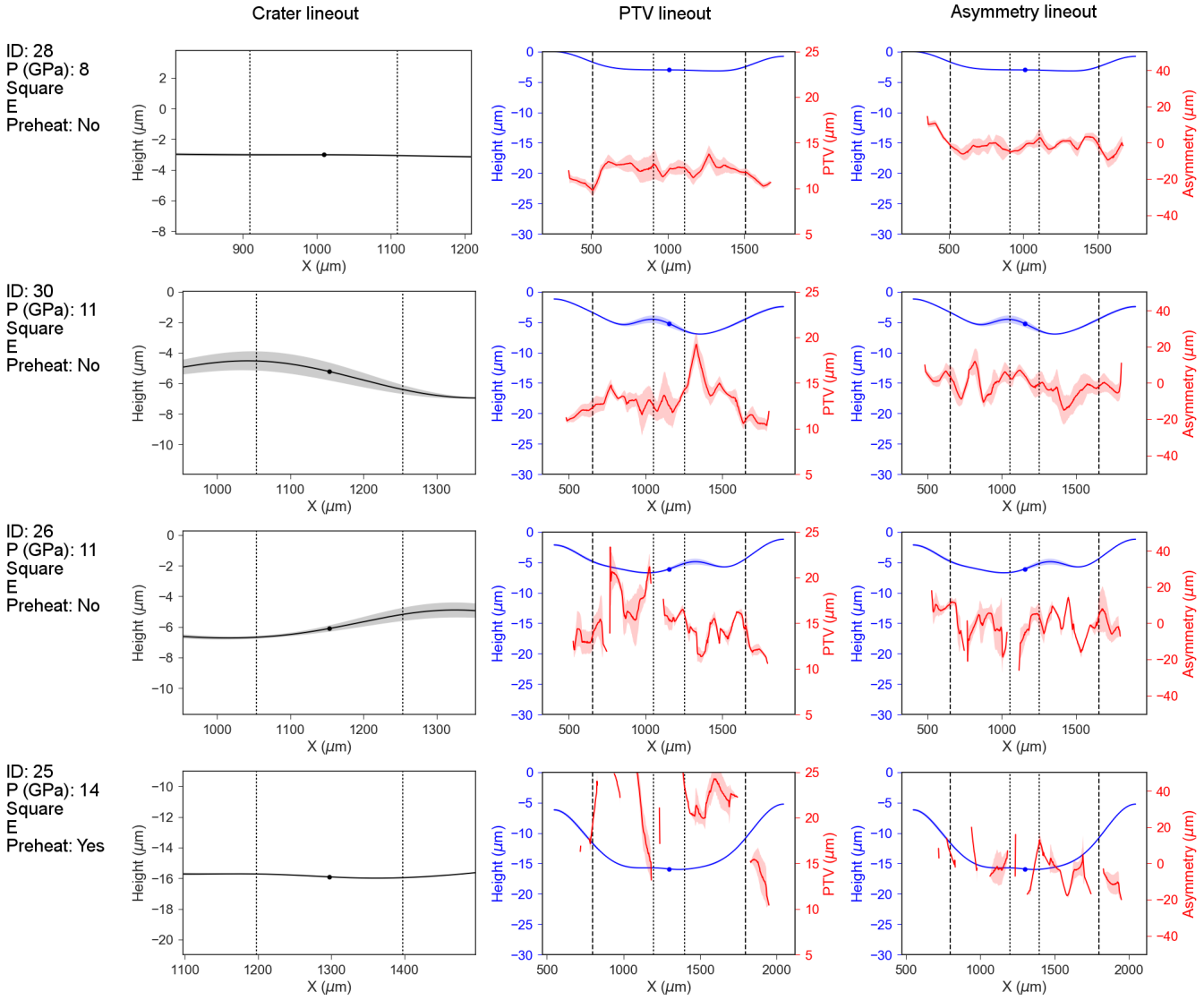

Figure C.12: Summary of profiles of copper samples manufactured with a 3D initial profile and driven with the square spot phase plate. Lineouts were taken from a 200 μm wide strip running in the X direction through the center of the profile. Dotted lines highlight the 100 μm radius region where the PTV was averaged to calculated the growth factor. The dashed lines highlight the extent of the laser spot. The standard deviation of the average used to calculate each curve is shown in the shading surrounding the curve.

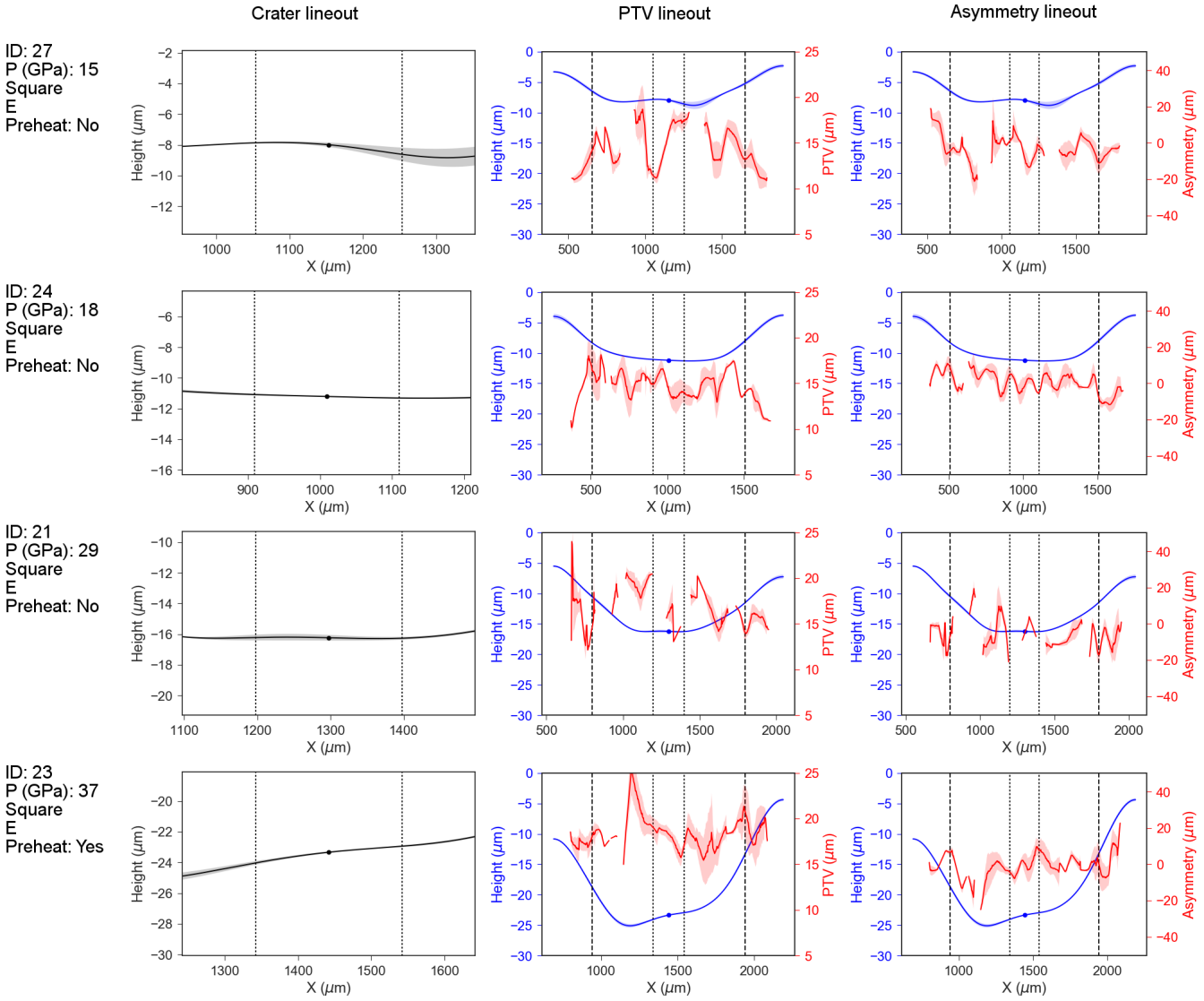

Figure C.13: Summary of profiles of copper samples manufactured with a 3D initial profile and driven with the square spot phase plate. Lineouts were taken from a 200 μm wide strip running in the X direction through the center of the profile. Dotted lines highlight the 100 μm radius region where the PTV was averaged to calculated the growth factor. The dashed lines highlight the extent of the laser spot. The standard deviation of the average used to calculate each curve is shown in the shading surrounding the curve.

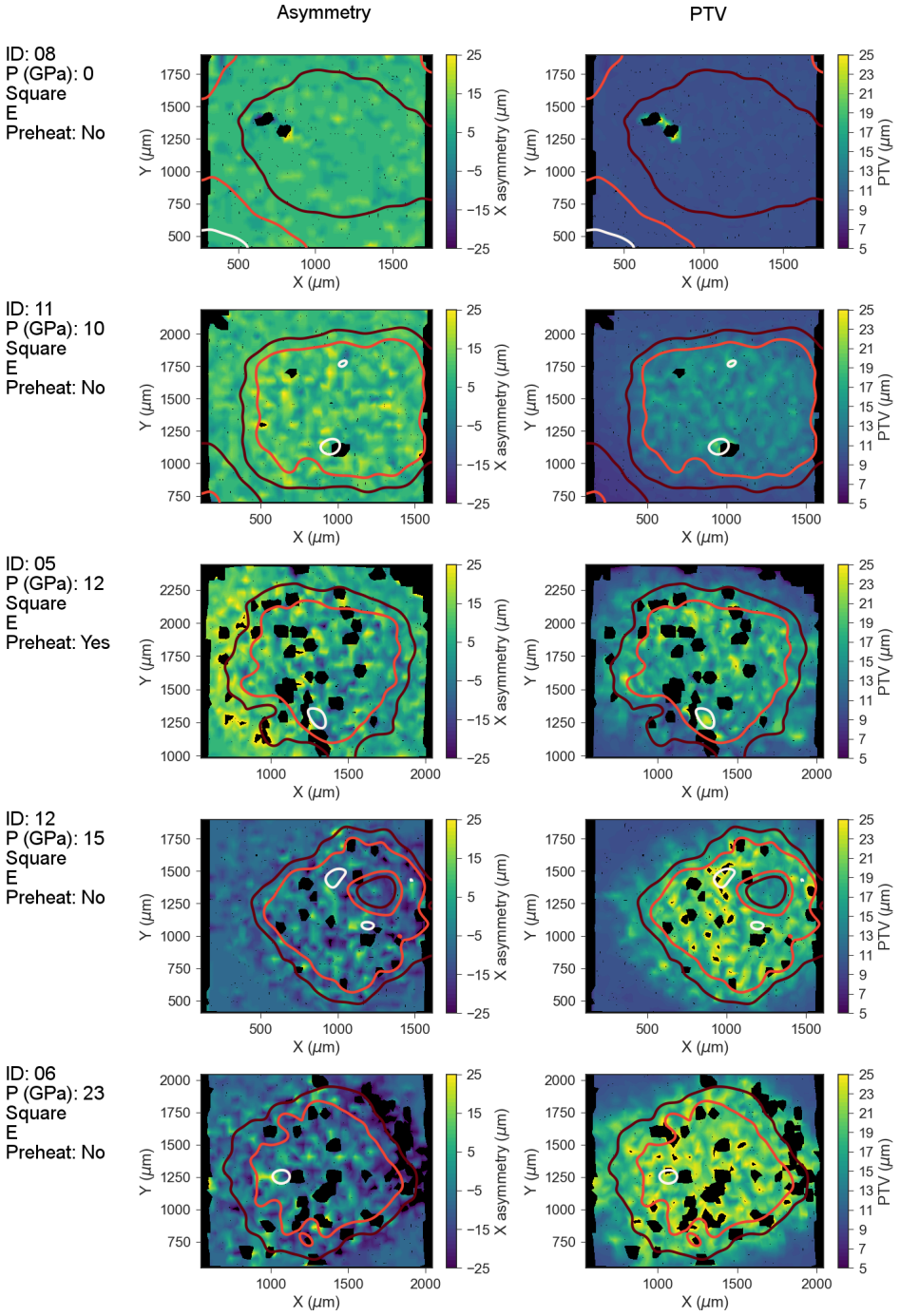

Figure C.14: Summary of profiles of copper samples manufactured with a 2D initial profile and driven with the square spot phase plate. Contours mark 40%, 60%, and 90% the maximum depth of the crater. The bump in the sample 8 PTV was from a fiber left on the sample.

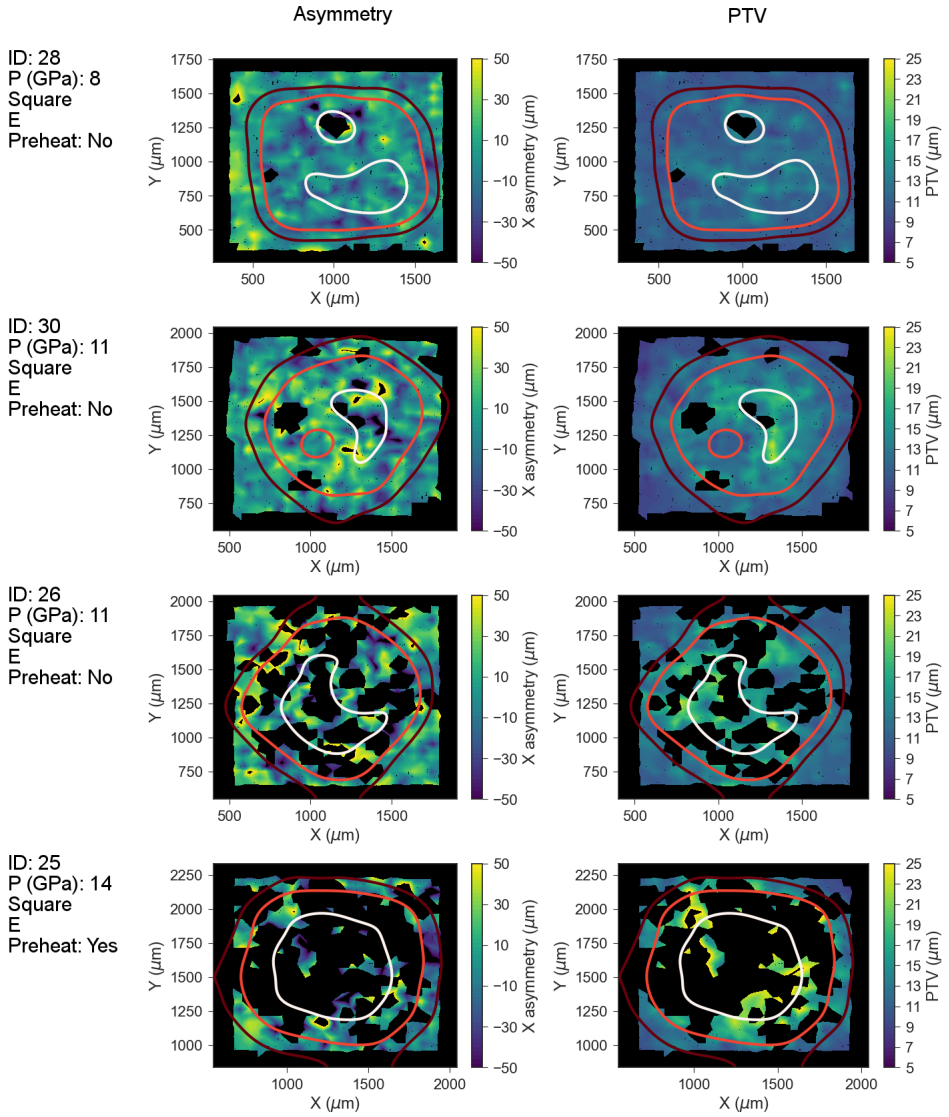

Figure C.15: Summary of profiles of copper samples manufactured with a 3D initial profile and driven with the square spot phase plate. Contours mark 40%, 60%, and 90% the maximum depth of the crater.

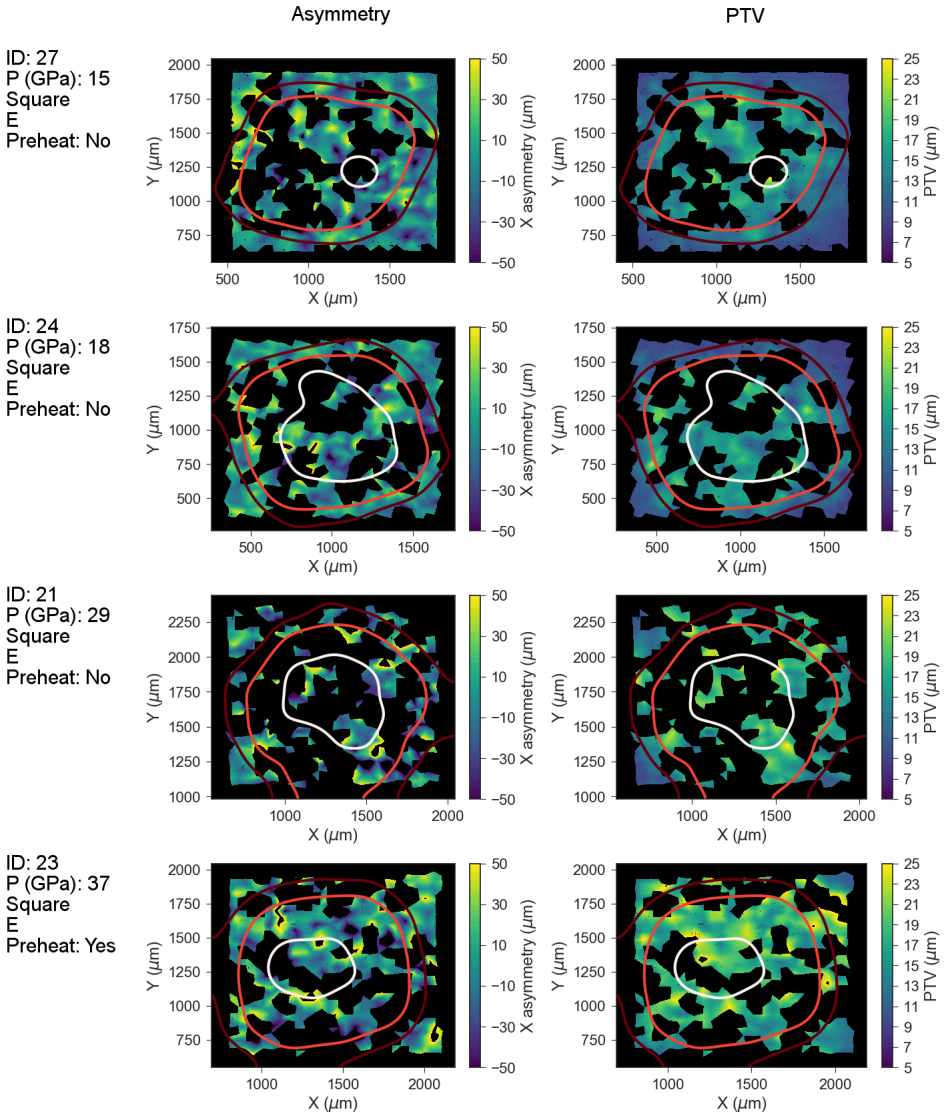

Figure C.16: Summary of profiles of copper samples manufactured with a 3D initial profile and driven with the square spot phase plate. Contours mark 40%, 60%, and 90% the maximum depth of the crater.